

https://dspace.org/

An investigation of high speed metal forming with liquid shock waves.

Kosing, Oliver E

1998
https://hdl.handle.net/10539/26234

Downloaded from a DSpace repository. https://dspace.org/

An Investigation Of High Speed Metal Forming With Liquid Shock Waves

Oliver E. Kosing

A thesis submitted to the Faculty of Engineering, University of the Witwatersrand, Johannesburg, in fulfilment of the requirements for the degree of Doctor of Philosophy.

Johannesburg, November 1998

Declaration

I declare that this thesis is my own, unaided work, except where otherwise acknowledged. It is being submitted for the degree of Doctor of Philosophy in the University of the Witwatersrand, Johannesburg. It has not been submitted before for any degree or examination in any other university.

Signed this 25 day of Nov. 1998

Oliver Kosing

Oliver E. Kosing.

To my parents for their support during my studies

Acknowledgements

I would like to express my greatest thanks to my supervisor Professor Beric W. Skews who has initiated this project and who has supported, advised and encouraged me in all regards. Without his help it would have been impossible for me to carry out my PhD studies at WITS University.

In addition I would like to thank Prof. Skews for giving me the possibility to present parts of this work at two international conferences, in Australia and Greece. I would also like to thank him for his helpful comments regarding this thesis.

I gratefully thank Prof. Grönig of the RWTH Aachen for his help in arranging my PhD studies at the University of the Witwatersrand.

I would like to thank my friends and colleagues Filipe Barbosa, John de Visser, Russell Hattingh, Mike Draxl, Graham Doyle, Samuel Kwofie, and Luke Felthun for their great help and assistance during my time at the School of Mechanical Engineering. Filipe Barbosa and John de Visser are gratefully thanked for proof reading parts of this document.

The assistance of Prof. Chandler is gratefully acknowledged. Rolf Mecking, who carried out a practical training in the 'Flow Research Group' is thanked for his work in connection with this project.

The workshop and the support staff of the School of Mechanical Engineering under the direction of John Copper is gratefully thanked for their helpful comments concerning the design of many shock tube parts and their excellent machining.

I would like to acknowledge the University of the Witwatersrand and the School of Mechanical Engineering for their contribution towards tuition fees and living expenses and the strong support which made me, as a foreign student, always feel welcome.

The author also wishes to gratefully acknowledge the support of the Foundation for

Research and Development (FRD).

Finally my thanks must go to Andra for her patience, encouragement and proof reading parts of this thesis and her spirit of adventure to follow me to Africa and to my parents for their great support, which enabled me to carry out my PhD studies in the new South Africa.

Abstract

In this work a new high speed metal forming process is experimentally and theoretically investigated and discussed. The high speed metal forming is carried out in a liquid shock tube. The pressure energy of a liquid shock wave, which is generated non-explosively is used to form the metal workpiece.

The high speed metal forming can be carried out by operating the shock tube in two different modes, the air mode and the projectile mode. In the air mode the liquid shock wave is generated by the impact of a gas shock wave on the water surface. In the projectile mode a rapidly moving projectile impacts on the water surface and generates the liquid shock wave. The projectile mode is more suitable for high speed metal forming than the air mode due to its precise controllability and more efficient energy transfer.

Theoretical approaches are presented to calculate the energy transformation in the liquid shock tube for the projectile mode. The impact velocity of the projectile and the kinetic energy available is computed. By using the method of characteristics the liquid shock wave profile is calculated from the impact velocity of the projectile. This numerical approach enables the prediction of the maximum pressure, the energy and the impulse of the liquid shock wave. The deformation energy absorbed by the test specimen is calculated by using the flow-stress power law.

The effect of different projectile masses, materials and geometries are discussed. Experimental results are presented, which show how the contour of the liquid shock wave can be tailored to exactly deliver the amount of energy required for the forming of the metal. Double and triple liquid pressure pulses are generated by using stepped projectile impact surfaces. A finite element program is used to model the impact process of the projectile and to compute the generation and propagation of the liquid shock wave.

The stress strain conditions of deformed copper and mild steel disks are determined. Using the strains obtained from these measurements the deformation energy of the

disks is calculated. A theoretical approach is given to predict the maximum midpoint deflection by assuming a conical shape of the deformed disk. This approach uses an energy method for plastic material behaviour. The deformation process of the metal disks during the impact of the liquid shock wave is investigated with a high-speed video camera. From the experiment the local and the average deformation velocities and the strain rates are determined. Strain rates at different stages of the deformation process are measured by using a mirror system which allows the recording of the side- and bottom-view simultaneously. An attempt is made to model the deformation process of flat disks by employing a finite element package. In the two-dimensional calculation a liquid shock wave generated by the impact of a projectile is used to deform the flat plate. The results of this numerical model are discussed with respect to experimental results.

The forming of cylindrical mild steel and copper tubes is investigated. For free forming the tubes reveal an unsymmetrical deformational behaviour which can be explained by the liquid shock wave being reflected at the bottom of the tube and thus resulting in double the pressure at the bottom. The stresses and strains of the deformed tubes are determined and the results of the strain calculations are used to obtain the deformation energy of the tubes.
Optical investigations are performed with a high speed video camera to reveal the deformational behaviour of the tubes. The deformation velocities at different locations of the tube are obtained and the strain rates calculated. The results show that the strain rates are much lower for the forming of tubes in comparison to the forming of flat disks.
The deformation of tubes into cylindrical, hexagonal and octagonal dies is investigated. The results show that it is possible to deform the tubes nearly completely into the dies which shows that detailed figuring is possible.

To improve the performance of the liquid shock tube and to reduce the test turn-around times the liquid shock tube is converted into a diaphragmless shock tube. The conversion is done by introducing a slotted section and a new diaphragmless driver to the existing tube.
The new diaphragmless driver is tested by using the shock tube as a normal gas shock tube and by comparing the performance of this new type of driver to already existing diaphragmless drivers.
The improved overall performance of the liquid shock tube is discussed with respect to the old system.

The Contribution of this Work

The use of liquid shock waves generated non-explosively in a liquid shock tube for high speed metal forming is a novel manufacturing process. The aim of this work is to establish the feasibility of this process, to determine various operating parameters, to investigate the impact process of the projectile and the impact process of the liquid shock wave on the metal specimen and to improve the performance of the liquid shock tube.

- Experiments have been carried out with various projectile materials, masses, and geometries to investigate the generation of different types of liquid shock waves. Apart from high speed metal forming these results also contribute to other practical applications of liquid shock waves such as lithotripsy, powder compaction, and rock breaking. By using stepped and double stepped projectiles it was possible to generated unique double and triple liquid shock waves and thus to tailor the energy delivering rate to suit a particular application.

- The impact phenomenon of the projectile on the water surface has been studied in detail experimentally and theoretically. By using the method of characteristics it was possible to predict the maximum pressure, the energy and the impulse of the liquid shock wave. A finite element program has been employed to model the impact process of the projectile and to compute the generation and propagation of the liquid shock wave. The results are of benefit to the characterisation of the shock tube which will be used in many other liquid shock wave work.

- The deformational behaviour of the metal specimen under the impulsive load of the liquid shock wave has been optically investigated. A new optical technique using ultra high speed video cameras has been used to conduct these experiments and to obtain the local deformation velocities and the strain rates for high speed metal forming. A special mirror set-up allowed the recording of the side- and bottom-view of deforming circular plates simultaneously to determine for the first time strain rates at different deformation stages. It was

also possible to numerically investigate the deformation process of flat plates by modeling a two-dimensional problem which simulates the liquid shock tube. These results are of great importance for the scientific research conducted in connection with structural response to explosive shocks and high velocity impact.

- A new simple theoretical approach is presented to predict the midpoint deflection of circular disks. The results of this computation are in excellent agreement with experimental results.

- A novel diaphragmless shock tube driver has been designed. The design distinguishes itself due to its cost efficiency, simplicity, practical usage and reproducibility of generating shock waves. For the generation of gas shock waves an efficiency of 91% of that predicted by ideal shock tube theory and a non-dimensional formation length of 20 could be reached. The new driver can be used on various types of shock tubes and has widespread applications as a rapidly opening valve.

This thesis can be seen as an interdisciplinary work bringing together the studies of gas shock waves, liquid shock waves, impact phenomenon and metal forming. Therefore the structure of this work has been chosen to describe the liquid shock wave research and the high speed metal forming research independently. The results of the experimental and theoretical investigations are discussed in each chapter rather than in the conclusions which is more customary. Section 10 which describes the design of the diaphragmless driver to convert the shock tube into a diaphragmless operating shock tube is treated as an independent chapter having a literature survey as part of it. This is done due to the fact that the experiments to test the performance of this driver have been carried out by operating the shock tube in the gas mode to allow comparisons to existing diaphragmless drivers.

Published Work

Aspects of this thesis have been published in the following references:

- Kosing, O.E. and Skews, B.W., The use of liquid shock waves for metal forming, Proceedings of the 21st International Symposium on Shock Waves, Australia (July 1997)
- Kosing, O.E. and Skews, B.W., High speed metal forming with liquid shock waves, R&D Journal South Africa, (Nov. 1997)
- Kosing, O.E. and Skews, B.W., High speed metal forming in a liquid shock tube, Proceedings of the 2nd South African Conference on Applied Mechanics, Cape Town (January 1998)
- Kosing, O.E. and Skews, B.W., An investigation of high speed forming of circular plates in a liquid shock tube, International Journal of Impact Engineering, Vol. 21, (Sep. 1998)
- Kosing, C.E., Barbosa, F.J, Skews, B.W., A new, friction released, piston actuated diaphragmless shock tube driver, Shock Waves, (accepted for publication)
- Kosing, O.E., Skews, B.W., High speed metal forming of circular disks and cylindrical tubes in a liquid shock tube, Proceedings of the 5th International Conference on Structures under Shock and Impact, Greece (June 1998)

Contents

Declaration i

Acknowledgements iii

Abstract v

The Contribution of this Work vii

Published Work ix

Contents x

List of Figures xiv

List of Tables xxii

List of Symbols xxiv

1 INTRODUCTION 1

2 SHOCK WAVES 4

2.1 SHOCK WAVES IN GASES 5

2.1.1 BLAST WAVES 8

2.2 SHOCK WAVES IN LIQUIDS 9

3 HIGH SPEED METAL FORMING 12

4 EXPERIMENTAL SET - UP 17

4.1 THE SHOCK TUBE 17

4.1.1 SET - UP FOR GAS SHOCK WAVES 18

4.1.2 SET - UP FOR LIQUID SHOCK WAVES - AIR MODE . . 18

4.1.3 SET - UP FOR LIQUID SHOCK WAVES - PROJECTILE MODE 21

4.2 TEST SECTIONS 23

4.3 OPTICAL SET - UP 24

4.4 TEST SPECIMEN 27

5 OPERATING CYCLE OF THE LIQUID SHOCK TUBE IN THE AIR MODE 30

6 OPERATING CYCLE AND ENERGY TRANSFER OF THE LIQUID SHOCK TUBE IN PROJECTILE MODE 33

6.1 KINETIC ENERGY OF THE PROJECTILE 33

6.1.1 THEORETICAL CALCULATION AND EXPERIMENTAL RESULTS OF PROJECTILE IMPACT VELOCITY 33

6.2 PRESSURE ENERGY OF THE LIQUID SHOCK WAVE 37

6.2.1 THEORETICAL CALCULATIONS AND EXPERIMENTAL RESULTS 37

6.3 DEFORMATION ENERGY OF THE WORKPIECE 46

7 THE EFFECT OF THE PROJECTILE GEOMETRY, MASS AND MATERIAL ON THE PRESSURE HISTORY OF THE LIQUID SHOCK WAVE 47

7.1 EXPERIMENTAL RESULTS WITH DIFFERENT PROJECTILE MASSES AND MATERIALS 47

7.2 EXPERIMENTAL RESULTS WITH DIFFERENT PROJECTILE GEOMETRIES 50

7.3 FINITE ELEMENT MODELING OF THE PRESSURE HISTORY 56

8 FORMING OF CIRCULAR METAL DISKS 62

8.1 STRAINS AND STRESSES OF DEFORMED METAL PLATES . . 62

8.1.1 DEFORMATION ENERGY FOR CIRCULAR PLATES . . 66

8.2 PREDICTION OF MIDPOINT DEFLECTION 70

8.3 OPTICAL INVESTIGATIONS OF THE DEFORMATION PROCESS 74

8.3.1 DEFLECTION TIME HISTORY AND DEFORMATION VELOCITY 74

8.3.2 STRAIN RATES 81

8.3.3 STRAIN RATE MEASUREMENTS DURING THE DEFORMATION PROCESS 82

8.3.4 FINITE ELEMENT MODELING OF THE DEFORMATION PROCESS 85

9 FORMING OF CYLINDRICAL METAL TUBES 93

9.1 FOCUSING OF THE LIQUID SHOCK WAVE INTO THE CYLINDRICAL TEST TUBE BY MEANS OF A NOZZLE 93

9.2 STRAINS AND STRESSES OF DEFORMED METAL TUBES . . 94

9.2.1 DEFORMATION ENERGY FOR CYLINDRICAL TUBES . 99

9.3 OPTICAL INVESTIGATION OF THE DEFORMATION PROCESS 99

9.3.1 DEFLECTION TIME HISTORY 100

9.3.2 STRAIN RATES 102

9.4 FORMING OF CYLINDRICAL TUBES INTO DIES 103

10 CONVERSION OF THE SHOCK TUBE TO DIAPHRAGMLESS OPERATION 109

10.1 THE DIAPHRAGMLESS WATER SECTION 109

10.2 THE DIAPHRAGMLESS DRIVER 110

10.2.1 PREVIOUS WORK 111

10.2.2 DESIGN 113

10.2.3 EXPERIMENTAL RESULTS 116

10.3 PERFORMANCE OF THE DIAPHRAGMLESS SHOCK TUBE IN PROJECTILE MODE 119

11 CONCLUSION 121

REFERENCES 125

List of Figures

2.1 Shock waves from lightning; lightning strokes over Downtown Johannesburg 5

2.2 Generation of a gas shock wave in a shock tube 7

2.3 One-dimensional calculated wave diagram 8

2.4 Comparison of a shock wave a) and an blast wave b) 9

3.1 The idealised mode of deformation in a fully clamped circular disk under impulsive load [15] 14

3.2 Axisymmetric radial velocity field for a fully clamped cylindrical tube [13] 15

4.1 Schematic arrangement of the gas shock tube 19

4.2 Schematic arrangement of the liquid shock tube in air mode 20

4.3 Schematic arrangement of the liquid shock tube in projectile mode . 22

4.4 Test section for circular disks 23

4.5 Test section for cylindrical tubes containing the hexagonal die 24

4.6 Test section for optical investigations of cylindrical tubes 25

4.7 Design of test specimen to simulate flat disks 26

4.8 Optical set-up of the shadow system, top view 26

4.9 Test section for optical investigations of circular disks and set-up for strain rate measurements, side view 27

4.10 Effect of strain rate on flow stress of 99.999% copper [31] 28

4.11 Effect of strain rate on strain hardening coefficient for mild steel [32] 28

5.1 Liquid shock wave pressure versus burst pressure in driving section . 31

5.2 Pressure history for a liquid shock wave, generated with an air shock wave. Transducer 1, 2, and 3 32

6.1 Comparison of experimental projectile velocities and calculated values by using eqn. 6.1 35

6.2 Comparison of calculated and experimental values for steel projectile (3.665 kg) velocity 36

6.3 Comparison of calculated and experimental values for aluminium projectile (0.87 kg) velocity 36

6.4 Comparison of calculated and experimental values for plastic projectile (0.2 kg) velocity 37

6.5 x-t wave diagram with expansion and compression characteristics of a compressed fluid in a shock tube 38

6.6 Comparison of calculated maximum shock wave pressure and experimental results performed with a steel projectile (3.665 kg) 40

6.7 Comparison of calculated shock wave pressure and experimentally measured shock wave pressure for the 3.665 kg steel projectile 41

6.8 Calculated results of steel projectile (3.665 kg) deceleration for an impact velocity of 42.9 m/s 42

6.9 Calculated results of steel projectile (3.665 kg) displacement for an impact velocity of 42.9 m/s 42

6.10 Comparison of calculated maximum shock wave pressure and experimental results performed with a plastic projectile (0.2 kg) 43

6.11 Comparison of the calculated shock wave pressure and the measured one for the (0.2 kg) plastic projectile 43

6.12 Calculated results of plastic projectile (0.2 kg) deceleration for an impact velocity of 91 m/s 44

6.13 Calculated results of plastic projectile (0.2 kg) displacement for an impact velocity of 91 m/s 44

6.14 Comparison of the calculated shock wave pressure and the measured one for the (0.87 kg) aluminium projectile 45

6.15 Comparison of calculated shock wave and experimentally measured shock wave for the aluminium projectile (0.87 kg) 45

7.1 Maximum shock wave pressure versus pressure in driving section . . 48

7.2 Shock wave energy versus pressure in driving section 49

7.3 Shock wave impulse versus pressure in driving section 49

7.4 Projectile dimensions for single and double stepped projectiles . . . 50

7.5 Steel projectile (3.665 kg), plane surface, impact velocity 39.6 m/s, Transducer 1, 2 and 3 51

7.6 Steel projectile (3.198 kg), short step, impact velocity 37.5 m/s, Transducer 1, 2 and 3 51

7.7 Steel projectile (3.85 kg), long step, impact velocity 37.5 m/s, Transducer 1, 2 and 3 52

7.8 Steel projectile (3.054 kg), double step, volume ratio $\sim$ 0.3, impact velocity 39.0 m/s, Transducer 1, 2 and 3 52

7.9 Steel projectile (3.054 kg), double step, volume ratio $\sim$ 0.5, impact velocity 39.0 m/s, Transducer 1 53

7.10 AUTODYN 2D-model: Liquid shock wave pressure history for the impact of the 3.665 kg steel piston. $V_{imp} = 40\ m/s$. Transducer position 1,2,3 57

7.11 Experimental liquid shock wave pressure history for the impact of the 3.665 kg steel projectile. $V_{imp} \sim 50\,m/s$. Transducer position 1,2,3 . 58

7.12 AUTODYN 2D-model: Velocity field at the end of the liquid shock tube just after wave reflection (velocity scale units in $[cm/\mu s]$ and dimension scale units in $[cm]$) 58

7.13 AUTODYN 2D-model: Liquid shock wave pressure history for the impact of the 0.2 kg plastic projectile. $V_{imp} = 50\,m/s$. Transducer position 1,2,3 59

7.14 Experimental liquid shock wave pressure history for the impact of the 0.2 kg plastic projectile. $V_{imp} \sim 70\,m/s$. Transducer position 1,2,3 . 60

7.15 AUTODYN 2D-model: Liquid shock wave pressure history for the impact of the single stepped projectile [short] 61

8.1 Measurements of circumferential and radial strains 63

8.2 Pictures of deformed copper disks. Thickness 0.55 mm. From left to the right hand side: 10.95, 13.45, 14.4, 16.15 mm midpoint deflection 63

8.3 Pictures of deformed copper disks. Thickness 0.9 mm. From left to the right hand side: 16.03, 17.22, 17.5, 19.0 mm midpoint deflection . 63

8.4 Variation of height and thickness for a 0.55 mm copper disk after impact of a shock wave with $p_{max} = 25.56\,MPa$, $E = 116.96\,J$ and $I = 10.97\,Ns$ 64

8.5 Variation of natural strains for a 0.55 mm copper disk after impact of a shock wave with $p_{max} = 25.56\,MPa$, $E = 116.96\,J$ and $I = 10.97\,Ns$ 64

8.6 Variation of stresses for a 0.55mm copper disk after impact of a shock wave with $p_{max} = 25.56MPa$, $E = 116.96J$ and $I = 10.97Ns$ 65

8.7 Geometry of circular ring element 66

8.8 Pressure history for a liquid shock wave impacting on a copper specimen 68

8.9 Pressure history for a liquid shock wave impacting on a mild steel specimen 68

8.10 Geometry of deformed disk 71

8.11 Comparison of calculated and experimental midpoint deflection for 0.55 mm copper plates 72

8.12 Comparison of calculated and experimental midpoint deflection for 0.9 mm copper plates 73

8.13 Comparison of calculated and experimental midpoint deflection for 1.6 mm mild steel plates 73

8.14 Comparison of calculated and experimental midpoint deflection for 1.0 mm and 0.5 mm mild steel plates 74

8.15 Pictures and local deformation velocities on the centre line of a copper specimen with a thickness of 0.55 mm. The maximum pressure of the shock wave is $p = 28.6\ MPa$, the impulse $I = 9.85\ Ns$ and the shock wave energy $E = 107.25\ J$ 76

8.16 Pictures and local velocities on the centre line of two copper specimen with a thickness of 0.9 mm. $p_a = 36.4\ MPa$, $I_a = 11.8\ Ns$, $E_a = 162\ J$; $p_b = 40\ MPa$, $I_b = 11.64\ Ns$, $E_b = 181\ J$ 77

8.17 Pictures and local deformation velocities on the centre line of a mild steel specimen with a thickness of 1.0 mm. The maximum pressure of the shock wave is $p = 65.0\ MPa$, the impulse $I = 17.74\ Ns$ and the shock wave energy $E = 449.3\ J$ 79

8.18 Average deformation velocity versus maximum deformation 80

8.19 Average deformation velocity versus shock wave energy 80

8.20 Average deformation velocity versus shock wave impulse 81

8.21 Strain rates versus liquid shock wave energy, circular disks 82

8.22 Side and bottom view of deforming copper specimen showing two superimposed pictures at 122 μs and 244 μs 83

8.23 Deformation and local strain rates of the copper plate at 122 μs . . . 84

8.24 Deformation and local strain rates of the copper plate at 244 μs . . . 85

8.25 AUTODYN 2D-model: Deformation of a 0.9 mm copper plate at 23 μs after impact of liquid shock wave (velocity scale units in $[cm/\mu s]$ and dimension scale units in $[cm]$) 88

8.26 AUTODYN 2D-model: Deformation of a 0.9 mm copper plate at 73 μs after impact of liquid shock wave (velocity scale units in $[cm/\mu s]$ and dimension scale units in $[cm]$) 88

8.27 AUTODYN 2D-model: Deformation of a 0.9 mm copper plate at 123 μs after impact of liquid shock wave (velocity scale units in $[cm/\mu s]$ and dimension scale units in $[cm]$) 89

8.28 AUTODYN 2D-model: Deformation of a 0.9 mm copper plate at 173 μs after impact of liquid shock wave (velocity scale units in $[cm/\mu s]$ and dimension scale units in $[cm]$) 89

8.29 AUTODYN 2D-model: Deformation of a 0.9 mm copper plate at 223 μs after impact of liquid shock wave (velocity scale units in $[cm/\mu s]$ and dimension scale units in $[cm]$) 90

8.30 AUTODYN2D-model: Deformation of a 0.9 mm copper plate at 273 μs after impact of liquid shock wave (velocity scale units in $[cm/\mu s]$ and dimension scale units in $[cm]$) 90

8.31 AUTODYN 2D-model: Contour plot at 23 μs after impact of liquid shock wave on the specimen (pressure in $[gm/(cm\,\mu s^2)]$) 91

8.32 AUTODYN 2D-model: Contour plot at 73 μs after impact of liquid shock wave on the specimen (pressure in $[gm/(cm\,\mu s^2)]$) 91

8.33 AUTODYN 2D-model: Liquid shock wave pressure history 92

8.34 AUTODYN 2D-model: Deformation velocity measured in the centre of the 0.9 mm copper plate 92

9.1 Euler model at $t = 4\ \mu s$ 94

9.2 Euler model at $t = 12\ \mu s$ 94

9.3 Euler model at $t = 20\ \mu s$ 94

9.4 Euler model at $t = 28\ \mu s$ 94

9.5 Pressure history for an aluminium projectile (0.87 kg) with focusing nozzle at the bottom end of the shock tube, Transducer 1, 2, 3 and 4 95

9.6 Pictures of deformed mild steel tubes. Maximum diameter increases from left to right hand side [mm]:24.1, 26.0, *torn* 96

9.7 Pictures of deformed copper tubes. Maximum diameter increases from left to right hand side [mm]:21.4, 24.7, 25.2, 25.4, 26.35, 26.6, *torn* 96

9.8 Change of diameter versus length of deformed mild steel tubes . . . 96

9.9 Change of diameter versus length of deformed copper tubes 97

9.10 Variation of natural strains for a copper tube with a wall thickness of 1.4 mm after impact of the liquid shock wave with $p_{max} = 53.2\ MPa$, $E = 691.7\ J$, $I = 37.6\ Ns$ 98

9.11 Variation of stresses for a copper tube with a wall thickness of $1.4mm$ after impact of a liquid shock wave with $p_{max} = 53.2MPa$, $E = 691.7J$, $I = 37.6Ns$ 98

9.12 Pictures of the deformation process of copper tubes a.) $p = 58.3\ MPa$, $I = 35.6\ Ns$, $E = 683.4\ J$ b.) $p = 42.8\ MPa$, $I = 31.6\ Ns$, $E = 509.5\ J$101

9.13 Deformation velocity at different points of the tube 102

9.14 Strain rates versus liquid shock wave energy, cylindrical tubes 103

9.15 Schematic drawing of cylindrical die for tube forming 105

9.16 $\emptyset\, 24mm$ cylindrical die with a deformed mild steel tube, 1.6 mm wall thickness after impact of a shock wave with $P_{max} = 66.4\ MPa$, $I = 122.2\ Ns$, $E = 3113.23\ J$ 105

9.17 Schematic drawing of the octagonal die for tube forming 107

9.18 Hexagonal die with a deformed copper tube, 1.2 mm wall thickness after impact of a liquid shock wave with $P_{max} = 62.12\ MPa$, $I = 40.3\ Ns$, $E = 892.4\ J$ 107

10.1 Schematic drawing of slotted interim section 110

10.2 Three adapter rings 114

10.3 Arrangement of piston chamber with brake pad and hollow aluminium piston 115

10.4 Schematic arrangement of the diaphragmless shock tube driver . . . 115

10.5 Efficiency of the diaphragmless driver 117

10.6 Shock wave development 117

10.7 Pressure History, Mach 1.44 119

List of Tables

2.1 Values for n (water) 9

7.1 Test results for the single step projectile [short] 54

7.2 Test results for the single step projectile [long] 54

7.3 Test results for the double step projectile [volume ratio ~ 0.3] 55

7.4 Test results for the double step projectile [volume ratio ~ 0.5] 55

7.5 AUTODYN 2D results for the single step projectile [short] 61

8.1 Comparison of deformation energy with shock wave energy for machined copper and mild steel specimen and for sheet material 69

8.2 Basic strain rate effects and thermodynamic conditions [12] 81

9.1 Deformation energy for cylindrical copper and mild steel tubes . . . 100

9.2 Filling grade and energy requirements for forming of mild steel tubes ($1.6\ mm$) into cylindrical dies 104

9.3 Filling grade and energy requirements for forming of mild steel tubes ($1.24\ mm$) into cylindrical dies 104

9.4 Filling grade and energy requirements for forming of copper tubes ($1.2\ mm$) into the hexagonal die 106

9.5 Filling grade and energy requirements for forming of copper tubes ($1.2\ mm$) into the octagonal die 108

10.1 Plastic projectile: Results for tests with diaphragmless liquid shock tube 120

10.2 Steel projectile: Results for tests with diaphragmless liquid shock tube 120

List of Symbols

a	Speed of sound
A	Area
B	Bulk modulus
C	Secant modulus
D	Diameter, Deflection
E	Energy
h	Enthalpy, Height
I	Impulse
K	Strength coefficient
L	Length
M	Mach number
m	Mass
n	Isentropic exponent, Strain hardening index
P	Compression characteristic
p	Pressure
Q	Expansion characteristic
R	Radius, Specific gas constant
r	Radial displacement

s	Entropy
t	Time
T	Temperature, Thickness
u	Velocity in X direction
V	Volume, Velocity
W	Deformation work
x	X coordinate
y	Y coordinate
α	Dimensionless number
γ	Specific heat ratio
ϵ	Strain
$\dot{\epsilon}$	Strain rate
ν	Poisson's ratio
ρ	Density
σ	Stress

1 INTRODUCTION

'High Speed Metal Forming' is a procedure of forming or shaping of metals by applying energy delivered over a short period of time and thus forming the metal at a speed which is appreciably higher than in conventional forming processes. High speed metal forming was invented at the end of last century and finds implementation in explosive, electro-hydraulic and electro-magnetic forming. The most common technique is explosive forming with chemical charges. The reasons for the development of high speed metal forming are e.g. [1]:

- for production of small runs, particularly of physically bulky items
- to avoid the manufacturing of male dies
- to avoid interstage annealing
- to reduce the time of forming
- for forming of difficult materials
- for forming of difficult shapes
- for the production of large parts

The advantage of forming with liquid shock waves in a shock tube in comparison to explosive forming is better control of the process and increased safety. High speed metal forming using liquid shock waves is characterised by a rapid release of energy. The potential energy stored in the driving section is transformed into the kinetic energy of an air shock wave (Air Mode) or into the kinetic energy of a fast moving projectile (Projectile Mode). With the impact of either the air shock wave or the projectile on a liquid surface, the kinetic energy is transformed into hydraulic pressure and a liquid shock wave is generated. The energy associated with the hydraulic pressure is used to form the work piece.

The high speed metal forming in a liquid shock tube can be carried out by operating the shock tube in two different modes (Projectile Mode and Air Mode). In both modes the potential energy of compressed gas is used.

In the air mode an air shock wave is generated after the bursting of a diaphragm which separates the driving section of the shock tube from the driven section. The shock wave travels down the driven section and impacts on the water surface. With the impact of the air shock wave the liquid shock wave is generated.

In the projectile mode the energy stored in the compressed gas is converted into kinetic energy of a projectile after bursting of the diaphragm. With the impact of the projectile on the water surface, the kinetic energy is converted into pressure energy in the liquid. The impacting projectile pressurises and accelerates the water. During the impact process the projectile is decelerated. This leads to a pressure drop of the shock wave, which results in a shock wave pressure profile similar to that of a blast wave. The pressure energy of this liquid shock wave is used to form the workpiece to the desired shape.

The design of the system in the projectile mode permits precise control of the total amount of energy delivered to the workpiece, and of the rate at which the energy is available. The total amount of energy is determined by the bursting pressure in the driving section, and the rate at which the energy is delivered is defined by the mass, the material, and the geometry of the projectile. These parameters allow an exact tailoring of the liquid shock wave which favours the projectile mode in comparison to the air mode.

In section 2 a review is given on shock waves. The generation of shock waves in a shock tube is discussed and the basic theory is presented. Particular attention is drawn to explosion waves and shock waves in liquids.

Section 3 presents a literature survey on the subject of 'High Speed Metal Forming' and several experimental results and theoretical models are presented and discussed.

The experimental set-up is described in section 4. The configuration and the dimensions of the shock tube for the generation of gas shock waves and for the generation of liquid shock waves in the air and projectile mode are given. The design of the test sections and the optical set-up is presented and the material properties of the test specimens are discussed.

A brief description of the operating cycle of the liquid shock tube in the air mode is given in section 5 and experimental results of the shock wave pressure are presented

in comparison to theoretical considerations.

The operating cycle of the shock tube in the projectile mode is discussed in detail in section 6. Theoretical models are presented to predict the complete energy transformation process in the liquid shock tube and the results are discussed in comparison with experiments.

In section 7 experimental results are presented to demonstrate the effect of different projectile masses, materials and geometries. A finite element program is employed to simulate the generation and the propagation of the liquid shock wave numerically.

The forming of circular metal plates is described in section 8. The strains and stresses of the deformed plates are determined experimentally. The deformation energy of the metal specimen is calculated and a theoretical approach is presented to predict the midpoint deflection of circular disks. The results of the optical investigations of the deformation process are reviewed and the strain rates of the deformation process are determined. The impact of a liquid shock wave on a circular plate in a shock tube is modeled numerically by using a finite element program. The results are discussed with respect to experimental results.

The forming of cylindrical tubes is discussed in Section 9. The focusing of the liquid shock wave through a nozzle into the tubes is described. The strain and stress behaviour is determined from the deformed tubes and the deformation energy is calculated. The deformational behaviour is optically investigated and the results of the strain rate calculations are given. The forming of tubes into cylindrical, hexagonal and octagonal dies is discussed and the results are presented.

The conversion of the liquid shock tube into a diaphragmless shock tube is described in section 10. The design of the diaphragmless water section and the diaphragmless driver is reviewed and experimental results are presented to estimate the performance of the modified shock tube.

Section 11 contains the conclusions of this thesis and recommendations for further work.

2 SHOCK WAVES

The most common experience of shock waves in nature is the crack and rumble of thunder following a flash of a lightning. This lightning-thunder phenomenon is one of the brightest flashes and most intense sounds in nature. The flash, which arrives in view with the speed of light, is generated by a sudden deposition of a huge quantity of electrical energy in a very narrow channel. The expanding, hot, high-pressure channel drives a cylindrical shock wave in front of it, which follows the flash. In Fig. 2.1 a photograph of lightning strokes over Downtown Johannesburg is shown. The picture shows lightening channels just generated (thin) and in expanding motion (thick). The shock wave radius expands with time and the intensity decreases by heating and compressing ever greater volumes of air [2].
Other shock waves that occur in nature are generated by volcanic explosions, meteor impact and earthquakes. Shock waves generated by man are widely known e.g. from aeroplanes flying at supersonic speed or from the destructive force of chemical or nuclear explosions. Not as widespread is the knowledge of the use of shock waves in research. For research purposes shock waves are used in the aerodynamic, chemical and medical fields. Here the most common tool for generating shock waves is the shock tube.

The phenomenon of shock waves can be explained by considering the following simplified situation:
A small disturbance in a medium is signaled by means of a wave travelling at the local velocity of sound. If a body is travelling through this medium at a velocity less than the speed of sound the information of the presence of this body is signaled with the speed of sound to the medium ahead of it so that the medium is able to adjust to the movement of the body. This results in a gradual change in the flow properties with a smooth and continuous streamline. The behaviour of the flow is totally different for a body moving with a velocity higher than the speed of sound. Since the information on the presence of the body is only delivered with the speed of sound, the medium is unable to sense the approach of the body. Therefore the flow properties change abruptly and a shock wave is generated.



Figure 2.1: Shock waves from lightning; lightning strokes over Downtown Johannesburg

2.1 SHOCK WAVES IN GASES

For a perfect compressible gas in the one-dimensional case and in a frame of reference fixed on the wave the equations for conservation of mass, momentum and energy can be written as [3]:

Conservation of mass:
$$\rho_1 u_1 = \rho_2 u_2 \tag{2.1}$$

Conservation of momentum:
$$\rho_1 u_1^2 + p_1 = \rho_2 u_2^2 + p_2 \tag{2.2}$$

Conservation of energy:
$$h_1 + \frac{u_1^2}{2} = h_2 + \frac{u_2^2}{2} \tag{2.3}$$

The perfect gas law is:

$$p = \rho RT \tag{2.4}$$

where R is the specific gas constant.

From the second law of thermodynamics and for an isentropic process follows:

$$Tds = dh - \frac{dp}{\rho} = 0 \tag{2.5}$$

For a perfect gas with constant specific heats undergoing an isentropic process the equation of state can be written:

$$\frac{p_2}{p_1} = \left(\frac{\rho_2}{\rho_1}\right)^{\gamma} \tag{2.6}$$

An important quantity for compressible gas flows is the Mach Number M, which gives a relation between the local velocity and the velocity of sound. The speed of sound can be calculated by using the following equation:

$$a = \sqrt{\left(\frac{\partial p}{\partial \rho}\right)_s} \tag{2.7}$$

For an ideal gas and by using both the equation of state (eqn. 2.6) and the perfect gas law (eqn. 2.4), the speed of sound can be calculated:

$$a = \sqrt{\gamma RT} \tag{2.8}$$

The process of generating shock waves in gas shock tubes can easily be described by assuming a simplified shock tube consisting of a high pressure driver, a diaphragm and a driven section (see Fig. 2.2a). With the bursting of the diaphragm the high pressure gas in the driver section (condition 4) can discharge into the driven section (condition 1) and a series of finite compression waves is generated (Fig. 2.2c). The compression waves increase the temperature of the gas which leads to an increase of the speed of sound behind each compression wave (see equation 2.8). This leads to the following compression waves travelling with a slightly higher velocity than the initial wave (condition 2) and thus eventually catching up with it. The compression waves steepen up to a shock wave.

The variation of variables through the shock wave are very large (yet not infinite), and the shock can be approximated by a discontinuity that is moving with a velocity higher than the speed of sound. The contact surface between the driver gas and the driven gas is moving with a speed less than the speed of the shock wave and

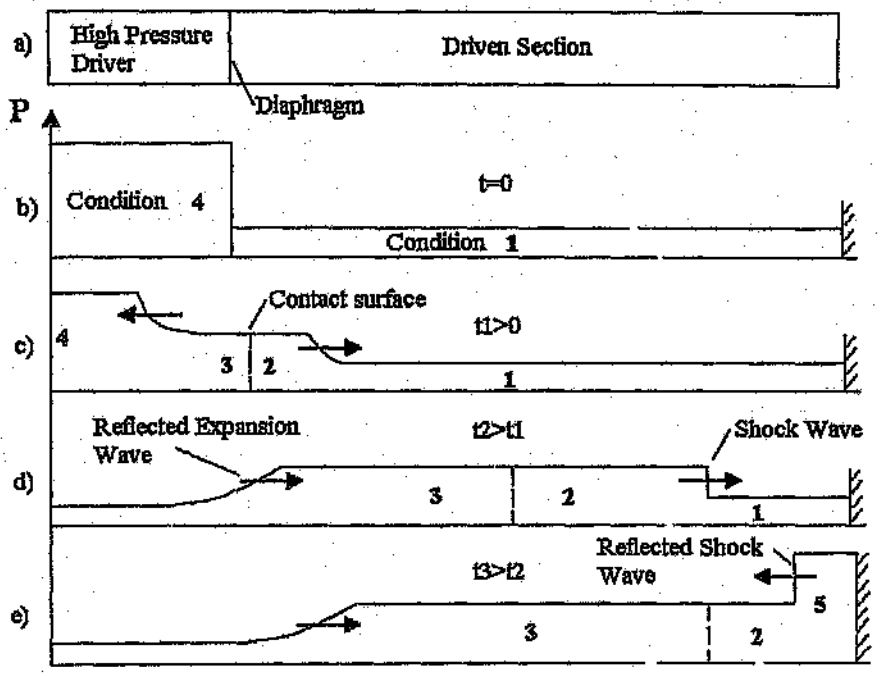

Figure 2.2: Generation of a gas shock wave in a shock tube

therefore stays behind it.

With the bursting of the diaphragm a series of expansion waves travel into the driving section (Fig 2.2c). The expansion waves cannot steepen up and form a discontinuity like the compression waves do since each expansion wave reduces the gas temperature. Therefore the sound velocity behind each expansion wave is smaller and they can not catch up with the leading wave front.

At the end walls of the shock tube both the shock wave and the expansion wave get reflected (Fig 2.2d and 2.2e). Typical behaviour of shock and expansion waves is given in a wave diagram, in the x-t plane as shown in Fig. 2.3. The wave diagram was calculated by using a one-dimensional shock tube simulation program [4]. For the calculations the dimensions of the existing gas shock tube have been taken (see Fig. 4.1). The pressure in the driven section was set to 5 bar.

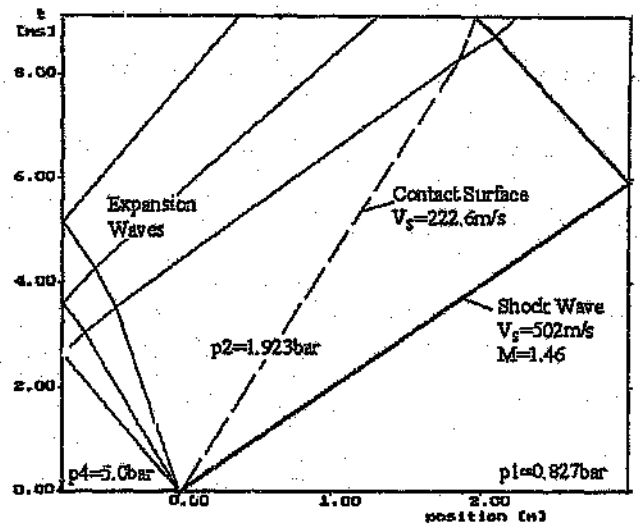

Figure 2.3: One-dimensional calculated wave diagram

2.1.1 BLAST WAVES

Blast waves, which belong to the family of shock waves, are characterised by a pressure jump similar to a normal shock wave and an exponential pressure drop immediately after the shock. In Fig. 2.4 a comparison between an blast wave and a normal shock wave is shown.

Blast waves occur after firing an explosive charge. The explosion of the charge generates a pressure wave which steepens up to a shock wave. Since there is no pressure reservoir to keep the pressure behind the shock wave constant, the pressure drops immediately. Blast waves can also be generated in shock tubes by using a very short driver section. The reflected expansion wave travels in the same direction as the shock wave and catches up to it, which leads to the pressure drop behind the initial shock wave.

The energy and the impulse of an blast wave can be calculated precisely (Cole [5]). Using the pressure trace from the experiment, the energy and the impulse can be numerically integrated by using the equations given by Müller [6].

$$E = \frac{A}{\rho_1 a_1} \int_{t_1}^{\infty} (p - p_1)^2 \, dt \tag{2.9}$$

$$I = A \int_{t_1}^{\infty} p(t) dt \tag{2.10}$$

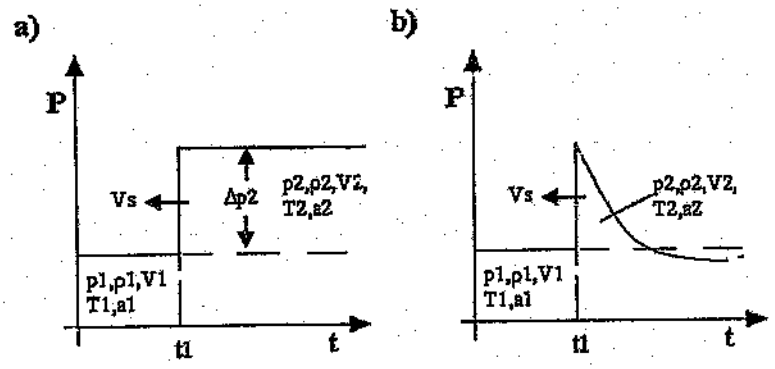

Figure 2.4 Comparison of a shock wave a) and an blast wave b)

2.2 SHOCK WAVES IN LIQUIDS

To describe shock waves in liquids, Kirkwood et al. [7] suggest a modified state equation:

$$\frac{\rho(p,T)}{\rho(1bar,T)} = \left(1 + \frac{p}{B(T)}\right)^{-1/n} \tag{2.11}$$

B is the Bulk Modulus and can be described with the empirical equation given by Müller [6]. For a room temperature of $20^o\ C$ the bulk modulus for water is $B = 2995\ bar$ and the variation of temperature (T in $[^o\ C]$) is given by:

$$B(T) = \left(2996 + 7.285\,(T-25) - 0.179\,(T-25)^2 + 6.13 \cdot 10^{-4}\,(T-25)^3\right) bar$$

The value n is also a function of the pressure and the temperature. Richardson et al. [8] suggested the following table for water:

$T[C]$	$500\ MPa$	$1500\ MPa$	$2500\ MPa$
20	7.211	7.188	7.130
40	7.360	7.126	6.969
60	7.411	7.054	6.868

Table 2.1: Values for n (water)

In the temperature region of $293\ K \leq T \leq 333\ K$ the differences in the values of B and n are smaller than 4% and therefore these values are kept constant. As shown by Holl [9] the state equation mentioned above can be treated as isentropic up to

shock wave pressures of $p_2 = 1000\ MPa$. Therefore the isentropic state equation can be written as:

$$\frac{\rho_2}{\rho_1} = \left(\frac{p_2 + B}{p_1 + B}\right)^{1/n} \tag{2.12}$$

In his work Holl introduces a modified pressure $p' = p + B$ (see also Cole [5]). Using this modified pressure and an exchange of the specific heat ratio γ with n, the gas dynamic laws can be transformed to describe shock waves in liquids. These transformations with the assumptions mentioned above, give good results for small pressures. In comparison with the exact solution the error is less than 1.3% for pressures up to $p_2 = 1000\ MPa$. For the one-dimensional case the equations of conservation can now be written:

Conservation of mass: $$\rho_1 u_1 = \rho_2 u_2 \tag{2.13}$$

Conservation of momentum: $$\rho_1 u_1^2 + p_1' = \rho_2 u_2^2 + p_2' \tag{2.14}$$

Conservation of energy: $$h_1 + \frac{u_1^2}{2} = h_2 + \frac{u_2^2}{2} \tag{2.15}$$

For an isentropic process we can now write:

$$h_2 - h_1 = \frac{n}{n-1}\frac{p_2'}{\rho_2} - \frac{n}{n-1}\frac{p_1'}{\rho_1} \tag{2.16}$$

These transformations can also be used for the calculation of the speed of sound in water. The speed of sound is defined as:

$$a^2 = \frac{\partial p}{\partial \rho}\Big|_s \quad \Rightarrow \quad a^2 = \frac{\partial p'}{\partial \rho}\Big|_s \tag{2.17}$$

By using equation 2.11 with $B, n = const$, p'/ρ can be calculated:

$$\frac{p + B}{\rho^n} = \frac{B}{\rho_0^n} = const \tag{2.18}$$

After solving of equation 2.17 the speed of sound can be written as:

$$\frac{\partial p'}{\partial \rho}\Big|_s = \frac{B}{\rho_0^n} n \rho^{n-1} = n\frac{p'}{\rho}$$

$$a^2 = n\frac{p'}{\rho}$$

ρ can now be substituted by using eqn. 2.18:

$$a^2 = \frac{nB}{\rho_0}\left(\frac{p'}{B}\right)^{(n-1)/n} \tag{2.19}$$

3 HIGH SPEED METAL FORMING

The term 'High Speed Metal Forming' describes a manufacturing process in which the speed of the metal movement is appreciably higher than in conventional forming processes (see Davis and Austin [10]). Another term that describes high speed metal forming is 'High Energy Rate Forming' (HERF) which is often found in older literature. This older terminology is misleading since high energy is not characteristic for high speed metal forming.

Attempts have been made to define the term 'high speed' when applied to metal forming. e.g. Johnson [11] proposed a guide for assessing the behaviour of metal plates subjected to impact by using a dimensionless number defined as

$$\alpha = \frac{\rho V^2}{\sigma_d} \tag{3.1}$$

where V is the impact velocity, ρ the material density and σ_d the damage stress. In his work he defines a damage number of $\alpha = 1 \cdot 10^{-5}$ as quasi-static elastic behaviour, $\alpha = 1 \cdot 10^{-1}$ as moderate plastic behaviour, $\alpha = 1 \cdot 10^{1}$ as extensive plastic deformation and $\alpha = 1 \cdot 10^{3}$ as hypervelocity impact. In comparison to that Wilson [12] classifies high velocity forming by using the strain rates of the deformation process. A deformation process with strain rates of $0 - 0.003\ s^{-1}$ is considered as static, $0.003 - 10^2\ s^{-1}$ as intermediate and above $10^2\ s^{-1}$ as high velocity forming. Davies and Austin [10] define for conventional forming a metal speed of up to $4.5\ m/s$, for high speed billet forming a speed of up to $24\ m/s$ and for high speed sheet forming a speed from $30\ m/s$ up to $300\ m/s$.

Since high speed metal forming is a relatively new manufacturing technology simple geometries for the test samples like circular and rectangular disks and cylindrical tubes are often used for the study of this techniques. Therefore these structural shapes are usually discussed in literature and free forming and forming into dies is investigated with respect to deformation energy, deformation speed and behaviour of the test specimen during deformation. Theoretical investigations of the deformation process for plates and tubes have been conducted by Johnson [11] and Jones [13].

The three main conventional processes for high speed metal forming are electro-hydraulic, electro-magnetic and explosive forming. Electro-hydraulic and electro-magnetic forming are explained and described in detail in technical manufacturing books e.g. in [10] and [12].

Explosive forming is the most common technique. Most of the explosive forming processes use water as an energy transmission medium. The explosive charge generates a water shock wave which is utilised to form the workpiece. The use of water and the generation of a liquid shock wave makes this process comparable to the high speed metal forming in a liquid shock tube.

Since explosive forming has found great application in industry a lot of work has been published on this field. General descriptions of the process can be found in many technical manufacturing books e.g. [10], [12] and [14]. These books cover the forming of flat plates as well as the forming of cylindrical tubes.

Forming of flat disks:

The behaviour of a flat sheet under an impulsive load was first described by Hudson [15]. He describes a fully clamped plate subjected to an initial impulsive velocity normal to its own plane. The deformation of the plate commences at the outer part by forming a plastic hinge whilst the centre remains flat (see Fig. 3.1). Kiyota and Fujita [16] have conducted high speed photography experiments with lead plates subjected to explosive blasts in air and their tests confirm Hudson's theory with air as the energy transmitter. A literature review on the dynamic plastic response of structures has been conducted by Jones [17].

Investigations to determine the deflection time history of flat disks have been undertaken by Johnson et al. [18] and Nurick [19]. Johnson et al. used pin contactors for his experiments which give a signal when the deforming metal makes contact while Nurick measured the time history by using light diodes.

There have been many empirical / theoretical predictions for the deflection of plates subjected to impulsive loads. Most of the authors' approaches are a function of the imparted impulse, the plate thickness and radius, the density and the static yield stress of the material in combination with an empirical factor: e.g. Nurick [20] extended Johnsons damage number (see eqn. 3.1) in terms of impulse and added a dimensionless geometry number and a loading parameter to assess the behaviour of

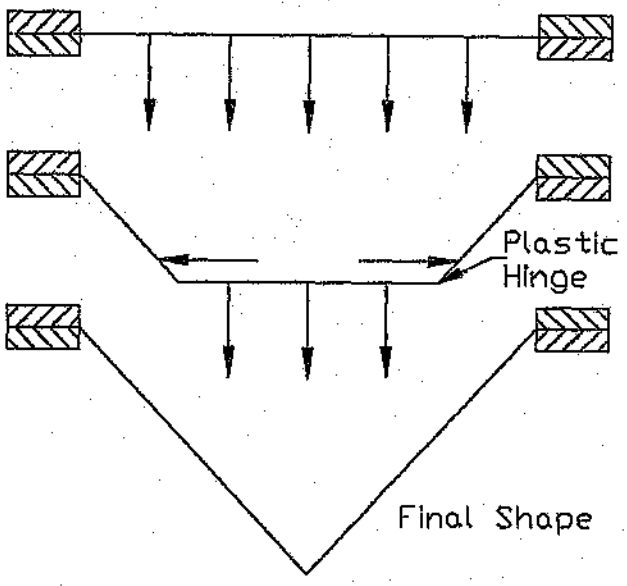

Figure 3.1: The idealised mode of deformation in a fully clamped circular disk under impulsive load [15]

plates with different dimensions under various loading conditions. With this modified damage number and an empirical factor the midpoint deflection of circular and rectangular disks can be predicted. Johnson [21] used an energy method by assuming a rigid linear strain-hardening material and a deformed shape. Duffey [22] used a rigid plastic energy method as well and assumed several deformed shapes, including sinusoidal and various polynomial forms, to find the best fit to experimental results. A review of these theoretical predictions is given by Nurick and Martin [23].

To improve the process of forming of flat disks Johnson et al. investigated the effect of the stand-off distance and hydrostatic head when explosively deep drawing circular plates (see [18, 21, 24]). The use of the plug-cushion technique to improve the quality of the deformed plates is described in [18], [24] and [25].

Forming of cylindrical tubes:

Jones' [13] theoretical analysis of fully clamped short cylindrical tubes subjected to an internal rectangular dynamic pressure pulse predicts a plastic hinge in the central region. In his approach the dynamic response consists of three phases of motion $0 \leqslant t \leqslant t_1$, $t_1 \leqslant t \leqslant t_2$, $t_2 \leqslant t \leqslant t_3$, where t_1 is the duration of the rectangular pressure pulse, t_2 is the time when the two travelling circumferential

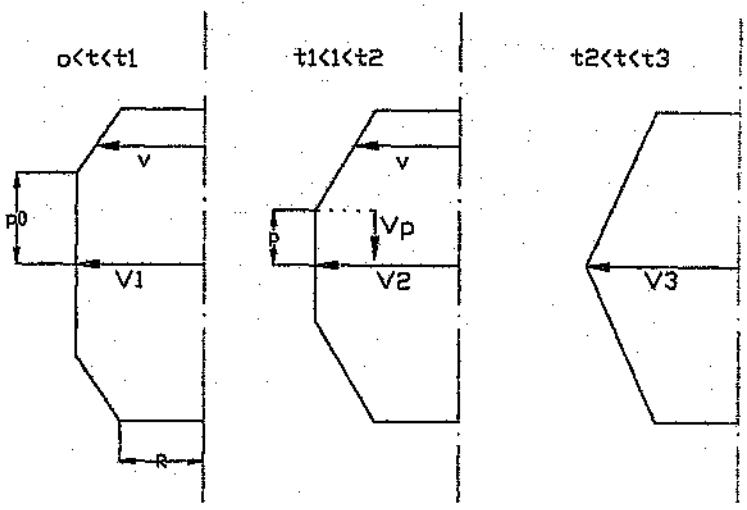

Figure 3.2: Axisymmetric radial velocity field for a fully clamped cylindrical tube [13]

plastic hinges coalesce and t_3 is the response duration. The radial velocity field for the three phases of motion can be seen in Fig. 3.2. For the first phase of motion the position of the plastic hinge is time independent. In the second phase of motion the plastic hinge starts to move towards the centre and with the plastic hinge reaching the centre the third phase of motion begins.

High speed photography experiments with aluminium tubes have been performed by Wedda et al. [26]. In each test the detonator was located on the axis of the tube, but at different points along the tube length. For a centered location of the detonator a symmetrical deformation could be achieved. The high speed photographs did not reveal the plastic hinge, which is most probably due to the detonation emerging from a point source. By placing the detonator at the upper part of the tube an unsymmetrical deformation with the maximum diameter closer towards the top was achieved.

Explosive expansion of water filled tubes has been investigated by Johnson et al. [27]. The detonation was generated by a line explosive charge along the axis which resulted in an axisymmetric deformation of the tube. The effect of different end caps was investigated. Light end caps out of cork which gave no resistance to the detonation and heavy end caps out of steel have been used. The results for the light end caps show nearly no deformation at the top and bottom end of the tube

whereas for the heavy end caps the top and the bottom part was nearly as deformed as the centre part. In addition Johnson et al. performed velocity measurements of the deforming tube by means of pin contactors.

Poynton et al. [28] performed tests with cylindrical brass tubes. In the experiments the ignition of a stoichiometric mixture of hydrogen and oxygen was used. The gaseous mixture was fired at the top end of the tube and caused a detonation wave, which traveled downwards. At the bottom end the detonation wave was reflected, which resulted in a pressure magnification. Due to the higher pressure the bottom of the tube deformed more than the centre. To place the maximum deformation at a desired location the authors also performed tests with an internal baffle.

The major difference between these previous studies of high speed metal forming of discs and tubes and the present investigations is that the current work does not use chemical explosives to generate the high pressure pulse in the liquid.

4 EXPERIMENTAL SET - UP

4.1 THE SHOCK TUBE

The design of the shock tube follows modular principles which allows a versatile usage of the shock tube. The shock tube can be used as an ordinary gas shock tube, as an air water shock tube, and as a projectile water shock tube. However the design is based on the designated principal use as a projectile water shock tube.

The modules of the shock tube are made from stainless steel with an inside diameter of 56 *mm* and a wall thickness of 25 *mm*. The modules have lengths of 502 *mm*, 752 *mm* or 1002 *mm* and the inside is honed smooth. In addition to the main modules several supplementary rings with the same inside and outside diameter are available and are used e.g. as gauge ports or water inlet rings. The whole tube is connected with clamp sledges to rails which are connected to a vertical beam to allow the opening of the tube. A counterbalance system simplifies the up and downwards sliding of the opened tube to exchange the diaphragms and to insert the projectile. The total length of the tube depends on the set-up and varies between 4.5 *m* and 6.5 *m*. The high pressure driver is located at the top of the tube and is separated from the driven section by means of a diaphragm. Several different test sections are available and can be connected to the bottom of the tube.

The high pressure driver, which is designed for a maximum pressure of 1000 *bar* is pressurised by using a HASKEL air driven gas booster (Model Double Air Head AGT-32/62). The booster uses the difference of areas principle to enable low pressure drive gas to pressurise the high pressure output gas. The HASKEL booster can supply gas with a maximum pressure of 620 *bar*. If the required pressure in the high pressure driver is less than 40 *bar* the driver is pressurised by using a commercial gas bottle.

4.1.1 SET - UP FOR GAS SHOCK WAVES

For the generation of gas shock waves the shock tube consists only out of the high pressure driver and the driven section. A schematic arrangement of the gas shock tube can be seen in Fig. 4.1. The tube can be operated with a rigid end wall or with an open end as shown in the figure. Four PCB pressure transducers of the A 24 series are incorporated in the driven section to measure the shock wave. The data is recorded with a four channel 150 MHz oscilloscope (Yokogawa DL 1540). The diaphragm that separates the driving section from the driven section is a polymer plastic. A needle system which is incorporated in the high pressure driver punctures the diaphragm to trigger the test.

4.1.2 SET - UP FOR LIQUID SHOCK WAVES - AIR MODE

If the liquid shock tube is used in the air mode, the liquid shock waves are generated by the impact of an air shock wave on the water surface. The experimental arrangement for the air mode is shown in Fig. 4.2. The shock tube consists of the high pressure driver, the driven section, the water section and the test section. With the discharge of the high pressure gas into the driven section an air shock wave develops and travels down the driven section. The liquid shock wave is then generated by the impact of the air shock wave on the water surface. The liquid shock wave travels down the water section and impacts on the test specimen which is located in the test section. The test section is connected to the bottom of the tube.

The air shock wave is recorded by three pressure transducers of the PCB A 24 series in the driven section. The data is recorded by a computer oscilloscope. The pressure history of the liquid shock wave is recorded by using three to four PCB A 23 or M109A pressure transducers and the data is recorded with the Yokogawa oscilloscope.

To obtain substantial strong shock waves for metal forming high pressures of up to 400 bar are required in the driving section to supply enough energy to the water column. To sustain these high pressures metal diaphragms have to be used for separating the high pressure driver. These metal diaphragms have a machined groove of 20% depth to open properly. Aluminium diaphragms were used with thicknesses up to 3 mm.

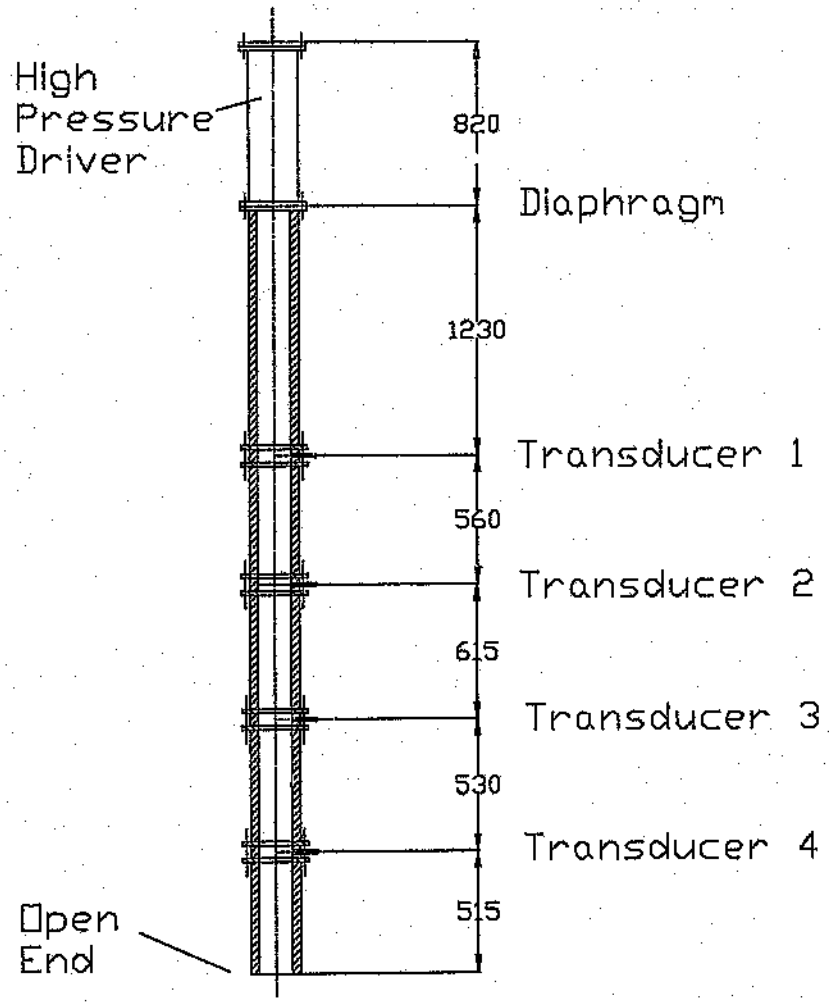

Figure 4.1: Schematic arrangement of the gas shock tube

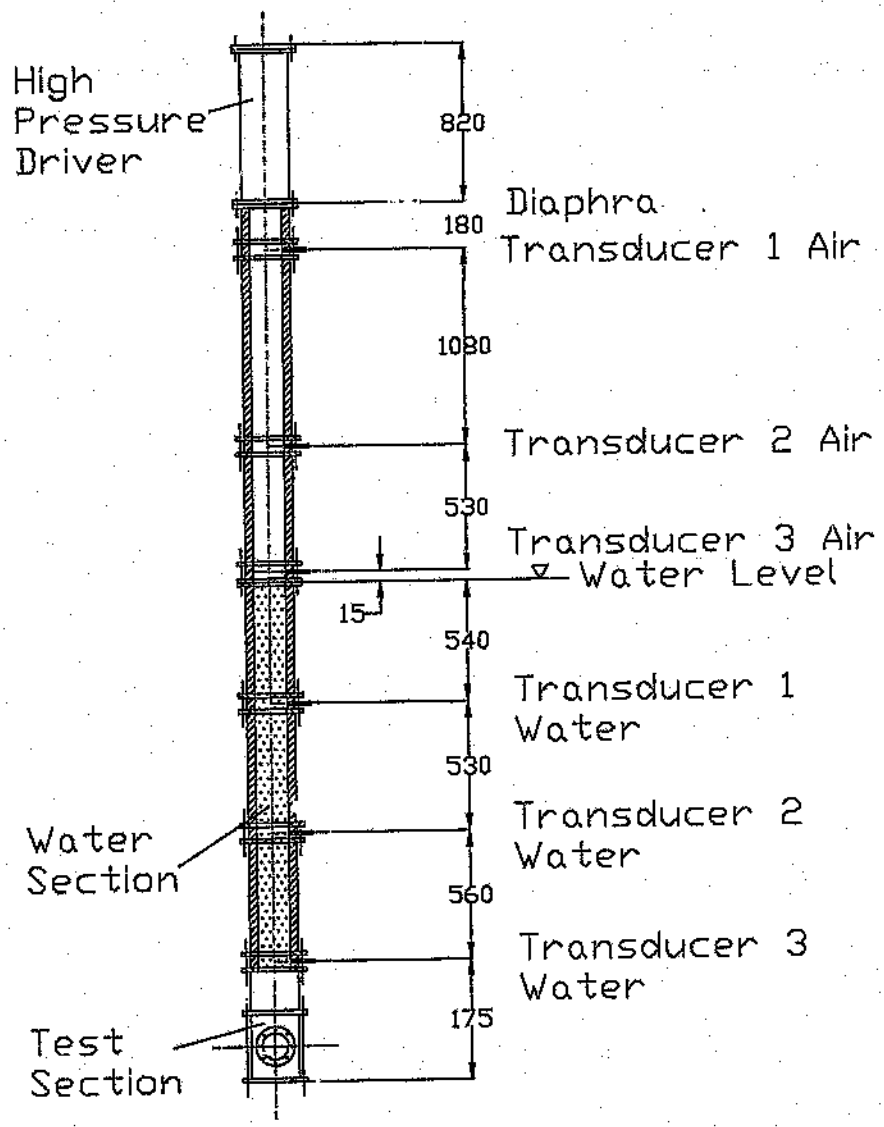

Figure 4.2: Schematic arrangement of the liquid shock tube in air mode

4.1.3 SET - UP FOR LIQUID SHOCK WAVES - PROJECTILE MODE

The experimental set-up of the shock tube for the projectile mode is shown in Fig. 4.3. The tube consists of four sections, the high pressure driver, the vacuum section which is incorporated to minimize the deceleration of the rapidly moving projectile due to the cushioning effect of any air ahead of it, the water section and the test section. Two diaphragms separate the vacuum section from the high pressure driver and the water section. The second diaphragm which covers the water surface prevents the water from boiling since the vacuum section is evacuated to a pressure of approximately 3 to 5 kPa. The projectile chamber is located immediately under the first diaphragm and has a slightly conical ring element to hold the projectile in place due to friction.

The first diaphragm is made out of polymer plastic since a maximum pressure of 50 bar in the high pressure driver is sufficient for metal forming. Therefore the needle system can be used to puncture the diaphragm. With rupturing diaphragm the projectile gets rapidly accelerated and travels with high velocity down the shock tube. At the end of the vacuum section a light gate or wire system is incorporated to determine the impact speed of the projectile. The bypassing projectile interrupts two light rays or cuts two thin current carrying wires. The time difference between these two signals is recorded in order to calculate the projectile velocity. The wire system proved to be more reliable than the light gate system which failed quite often due to atmospheric humidity inside the tube. The atmospheric humidity condensed due to the piston movement and covered the diodes.

The impacting projectile pressurises and accelerates the water which results in a liquid shock wave being generated. The liquid shock wave travels down the water section and impacts on the test specimen in the test section at the bottom of the tube. Three to four PCB pressure transducers of the A23 or M109A family are incorporated in the water section and the data gets recorded by the Yokogawa oscilloscope. The signals from the projectile velocity measurements are recorded with the computer oscilloscope.

Three different projectiles are used throughout this work. A heavy steel projectile with a mass of 3.665 kg, an aluminium projectile (0.87 kg) and a light plastic projectile made out of polyacetal (Delrin) with a mass of 0.2 kg.

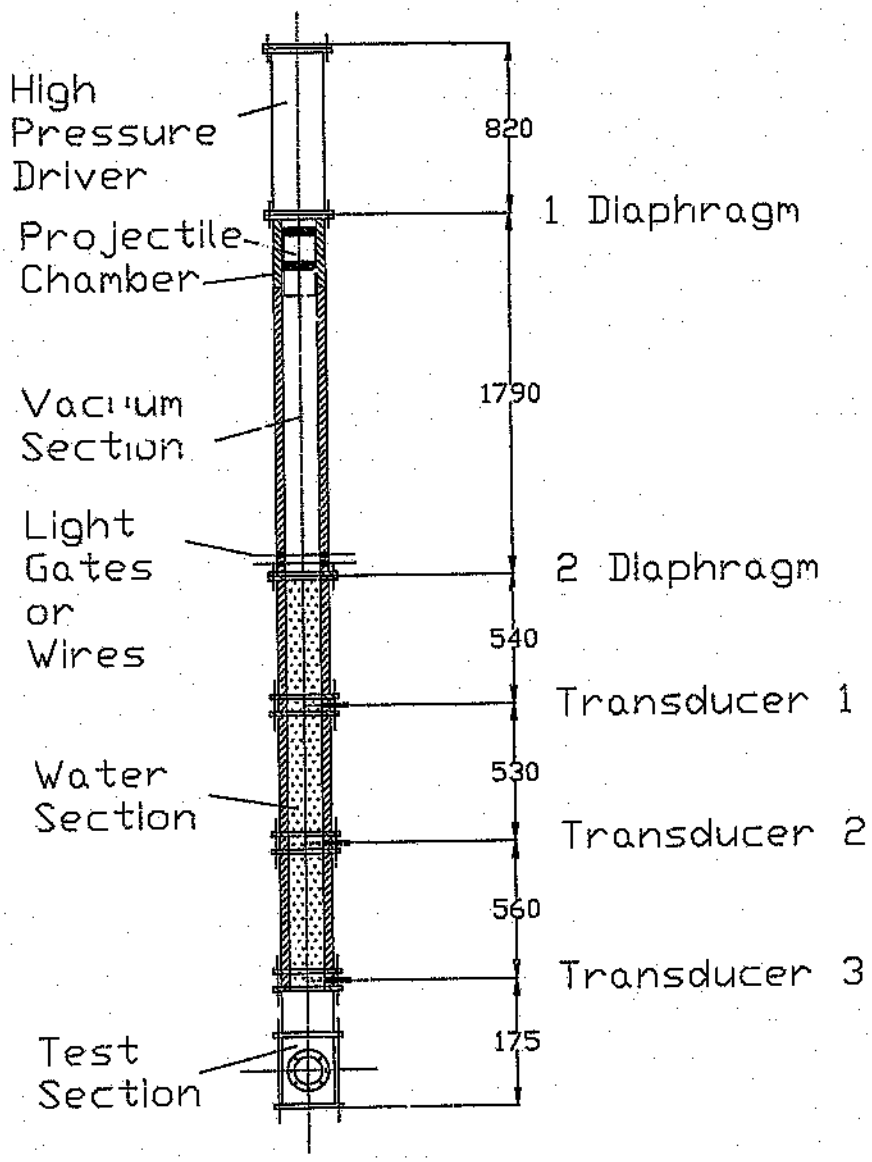

Figure 4.3: Schematic arrangement of the liquid shock tube in projectile mode

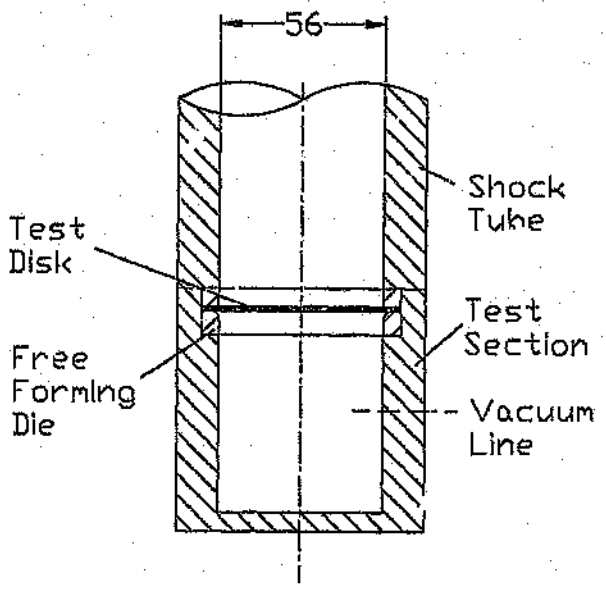

Figure 4.4: Test section for circular disks

4.2 TEST SECTIONS

The test section is situated at the bottom of the tube and allows both the testing of circular flat disks and cylindrical thin tubes. The design of the test section allows forming into dies as well as free forming.

In Fig. 4.4 a schematic drawing shows the set-up of the test section for free forming of circular disks. The test specimen is fitted to the water section by means of an adapter. An O-ring prevents water from leaking into the test section. The die is situated under the disk and the air inside the die is evacuated through the vacuum line to prevent the deforming metal from being cushioned.
The set-up of the test section for cylindrical tubes is shown in Fig. 4.5. The liquid shock wave is focused through the nozzle into the inside of the tube. The tube is fixed in the test section by means of a bottom and top tube holder. Both tube holders contain O-rings to seal the inside of the die. The die itself is split into four parts to allow a dismantling of the die after the tube has been deformed. The inside of the die is also evacuated through the vacuum line. A fourth pressure transducer ring can be incorporated between the nozzle and the test section to allow the recording of the pressure history after the liquid shock wave has been focused through the nozzle.

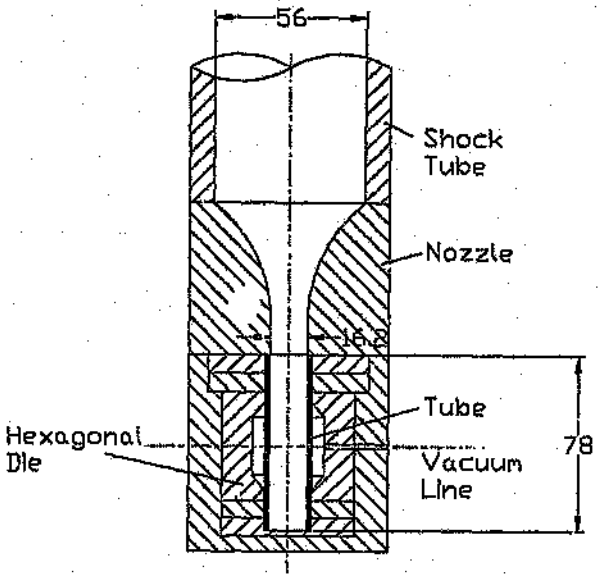

Figure 4.5: Test section for cylindrical tubes containing the hexagonal die

4.3 OPTICAL SET - UP

Two ultra-high-speed video cameras are available for the optical investigations of the deformation process. Both cameras are distributed by 'The Cooke Corporation' and are black and white CCD-Video cameras. The cameras are able to record up to 10 superimposed pictures.
The FlashCam has a resolution of 756 x 290 pixels and an exposure time of 1 μs to 1 ms which can be set in 1 μs steps. The delay time between the pictures is selectable from 0 μs to 1 ms in 1 μs steps. These settings are done by using 3-digit decade switches on the back panel of the camera. The camera has a video output and a centronics interface to readout the data to a computer.
The SensiCam is a SuperVGA black and white camera with a resolution of 1280 x 1024 pixel. The camera is controlled via the SensiControl utility software. The software allows to set the exposure time and the delay of each picture to different values. The minimum exposure and delay time is 100 ns and the maximum 1 ms.

To allow the investigation of the deformational behaviour of the test specimen during the impact of the shock wave special test sections had to be build. For the optical investigation of the deformation of cylindrical tubes a test section has been designed which is equipped with two $\emptyset$ 40 mm windows out of toughened glass. The tubes are deformed by using the free forming die. The schematic design of the optical test

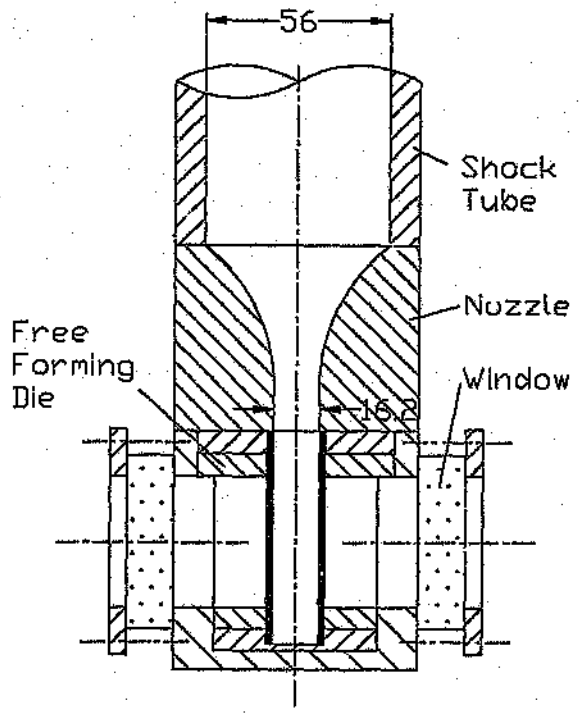

Figure 4.6: Test section for optical investigations of cylindrical tubes

section for tubes can be seen in Fig. 4.6.

The optical test section for the investigation of the deformation of flat disks is a metal box which is connected to the bottom of the shock tube by means of an adapter. Three windows out of toughened glass are incorporated in the box. The schematic set-up can be seen in Fig. 4.9. In addition special test specimens have been designed to allow a recording of the pictures from the side view. These special test specimens are not supported from the bottom and therefore the light rays are able to travel parallel and adjacent to the metal plate. Fig. 4.7 shows the design of the test specimen. In case of tearing of the test specimen the water discharges into the metal box.

For the recording of pictures in the side view a simple shadow photography system is used to illuminate the test section. The set-up of the shadow system can be seen in Fig. 4.8. Light from a 100 W halogen light source is focused onto a pin hole. From this point source parallel light, which is generated by two mirrors is used to illuminate the test section. By using a second lens the image is focused onto the

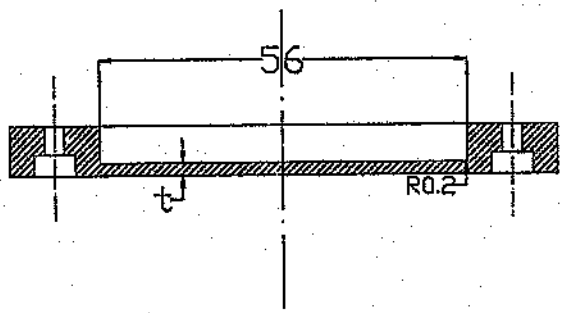

Figure 4.7: Design of test specimen to simulate flat disks

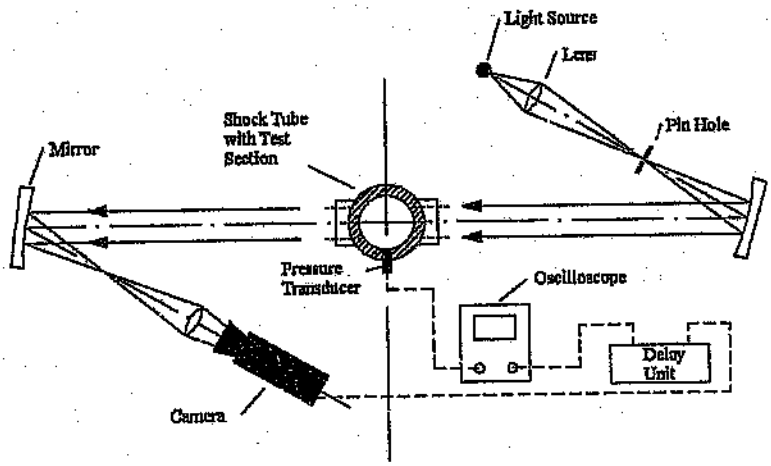

Figure 4.8: Optical set-up of the shadow system, top view

CCD chip of the camera. The camera is triggered with a trigger signal generated by the oscilloscope. The oscilloscope itself is triggered by a transducer signal from the passage of the shock wave. A delay box between the oscilloscope and the camera allows the time delay between the impacting shock wave and the first picture to be pre-set.

The third window in the bottom of the optical test section for disks gives the possibility to record the motion of the grid, which is painted onto the test specimen. A special mirror system allows the recording of the side view and the bottom view, which means the bulging of the disk and the circumferential deformation can be measured simultaneously. By using this information the strain rates for a particular

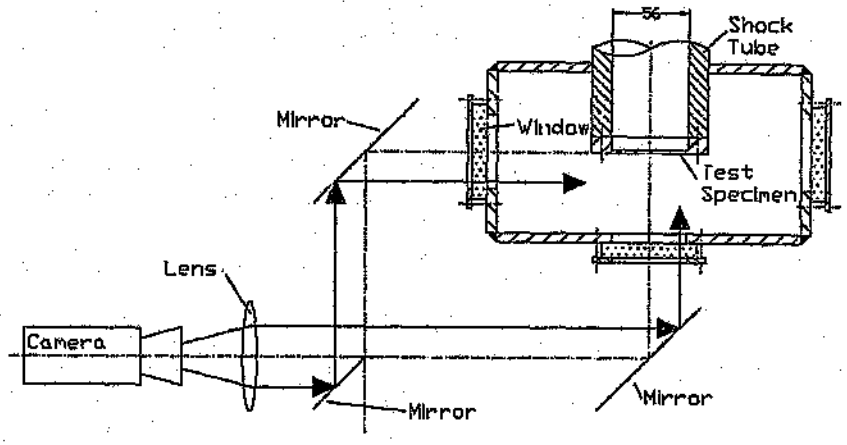

Figure 4.9: Test section for optical investigations of circular disks and set-up for strain rate measurements, side view

deformation stage can be calculated. The optical set-up for these experiments can be seen in Fig. 4.9. The camera is triggered the same way as for the shadow system set-up. The light to illuminate the test specimen is coming from the left side and from the bottom. The camera is focused onto the test specimen which is possible due to identical optical path lengths. To avoid reflections the whole test specimen is painted black. White grid lines are only applied to the right side of the specimen since this half can be seen in the bottom view.

4.4 TEST SPECIMEN

The test specimens used in this project are made out of copper and normal mild steel. The material properties of these materials have been determined in static tensile tests according to BS EN 10 002-1. Copper is ideal for high strain rate testing since the material properties do not change significantly for strain rates below $10^{-4}\ s^{-1}$ (see Chandler [29]). Above a strain rate of $10^{-4}\ s^{-1}$ the strain hardening saturates and the stress strain behaviour will approach perfect plasticity (Follansbee and Kocks [30]). Experimental results with copper under high strain rates have been conducted by Lindholm et al. [31]. Their results show little or no increase in flow stress up to strain rates of nearly $10^5\ s^{-1}$. The results are shown in Fig. 4.10.

The behaviour of mild steel is in comparison to copper strain rate sensitive. With

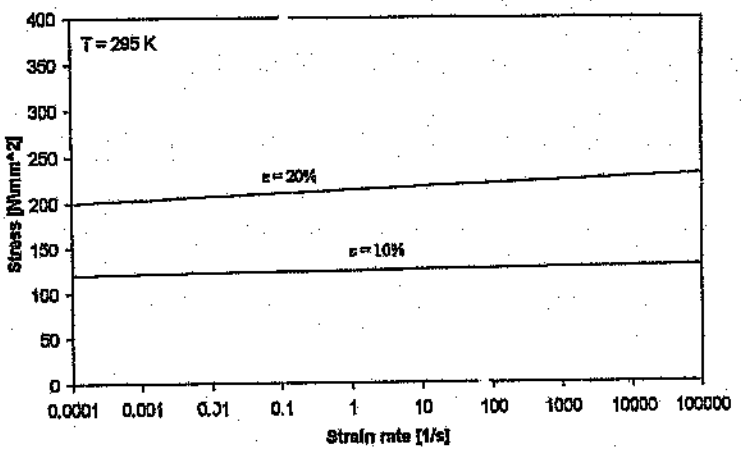

Figure 4.10: Effect of strain rate on flow stress of 99.999% copper [31]

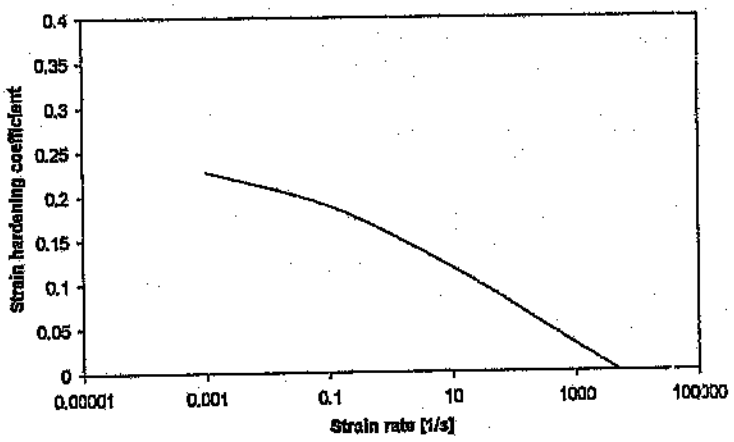

Figure 4.11: Effect of strain rate on strain hardening coefficient for mild steel [32]

increasing strain rate the flow stress increases. In addition to that the strain rate coefficient changes with increasing strain rate. Bramley and Mellor [32] have performed high strain rate tests with mild steel and their investigations show that the strain hardening coefficient of steel decreases for high strain rates and tends towards ideal plastic behaviour $n = 0$. At a strain rate of $10^3\ s^{-1}$ the strain hardening coefficient drops down to $n = 0.04$. The stress at this strain rate increases for a strain of 0.2 by 30 %. Fig. 4.11 shows the values of the strain hardening coefficient determined by Bramley and Mellor [2].

For the cylindrical disks copper C101/102 and hot rolled mild steel has been used. For copper the available thicknesses were 0.55 *mm*, 0.9 *mm* and 1.5 *mm* and for the hot rolled mild steel 0.5 *mm*, 1.0 *mm* and 1.6 *mm*. The test specimen for the optical investigations (see 4.7) have been machined out of sheet material with a thickness of 10 *mm*. For mild steel a hot rolled sheet has been used as well. The inner part of the thick plates has been skimed down on a lathe to the above mentioned thicknesses. The tolerance achieved was ± 0.05 *mm*.

For the cylindrical tubes copper C106 and mild steel have been used. The outside diameter for all tubes was 19.05 *mm*. For the copper tubes a wall thickness of 1.1 *mm*, 1.4 *mm* and 1.6 *mm* was available. The mild steel tubes were supplied with wall thicknesses of 1.24 *mm* and 1.63 *mm*.

5 OPERATING CYCLE OF THE LIQUID SHOCK TUBE IN THE AIR MODE

The air shock wave in the driven section is generated by the bursting of the diaphragm that separates the two sections. The pressure of the air shock wave can be calculated by iterating the following equation given by Glass and Sislian [2].

$$p_{41} = p_{21} \left[1 - \frac{(\gamma_4 - 1)\frac{a_1}{a_4}(p_{21} - 1)}{\sqrt{2\gamma_1(\gamma_1 + 1)\left(p_{21} + \frac{\gamma_1 - 1}{\gamma_1 + 1}\right)}} \right]^{-2\gamma_4/(\gamma_4 - 1)} \tag{5.1}$$

In this equation subscript 4 stands for the conditions in the driving section and subscript 2 for the conditions behind the air shock wave. Subscript 1 describes the condition in the driven section in front of the shock wave (the ambient pressure due to the high altitude of Johannesburg is about 0.83 *bar*). p_{ij} stands for p_i/p_j. For air or nitrogen γ is 1.4.

An air shock wave is characterised by a pressure jump Δp over a very short time. Behind the pressure jump the pressure stays constant ($p_2 = const$) for a certain time (depending on the size of the driving section). This pressure history of the air shock wave determines the pressure profile of the liquid shock wave. With the impact of the air shock wave the liquid shock wave is generated. Due to the constant pressure behind the reflected air shock wave, the interface remains pressurised and the pressure behind the liquid shock wave stays constant as well.

The pressure of the liquid shock wave generated by an air shock wave can be calculated using equation 5.2. The impacting air shock wave gets reflected on the water surface with the pressure p_6. The pressure on the contact surface between the air and the water is equal and therefore the same pressure p_5 is transmitted into the water. Since the density and th . wave speed in water are much higher than in air the reflection is similar to a reflection from a solid wall.

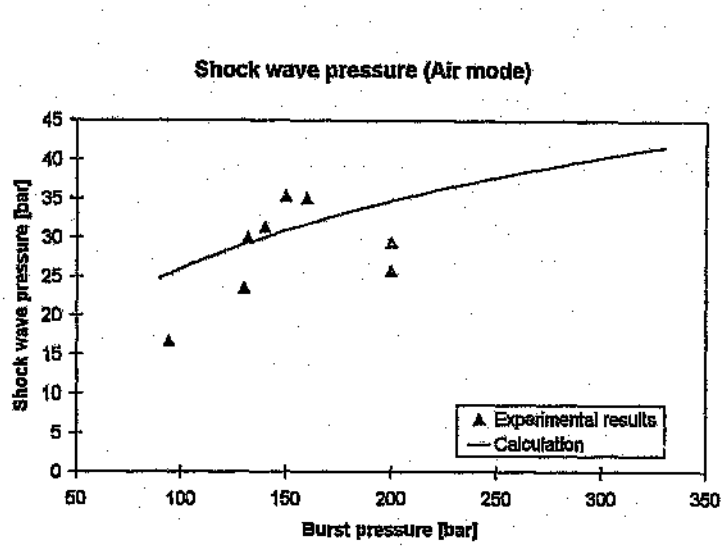

Figure 5.1: Liquid shock wave pressure versus burst pressure in driving section

$$p_{51} = p_{21} \frac{1 - \gamma + p_{21}(3\gamma - 1)}{1 + \gamma + p_{21}(\gamma - 1)} \tag{5.2}$$

The results of the calculations of the pressure of the liquid shock wave in comparison to experimental measurements are shown in Fig. 5.1. The comparison shows that the experimental results are in reasonable agreement with the theoretical curve. This variability is due to the metal diaphragms opening slowly. The opening time has a great influence on the shock wave strength. In addition to that the driven air section in the experimental set-up is very short (32 pipe diameters). This means the air shock wave is not fully established when it impacts on the water surface. A shock wave which is not fully established is characterised by a pressure rise behind the initial shock wave. Thus it is difficult to accurately control the strength of the air shock wave and with that the strength of the liquid shock wave.

A typical pressure history for a liquid shock wave generated with an air shock wave can be seen in Fig. 5.2. The pressure traces of the three transducers show the liquid shock wave travelling down the shock tube. A substantial pressure rise behind the initial shock wave front and an increasing strength of the initial shock wave can be seen in the pressure history. This is an indication for the air shock wave which impacted on the water surface not being fully established.
At the third transducer near the bottom wall the pressure reaches nearly double the pressure of the initial shock wave due to the reflection at the end wall. The reflected

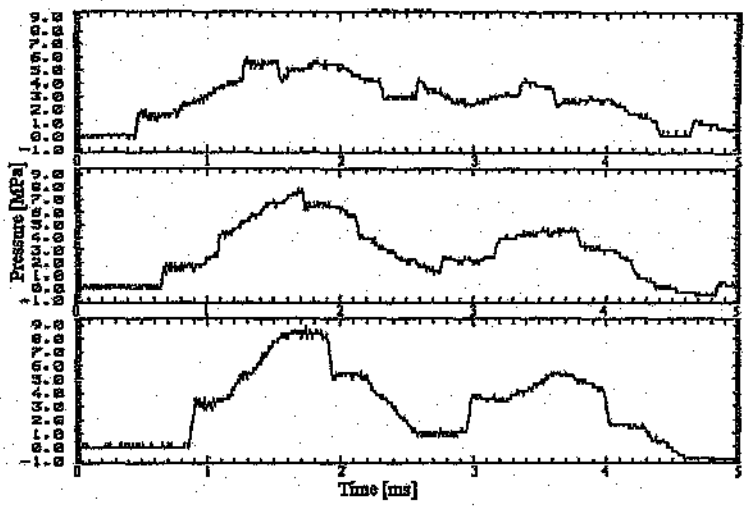

Figure 5.2: Pressure history for a liquid shock wave, generated with an air shock wave. Transducer 1, 2, and 3

shock wave travels up the shock tube and superimposes with the initial wave. At the water surface the reflected liquid shock wave reflects as an expansion wave due to the density difference between water and air. This expansion wave which is travelling down the shock tube, can be seen as a pressure drop in Fig. 5.2.

6 OPERATING CYCLE AND ENERGY TRANSFER OF THE LIQUID SHOCK TUBE IN PROJECTILE MODE

In this section the operating cycle of metal forming in a liquid shock tube in the projectile mode is discussed with respect to the energy transfer. Several theoretical models are presented to predict the whole energy transformation process in the liquid shock tube. The energy transformation process consists of:

1. the potential energy stored in the compressed gas is converted into kinetic energy of the projectile
2. the kinetic energy of the projectile is converted into pressure energy in the liquid after the impact
3. the pressure energy of the liquid shock wave is transformed into deformation energy of the workpiece

The results of the theoretical models are presented and compared to experimental results.

6.1 KINETIC ENERGY OF THE PROJECTILE

6.1.1 THEORETICAL CALCULATION AND EXPERIMENTAL RESULTS OF PROJECTILE IMPACT VELOCITY

For the 'High Speed Metal Forming with Liquid Shock Waves' the total energy available is of prime importance. Potential energy of the compressed gas in the driving section of the shock tube is converted into kinetic energy of the moving

projectile. To avoid a significant deceleration of the projectile during its movement through the shock tube, the driven section is evacuated to a pressure of about 40 *mbar*. The projectile velocity and with it the kinetic energy available can be ascertained by using the following equation given by Heiser [33], where L is the length of the driven section, Δp_{41} the pressure difference between driver and driven section, A_P the area, V_P the maximum achievable velocity and m_P the mass of the projectile. The length of the high pressure driver is of no importance for this calculation since the driver in the experimental set-up is long enough to avoid an influence of the expansion wave.

$$\frac{LA_P(1-\gamma)}{2a_4^2 m_P}\Delta p_{41} = \left(1-\frac{\gamma-1}{2a_4}V_P\right)^{\frac{2}{\gamma-1}} - \frac{2}{1+\gamma}\left[\left(1-\frac{\gamma-1}{2a_4}V_P\right)^{\frac{1+\gamma}{\gamma-1}} - 1\right] - 1 \tag{6.1}$$

Müller [6] reported in his work that the experimental results were nearly 75% of the calculated values. The results of the experiments performed within this project show a difference of about 40% from the calculated values. The difference in the projectile velocity of the current experiments to Müller's results is due to a small difference in the design of the shock tube. During the movement of the projectile, the remaining air in the driven section is compressed. In Müllers shock tube the cross sectional area of the diaphragm section, that covers the water surface, is larger than the cross sectional area of the projectile and therefore the remaining air in the driven section is not significantly pressurised. In the present case the cross sectional area of the shock tube is constant and the remaining air gets pressurised and decelerates the projectile. The results of this calculation in comparison to experimental results of tests performed with the steel projectile can be seen in Fig. 6.1.

To achieve a better accordance to theoretical calculations with experimental results the projectile-energy is numerically integrated from the following equation [34]:

$$E = \int p_4 A dx \tag{6.2}$$

If it is assumed that air is an ideal gas the pressure can be determined from the equation of state for ideal gases:

$$p = \frac{mRT_2}{V_2} \tag{6.3}$$

By using the simplifying assumptions of an adiabatic and isentropic change of state ($n = \gamma$) the temperature can be calculated:

$$T_2 = T_1\left(\frac{V_1}{V_2}\right)^{(\gamma-1)} \tag{6.4}$$

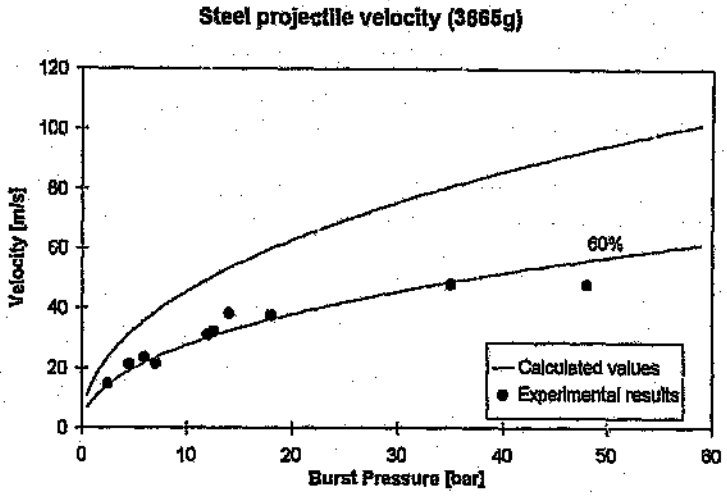

Figure 6.1: Comparison of experimental projectile velocities and calculated values by using eqn. 6.1

The net kinetic energy of the projectile consists of the energy imparted from the expansion of the compressed air in the driving section and the energy-losses due to the compression of the remaining air in the driven section through the projectile movement. For the compression of the remaining air it is assumed that there is no blow-by past the projectile.

$$E_P = E_1 - E_2 \tag{6.5}$$

The projectile velocity is calculated from the net kinetic energy at the moment of impact on the water surface:

$$V = \sqrt{\left(2\, E_{kin}\, \frac{1}{m_p}\right)} \tag{6.6}$$

The results of the above calculations can be seen in Fig. 6.2 to Fig. 6.4. The diagrams show the projectile velocity versus burst pressure for the steel projectile ($3.665kg$), for the aluminium projectile ($0.87kg$) and for the light plastic projectile ($0.2kg$).

The comparison of the experimental data with the calculated curves shows a good agreement. It can be seen that the experimental values are slightly lower than the calculated ones. This is due to the neglecting of friction.
The opening time of the diaphragm also has an important influence on the piston velocity as already mentioned in section 4.1.3. In case of a slow opening diaphragm the

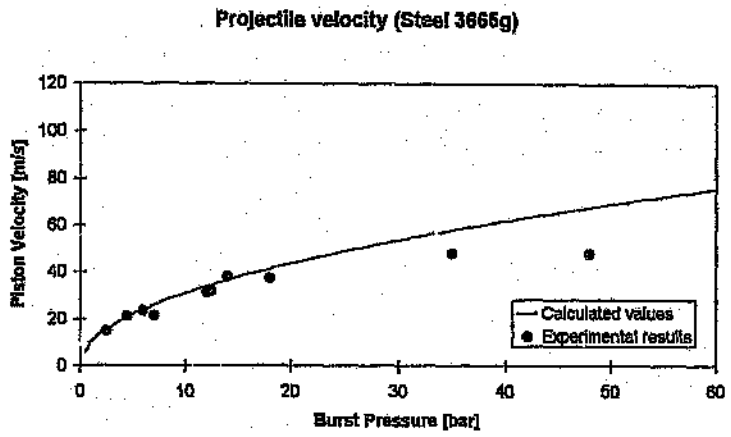

Figure 6.2: Comparison of calculated and experimental values for steel projectile (3.665 *kg*) velocity

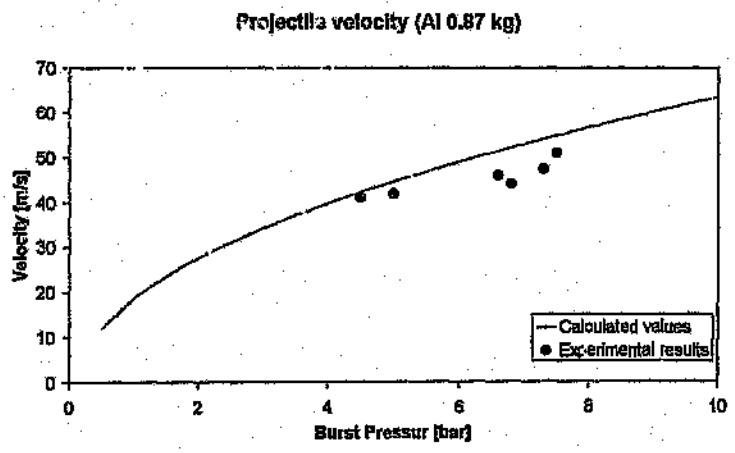

Figure 6.3: Comparison of calculated and experimental values for aluminium projectile (0.87 *kg*) velocity

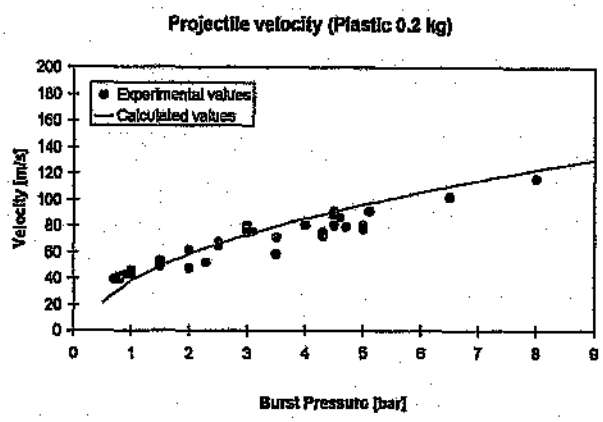

Figur 6.4: Comparison of calculated and experimental values for plastic projectile (0.2 kg) velocity

projectile velocity is much slower than expected. For repeatable tests the diaphragm has to be chosen as thin as possible.

6.2 PRESSURE ENERGY OF THE LIQUID SHOCK WAVE

6.2.1 THEORETICAL CALCULATIONS AND EXPERIMENTAL RESULTS

To predict the pressure history of the liquid shock wave, the process of the projectile, impacting on the water surface has to be considered. With the calculated profile of the shock wave the maximum pressure, the energy and the impulse of the shock wave can be estimated. For this calculation Müller [6] suggests the use of the method of characteristics. The Riemann Invariant is defined in [2] and [35] as follows:

$$P = \frac{2}{n-1}a + V \tag{6.7}$$

$$Q = \frac{2}{n-1}a - V \tag{6.8}$$

where P is the characteristic for a positive wave (right going) and Q for a negative wave (left going). The slope of the characteristics are:

$$\frac{dx}{dt} = V \pm a$$

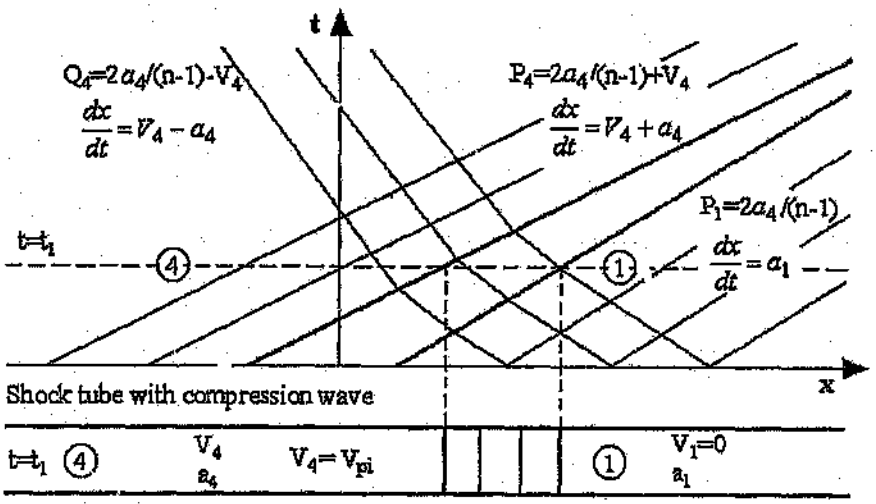

Figure 6.5: x-t wave diagram with expansion and compression characteristics of a compressed fluid in a shock tube

where a is the local speed of sound. For an isentropic and adiabatic flow P and Q are constant along a characteristic. Fig. 6.5 shows the behaviour of the P and Q characteristics in an x-t diagram under the influence of a compression wave. The compression wave increases the temperature in the fluid. The higher temperature results in a higher speed of sound and a higher particle velocity. A smaller slope of the characteristics means a higher velocity of the waves and makes the characteristics converging. Later on, the P characteristics will come together and form a shock wave. A similar wave diagram will be generated when the fluid is compressed by a rapidly moving projectile. For a projectile, moving with a constant velocity, the compression wave becomes a plane shock wave, centred in the origin of the x-t diagram and running ahead of the projectile.

As mentioned above, P is constant along the characteristic. Due to the increasing speed of sound and increasing particle velocity the value for Q stays constant over the complete compression process. By using Eqs. 6.7 and 6.8 this leads to:

$$Q = \frac{2}{n-1}a_i - V_{Pi} = \frac{2}{n-1}a_1$$

$$a_i = a_1 + \frac{n-1}{2}V_{Pi} \tag{6.9}$$

Before the impact of the projectile, the liquid is at rest. For water, that means, the speed of sound is $a_1 = 1483\ m/s$ and the particle velocity is zero. Just after

the impact the particles are accelerated and it can be assumed that for a short time interval the velocity of the projectile stays constant V_{Pi}. Therefore the fluid particles ahead of the projectile have the same velocity V_P as the projectile. Using Eq. 6.9 the new speed of sound can be calculated. A modification of Eq. 2.19 leads to an equation for the pressure p_{Pi} in front of the projectile. In this equation a_1 stands for the speed of sound in the water compressed by the projectile:

$$p_{Pi} = B\left(\left(\frac{\rho_1 a_1^2}{nB}\right)^{\frac{n}{n-1}} - 1\right) \tag{6.10}$$

This equation neglects the material properties of the projectile. Therefore a reflection factor R has to be introduced, which depends on the acoustic impedance of the projectile material.

$$p_i = p_{Pi} R \tag{6.11}$$

For the steel projectile the reflection factor is $R \approx 1.0$, for the aluminium projectile $R \approx 0.85$ and for the plastic projectile $R \approx 0.35$ (see [6]). The shape of the shock wave pressure profile can now be calculated step wise. The force decelerates the projectile in the time interval Δt down to the new velocity V_{Pi+1}. With the conservation of momentum the new velocity can be written:

$$(V_{Pi+1} - V_{Pi})\, m_p = -p_i A \Delta t$$

$$V_{Pi+1} = V_{Pi} - \frac{p_i A \Delta t}{m_p} \tag{6.12}$$

To determine the velocity of the shock wave V_s, the change of the particle velocity over the shock wave has to be considered (see [35]).

$$\frac{u_2}{u_1} = \frac{2 + (n-1)M^2}{(n+1)M^2}$$

For a system of co-ordinates that is travelling with the shock wave, the particle velocities can be expressed with $u_1 = V_s$ and $u_2 = V_s - V_P$. That leads to the following equation for the shock wave velocity:

$$V_{Si} = \frac{n+1}{4} V_{Pi} + \sqrt{\left(\frac{n+1}{4} V_{Pi}\right)^2 + a_1^2} \tag{6.13}$$

From equation 6.10 it can be seen that the maximum pressure of the liquid shock wave depends only on the impact velocity of the projectile and the projectile material

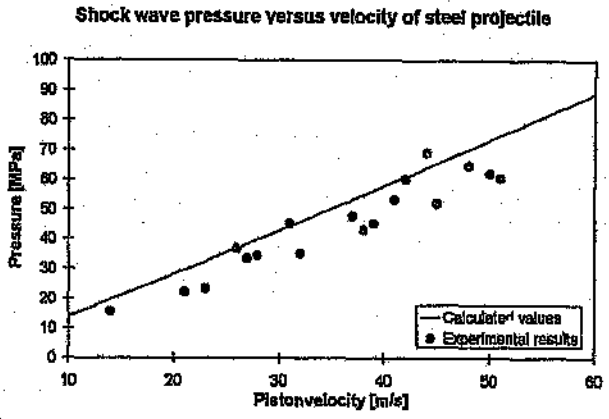

Figure 6.6: Comparison of calcuated maximum shock wave pressure and experimental results performed with a steel projectile (3.665 kg)

(different acoustic impedance). Equation 6.12 shows that the profile and with it the energy and impulse of the shock wave depends not only on the impact velocity, but also on the inertia of the projectile. That means that the negative slope of the shock wave after the maximum pressure peak is much higher for a lighter projectile than for a heavier projectile, due to the faster deceleration of the lighter projectile. Results of the above mentioned calculations and comparisons with experiments are shown in Fig. 6.6 to Fig. 6.15.

In Fig. 6.6 the maximum shock wave pressure versus the impact velocity of the steel projectile can be seen. For the calculation, equation 6.10 was used. The experimental values were measured with the first pressure transducer in the water column. Fig. 6.7 shows as an example a calculation of the shock wave pressure profile in comparison to an experimental shock wave. The impact velocity was 42.9 m/s. The steel projectile with a mass of 3.665 kg was used. The curves are very similar and the above calculation yields a good approximation. The second pressure peak of the experimental curve in Fig. 6.7 is the reflected shock wave, coming from the bottom of the shock tube. The third pressure peak is due to a second reflection of the shock wave from the steel projectile which is lying on the water surface. For a velocity of 42.9 m/s the kinetic energy of the steel projectile is 3372.5 J and the momentum is 157.2 Ns. For the simulated shock wave the energy is 3249.8 J. The experimental shock wave yields an energy of 3136.3 J and an impulse of 130 Ns.

The following figures (Fig. 6.8 and Fig. 6.9) show the behaviour of the projectile during the impact. The calculations were made at the same conditions as mentioned

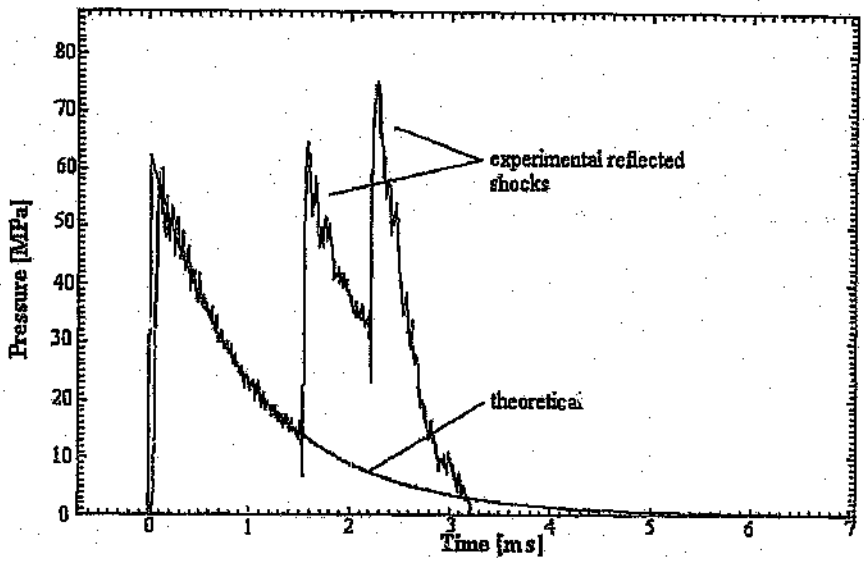

Figure 6.7: Comparison of calculated shock wave pressure and experimentally measured shock wave pressure for the 3.665 *kg* steel projectile

above. In Fig. 6.8 the deceleration of the steel projectile versus time can be seen. The projectile velocity has dropped from 42.9 m/s to zero within 6 ms . That means the maximum duration of the shock wave is also 6 ms, which can be seen in Fig. 6.7. The distance that the projectile travels during the impact is shown in Fig. 6.9. The maximum displacement and with that the compression of the water column after 6 ms is approximately 43 mm.

The following figures (Fig. 6.10 - Fig. 6.13) show the results of the calculations and experiments performed with the light plastic projectile (0.2 kg). For the plastic projectile the reflection factor is only $R \approx 35\%$ due to the smaller density of the material. The small reflection factor leads to a lower pressure in the water column. Therefore the curve of maximum pressure in Fig. 6.10 has a smaller slope in comparison to the curve for the steel projectile.

In Fig. 6.11 a comparison is made between the calculated shock wave profile and a measured one. The impact velocity of the projectile was 91 m/s. The comparison shows that the slope of the experimental shock wave is a little bit steeper than the calculated one due to a deformation of the projectile, but the calculation yields a good approximation. The impacting projectile has a kinetic energy of 783.4 J and a momentum of 17.22 Ns. The integration of the energy over the calculated shock

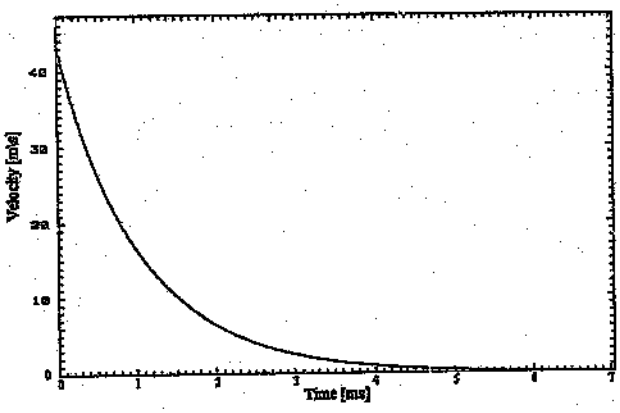

Figure 6.8: Calculated results of steel projectile (3.665 kg) deceleration for an impact velocity of 42.9 m/s

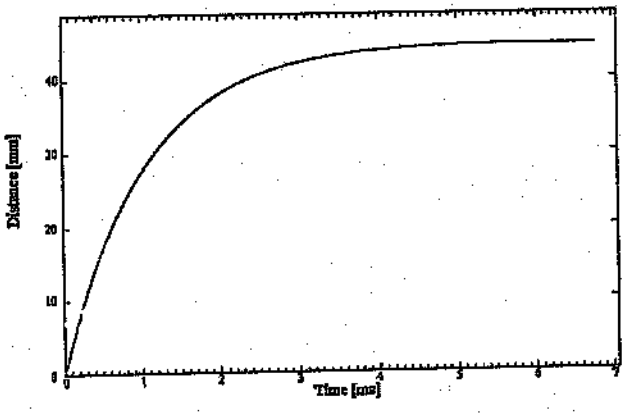

Figure 6.9: Calculated results of steel projectile (3.66[illegible] kg) displacement for an impact velocity o[illegible] 2.9 m/s

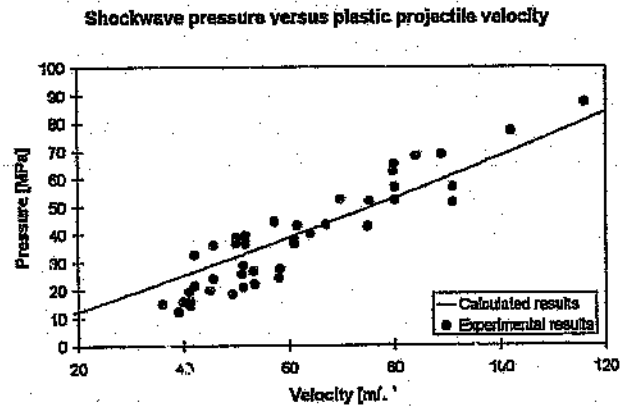

Figure 6.10: Comparison of calculated maximum shock wave pressure and experimental results performed with a plastic projectile (0.2 kg)

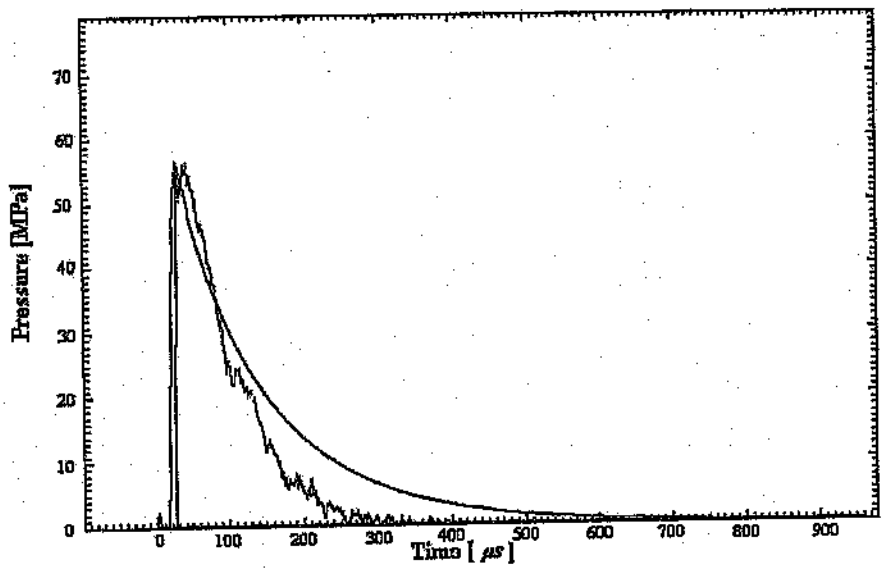

Figure 6.11: Comparison of the calculated shock wave pressure and the measured one for the (0.2 kg) plastic projectile

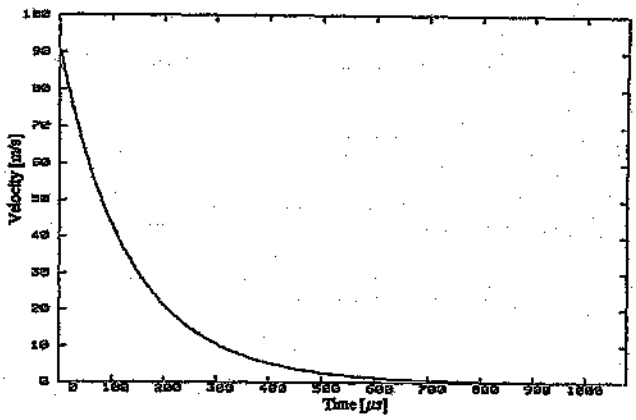

Figure 6.12: Calculated results of plastic projectile (0.2 kg) deceleration for an impact velocity of 91 m/s

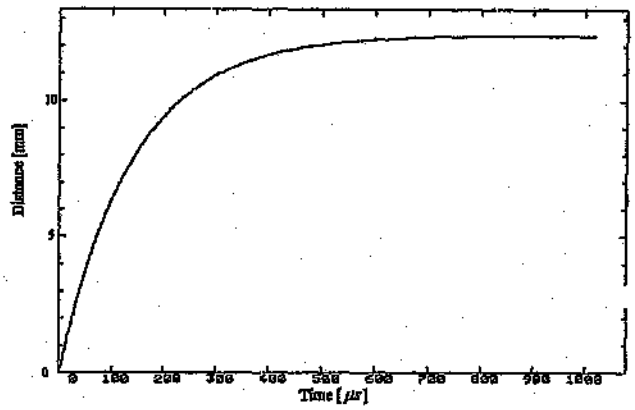

Figure 6.13: Calculated results of plastic projectile (0.2 kg) displacement for an impact velocity of 91 m/s

wave profile results in an energy of 301.1 J. This energy difference is due to the small reflection factor of the plastic projectile. In the experiment the shock wave yields an energy of 319.09 J and an impulse of 13.4 Ns. The inertia of the plastic projectile is much smaller than that of the steel projectile. The velocity of the plastic projectile drops from 91 m/s to zero (see Fig. 6.12) within 700 μs, which is the reason for the much smaller duration of the shock wave. The maximum displacement of the projectile after impact is smaller than for the heavier steel projectile as well. The displacement versus time curve can be seen in Fig. 6.13.

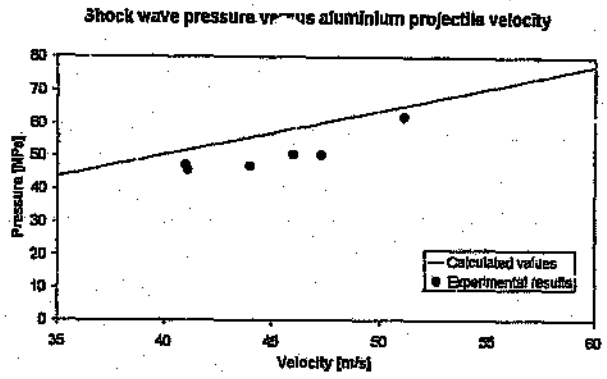

Figure 6.14: Comparison of the calculated shock wave pressure and the measured one for the (0.87 kg) aluminium projectile

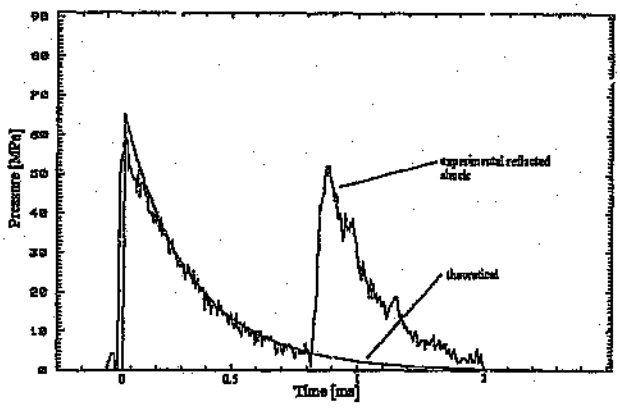

Figure 6.15: Comparison of calculated shock wave and experimentally measured shock wave for the aluminium projectile (0.87 kg)

The results for the aluminium piston can be seen in Fig. 6.14 and Fig. 6.15. A comparison between the maximum liquid shock wave pressures for the experiment and for the calculation is shown in Fig. 6.14. Fig. 6.15 shows a comparison between the profile of an experimental shock wave and the calculated curve. The impact velocity was 51.1 m/s. It can be seen that the calculated shock wave for the aluminium piston is also in good agreement with the experimental curve. The second pressure peak of the experimental curve in Fig. 6.15 is the reflected shock wave, coming from the bottom of the shock tube. The energy and the impulse of the calculated shock wave are 961 J and 44.37 Ns respectively. In the experiment the projectile generated a shock wave with an energy of 874.4 J and a momentum of 42.9 Ns.

6 3 DEFORMATION ENERGY OF THE WORKPIECE

Of great interest for high speed forming of metals is the energy absorbed by the metal during the deformation process. In [12] the deformation energy per unit volume is given by:

$$W_V = \int_0^{\bar{\epsilon}} \sigma d\epsilon$$

To calculate the energy for a given material the true stress has to be expressed in terms of the true strain. The flow - stress power law for the plastic region gives:

$$\sigma = K\epsilon^n \tag{6.14}$$

$$W_V = K \int_0^{\bar{\epsilon}} \epsilon^n d\epsilon$$

Integration of the equation leads to:

$$W_V = \frac{K}{n+1} (\bar{\epsilon})^{n+1}$$

The material constant n is defined as the strain-hardening exponent and K is the strength coefficient. For copper both constants can be derived from the true-stress true-strain diagram determined from tensile tests using the given material. This is a permissible approximation since the change in the stress strain behaviour for copper is small (see section 4.4). The constants can be obtained by plotting equation 6.14 in a log-log graph, which will yield a straight line with a slope of n:

$$ln\,\sigma = n\,ln\,\epsilon + ln\,K$$

The material constant K can be seen to be the true stress associated with a true strain of 100 %.

The stress strain behaviour for mild steel changes with increasing strain rates and therefore the material constants cannot be taken from static tensile tests. For the calculation the material constants determined in the high strain tests from Bramley and Mellor [32] have been used (see section 4.4).

In order to compute the total deformation energy it is necessary to determine the volume of the metal being deformed. This is done by measuring the deformation of the test specimen. The results of the calculation of the deformation energy for circular plates and cylindrical tubes are shown in section 8.1.1 and 9.2.1 respectively.

7 THE EFFECT OF THE PROJECTILE GEOMETRY, MASS AND MATERIAL ON THE PRESSURE HISTORY OF THE LIQUID SHOCK WAVE

This section deals with the investigation of the generation of liquid shock waves by using different projectiles. Experimental results for different projectile masses and materials are presented with respect to maximum pressure, energy and impulse of the liquid shock wave. Double and triple liquid pressure pulses are generated by using stepped projectile impact surfaces. The results of these experiments are discussed with respect to the contour of the liquid shock waves. A finite element program is employed to simulate the generation and the propagation of the liquid shock wave numerically. Different projectile masses, materials and geometries are considered in these calculations.

7.1 EXPERIMENTAL RESULTS WITH DIFFERENT PROJECTILE MASSES AND MATERIALS

Since the maximum pressure, the energy, and the impulse of the liquid shock waves play an important role for metal forming, the experimental results of tests performed with the three different projectiles are presented in the following three figures (Fig. 7.1 - 7.3). The results have been obtained from the measured pressure traces. The shock wave energy and the shock wave impulse have been calculated by using equation 2.9 and 2.10. In Fig. 7.1 the maximum pressure of the liquid shock waves is shown. It can be seen that the plastic projectile yields the curve with the steepest slope despite having the lowest reflection factor. This is due to the much higher impact velocities of this projectile in comparison to the impact velocities of the heavier aluminium and steel projectile. Equation 6.11 shows that the maximum pressure

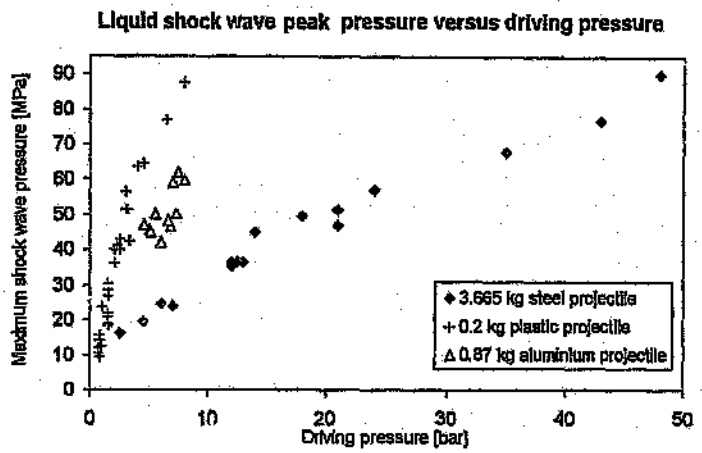

Figure 7.1: Maximum shock wave pressure versus pressure in driving section

of the liquid shock wave only depends on the projectile velocity and material. The heavy steel projectile produces the curve with the lowest slope.

In Fig. 7.2 a comparison of the shock wave energies generated with the steel, the aluminium and the plastic projectile can be seen. The shock wave energy generated with the steel projectile is slightly smaller than the values for the plastic and aluminium projectile. This is most probably due to higher friction losses when using the steel projectile. The steel projectile is longer in comparison to the plastic and aluminium projectile and for very slow projectile velocities the friction losses become more important.

A comparison of the generated shock wave impulse is made in Fig. 7.3. The shock wave impulse generated by the steel projectile is larger than that for the aluminium and plastic projectile. In the equation for the momentum, the mass of the projectile plays a much more important role than in the equation for the energy, where the mass is compensated for by the velocity, which is squared. The plastic projectile due to its low mass yields the curve with the lowest slope.

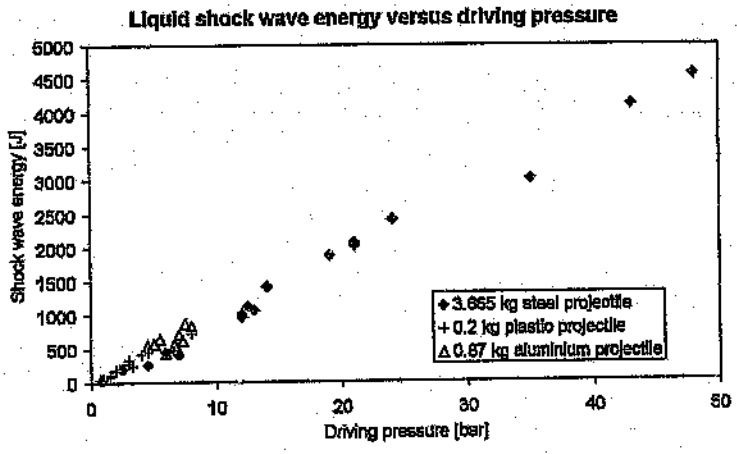

Figure 7.2: Shock wave energy versus pressure in driving section

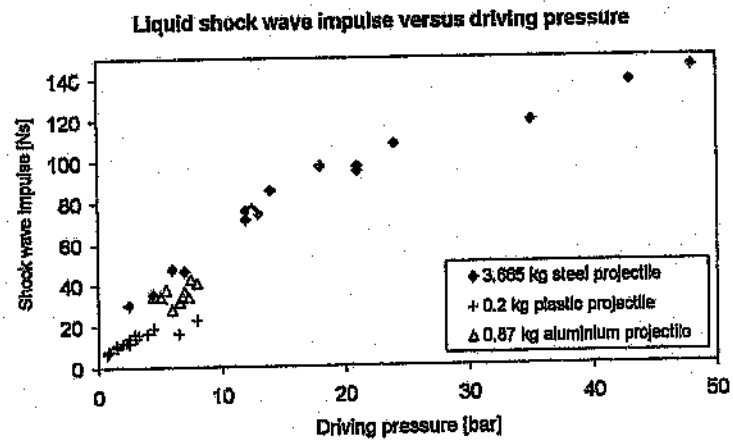

Figure 7.3: Shock wave impulse versus pressure in driving section

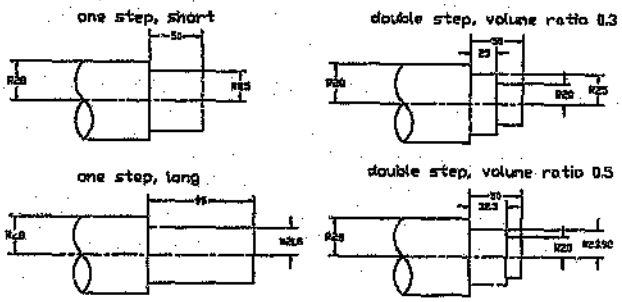

Figure 7.4: Projectile dimensions for single and double stepped projectiles

7.2 EXPERIMENTAL RESULTS WITH DIFFERENT PROJECTILE GEOMETRIES

As described in section 6.2 a projectile with a plane surface generates a single or normal liquid shock wave which is similar to a blast wave. The use of a stepped projectile surface permits the generation of a double or triple liquid shock wave. These types of shock waves are important for metal forming because it allows splitting of the deformation process into two or three stages.

The dimensions of the stepped projectile surfaces are shown in Fig. 7.4. Four different stepped projectiles are available. Two single stepped projectiles with a step of 50 mm and 95 mm and two double stepped projectiles. The first double stepped projectile has symmetrical steps of 25 mm length. The volume ratio of the void part of the second step in comparison to the whole void volume is ~ 0.3. For the second stepped projectile the length of the steps is irregular. The first step has a length of 17.7mm and the second 32.2 mm. Therefore the volume ratio is ~ 0.5.

As an example five wave diagrams are shown in Fig. 7.5 to 7.9 for a plane, the two single stepped, and the two double stepped projectiles respectively. The pressure traces have been recorded with three pressure transducers in the water section.

The wave diagram in Fig. 7.5 shows the behaviour of a normal liquid shock wave. With a speed of 1550 m/s the shock wave travels down the shock tube and gets reflected at the bottom. That leads to a pressure at transducer 3 which is nearly double the initial shock wave pressure. The reflected shock wave travels up the shock tube and gets reflected again by the steel projectile lying on the water surface.

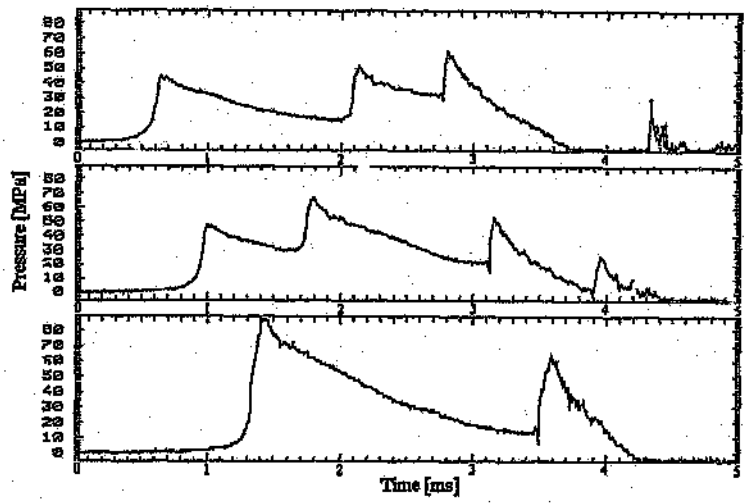

Figure 7.5: Steel projectile (3.665 kg), plane surface, impact velocity 39.6 m/s, Transducer 1, 2 and 3

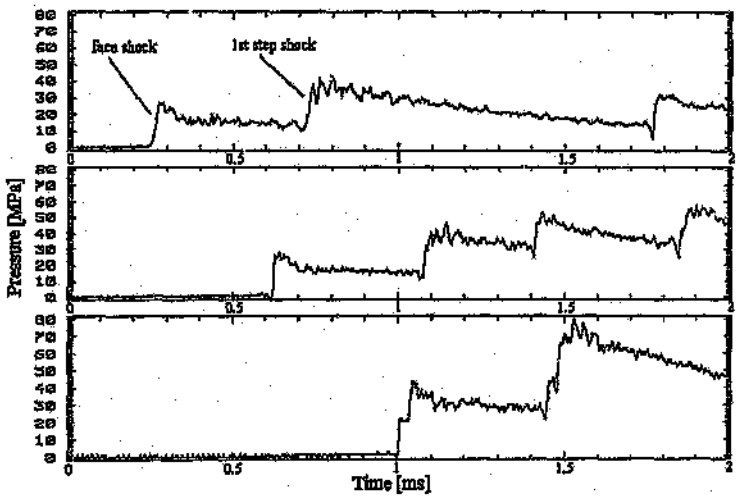

Figure 7.6: Steel projectile (3.198 kg), short step, impact velocity 37.5 m/s, Transducer 1, 2 and 3

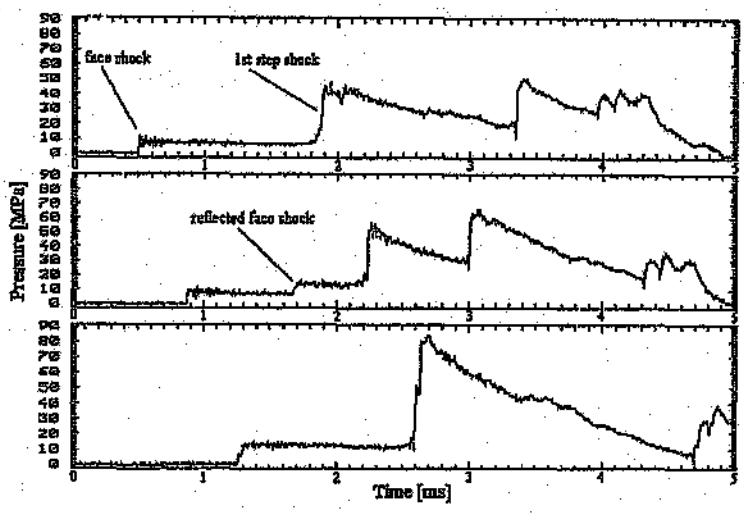

Figure 7.7: Steel projectile (3.85 kg), long step, impact velocity 37.5 m/s, Transducer 1, 2 and 3

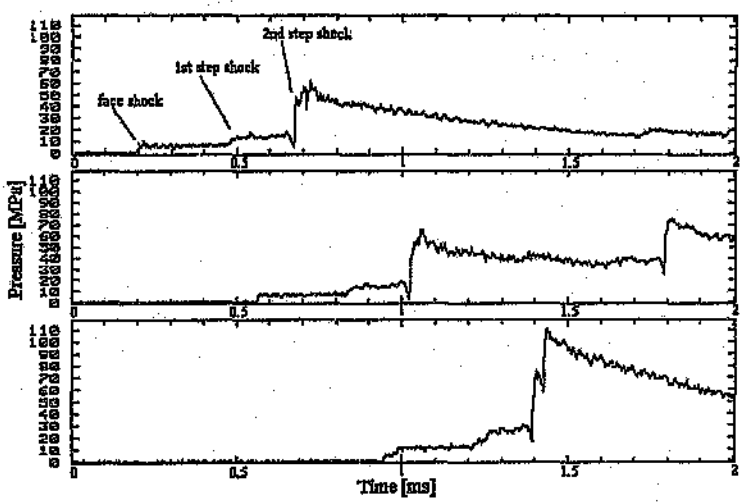

Figure 7.8: Steel projectile (3.054 kg), double step, volume ratio $\sim$ 0.3, impact velocity 39.0 m/s, Transducer 1, 2 and 3

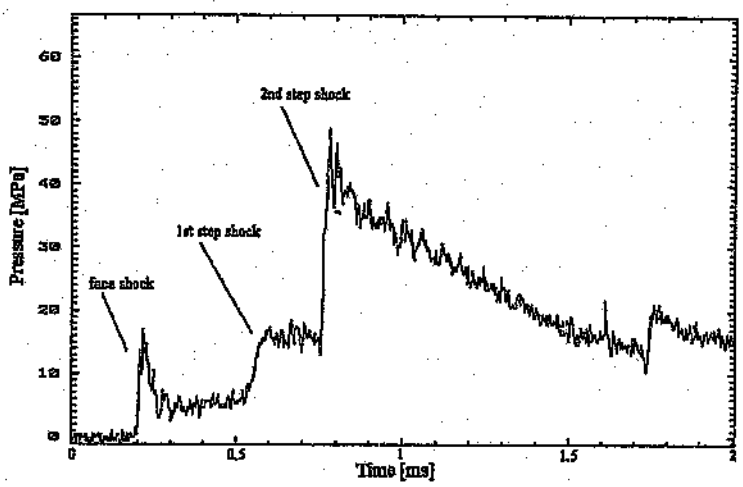

Figure 7.9: Steel projectile (3.054 kg), double step, volume ratio $\sim$ 0.5, impact velocity 39.0 m/s, Transducer 1

Figure 7.6 shows the wave diagram for a double shock wave produced by the projectile with the short step. The first pressure peak (the face shock) is generated by the top of the projectile impacting on the water surface and the second peak (1st step shock) by the step. An interesting phenomenon is the nearly constant pressure between the first and the second pressure peak. That implies that the velocity of the water particles stays constant in contrast to a decelerating projectile. This occurs as liquid flows from the front of the projectile to fill the radial gap resulting from the step. After the step has hit the water surface, the clearance gap between the shock tube wall and the projectile is completely filled with water and now the water particles in front of the projectile have the same velocity as the projectile.

In Fig. 7.7 the wave diagram for the projectile with the 95 mm step can be seen. Two pressure pulses have been generated. The time between the first (face shock) and the second pressure pulse (1st step shock) is much longer in comparison to Fig. 7.6 due to the longer step of the projectile. Again the pressure stays constant between the first and the second pressure peak, which is a result of a constant particle velocity in the water. In the pressure trace of the second transducer the interference of the reflected shock wave can be seen between the first and the final pressure peak.

A triple shock wave can be seen in the wave diagram of Fig. 7.8 and in the pressure history of Fig. 7.9. Figure 7.9 only shows the pressure trace of the first transducer. As in the experiment with a single step, the first pressure peak (face shock) is

generated by the impact of the top part of the projectile. The second (1st step shock) and the third pressure rise (2nd step shock) are generated with the first and the second step respectively. Again the pressure stays constant behind the first and the second pressure peak due to a constant particle velocity in the water. The time duration between the second and the third pressure peak increases for the double stepped projectile (volume ratio ~ 0.5) due to the longer step and the bigger volume of the void part of the second step.

A simple one-dimensional calculation has been performed to predict the time intervals between the pressure peaks and their dependence of the impact velocity of the projectile. In the calculations the deceleration of the projectile was calculated using equation 6.12. The dynamic change of density in the water was calculated stepwise for small time intervals by using the pressure information of the experiment.

The results of tests with different impact velocities for the single and double edged projectiles in comparison to the above described calculations are shown in tables 7.1 - 7.4. In Tables 7.1 and 7.2, p_1 is the first and p_2 the second pressure peak in MPa. p_{1av} is the average of the constant pressure between the first and the second pressure peak. Δt is the time difference between the pressure peaks in μs. In Tables 7.3 and 7.4, p_1 is the pressure of the first, p_2 the pressure of the second, and p_3 the pressure of the third pressure pulse in MPa. Again p_{1av} stands for the constant pressure between the first and the second pressure peak. Δt_1 is the time difference between the first and the second and Δt_2 is the time between the first and the last pressure peak in μs.

$V_i[m/s]$	Δt	Δt_{cal}	$p_1[MPa]$	$p_{1av}[MPa]$	$p_2[MPa]$
32.5	553.6	490.0	25.7	11.88	30.67
37.5	452.0	434.0	27.3	14.9	37.7
38.1	451.0	410.0	22.0	15.83	45.4
45.2	404.4	372.0	30.45	22.67	50.0

Table 7.1: Test results for the single step projectile [short]

$V_i[m/s]$	Δt	Δt_{cal}	$p_1[MPa]$	$p_{1av}[MPa]$	$p_2[MPa]$
27.5	1678.2	1725	6.0	3.8	31.3
30.3	1531	1519.5	11.8	3.9	36.07
36	1344.5	1380	11.16	6.6	45.0
38	1197.3	1240	13.11	5.9	47.6

Table 7.2: Test results for the single step projectile [long]

$V_i[m/s]$	Δt_1	Δt_2	Δt_{1cal}	Δt_{2cal}	P_1	P_{1av}	P_2	P_3
33	459.2	628.1	422.0	636.0	11.2	4.0	13.17	43.7
39	357.4	557.6	364.0	570.0	17.0	5.1	16.0	49.0
43	345.6	506.5	328.0	508.0	15.5	6.17	20.0	54.8
49.2	342.0	436.0	288.0	424.0	15.3	7.99	20.5	65.2

Table 7.3: Test results for the double step projectile [volume ratio ~ 0.3]

$V_i[m/s]$	Δt_1	Δt_2	Δt_{1cal}	Δt_{2cal}	P_1	P_{1av}	P_2	P_3
35.5	357.2	569.6	272.0	582.0	10.2	4.63	9.01	25.66
40	231.7	553.5	248.0	546.0	12.8	5.81	12.5	49.3
46	267.0	475.0	210.0	450.0	9.55	6.2	14.0	61.5
50	247.5	447.7	202.0	438.0	17.3	8.9	17.3	65.1

Table 7.4: Test results for the double step projectile [volume ratio ~ 0.5]

The results presented in Tables 7.1 to 7.4 show that the strength of the initial pressure peak of the double and triple shock waves p_1 seems to have a random behaviour since the maximum pressure does not necessarily increase with increasing impact velocity of the projectile. A possible explanation could be the absorption of this, in comparison to normal shock waves, very short pressure peak due to the complex flow around the front face of the projectile into the gap which results in the generation of micro-bubbles and cavitation. In contrast to the behaviour of the initial pressure peak, the constant pressure between the first and second pressure peak increases with increasing impact velocity. This constant pressure also depends on the area of the top part of the projectile. A higher constant pressure can be seen for the projectiles with a larger impact area. The time duration between the first and the second pressure peak in the results for the single stepped projectile increases with increasing length of the step. The long stepped projectile yields a time duration which is more than double the time of the short stepped projectile. The same is true for the double stepped projectiles. With decreasing length of the steps the time between the pressure peaks decreases. The average time between the second and the third pressure peak in relation to the time between the first and the third pressure peak is 29 % (volume ratio of ~ 0.3) for the double-steeped projectile. The double stepped projectile with a volume ratio of ~ 0.5 yields an average time relation of 46 % (see table 7.3 and 7.4 respectively).

7.3 FINITE ELEMENT MODELING OF THE PRESSURE HISTORY

An attempt has been made to model the impact process of the projectile on the water surface. The commercial, two dimensional finite element program AUTODYN 2.66 has been used. The program allows alternative numerical processors to be selectively used to model different components and regions of a problem. AUTODYN 2.66 includes a Lagrange processor for modeling problems with small distortions, an Euler processor for fluids or solids with large distortions, an ALE (Arbitrary Lagrange Euler) processor for specialised flow models and a shell processor for modeling thin structures [36].

In order to simulate the impact of the projectile on the water surface and the propagation of the liquid shock wave in the shock tube, an axisymmetric model of the shock tube has been set-up. According to the experimental set-up the modeled water section of the shock tube has a length of 1.65 m and an inner diameter of 56 mm. The length, and with that the mass of the impacting projectiles, was also chosen to be identical with the real projectiles. The material properties for water have been taken from the AUTODYN material library. The equation of state used in the simulation for the water section was 'shock' and the strength model 'hydro'. For the steel and aluminium projectiles the material properties given in the AUTODYN material library have been used as well. The material properties for the plastic projectile, which was manufactured out of delrin have been obtained from DuPont Engineering Polymers. The projectiles have been modeled by using the von Mises strength model and a linear equation of state. Since no large distortions and deformations occur the impact process of a plane projectile can be numerically modeled by using the Lagrange processor. The shock tube wall and the end wall were simulated by defining a simple boundary condition to prevent material from being transported beyond these points. The results of the numerical simulation for the impact of a plane steel and plastic projectile and comparison to experimental results can be seen in the following figures (Figs. 7.10 - 7.14). A good qualitative agreement between experiment and model could be reached. As the wave diagrams show, it was possible to model the behaviour of the liquid shock wave in the shock tube. The comparison shows that for the numerical models lower impact velocities are needed to yield comparable results. In the steel projectile simulation an impact velocity of 40 m/s was needed to generate the wave diagram shown in Fig. 7.10. In this case a liquid shock wave with a maximum pressure of 67 MPa, an energy

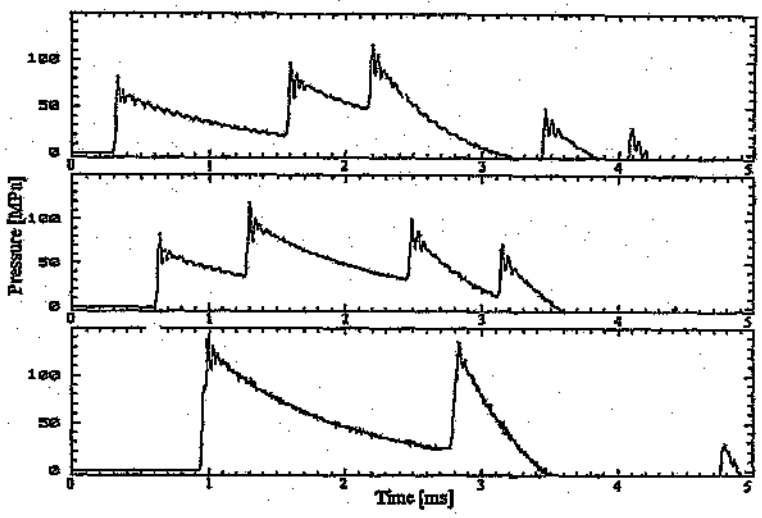

Figure 7.10: AUTODYN 2D-model: Liquid shock wave pressure history for the impact of the 3.665 kg steel piston. $V_{imp} = 40\ m/s$. Transducer position 1,2,3

of 3169.2 J and an impulse of 114.8 Ns has been generated. The comparable experimental liquid shock wave, which can be seen in Fig. 7.11 has been generated with an impact velocity of $\sim 50\ m/s$. The maximum pressure of the experimental shock wave is 65.3 MPa, the energy 3167.8 J and the impulse 122.5 Ns. These results show that the contour of the simulated liquid shock wave is in good agreement with the experimental one. A comparison of the shock wave velocities shows that the simulated shock wave travels faster than the experimental shock wave which is presumably due to the neglecting of impurities and dissolved gases in the water.
In Fig. 7.12 the velocity field at the end wall shortly after the reflection of the initial liquid shock wave can be seen. The reflection at the end wall results in approximately double the pressure at the end wall, which can bee seen in Figs. 7.10 and 7.11. In addition the particle velocity in the wake of the reflected shock wave drops down to zero, as shown in Fig. 7.12. An interesting result obtained from the finite element calculation is the compression of the water column due to the impact of the steel piston. The maximum compression of the water column is 35 mm at the time the reflected shock wave hits the steel projectile, which is still compressing the water. The impact of the reflected shock wave on the steel piston stops a further compression of the water and pushes the projectile backwards. This result confirms the calculation performed in section 6.2.

The results of the simulated impact of a Delrin plastic piston can be seen in Fig.

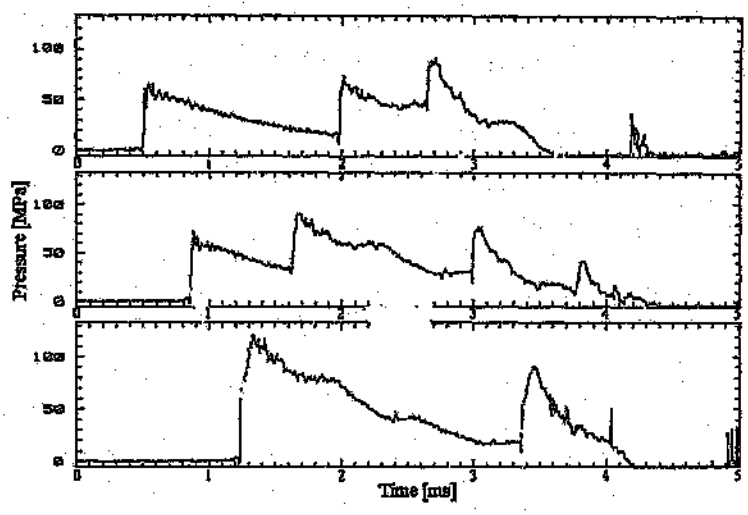

Figure 7.11: Experimental liquid shock wave pressure history for the impact of the 3.665 kg steel projectile. $V_{imp} \sim 50\ m/s$. Transducer position 1,2,3

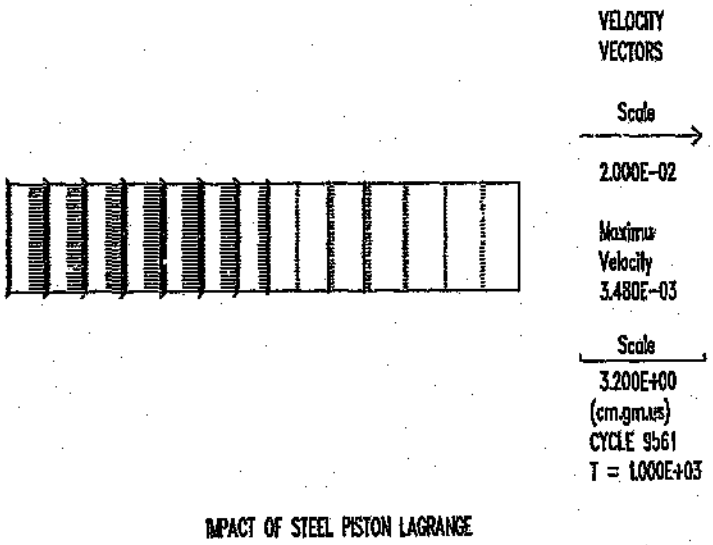

Figure 7.12: AUTODYN 2D-model: Velocity field at the end of the liquid shock tube just after wave reflection (velocity scale units in $[cm/\mu s]$ and dimension scale units in $[cm]$)

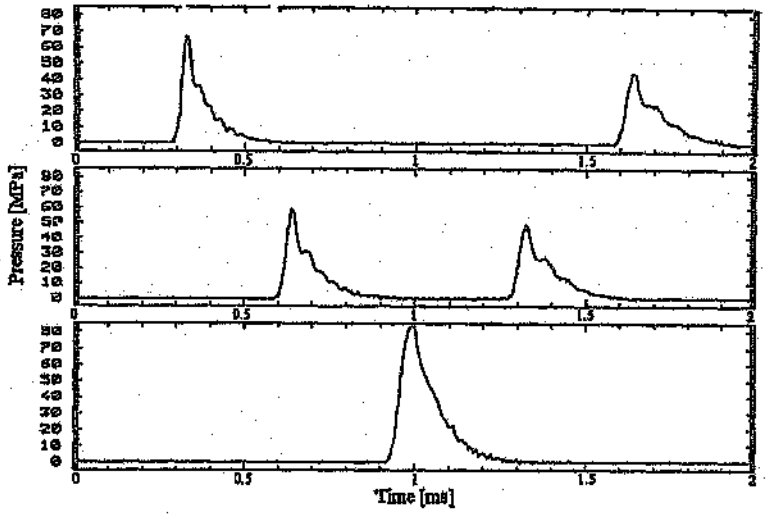

Figure 7.13: AUTODYN 2D-model: Liquid shock wave pressure history for the impact of the 0.2 kg plastic projectile. $V_{imp} = 50\ m/s$. Transducer position 1,2,3

7.13. The simulated shock wave yields an energy of 290.6 J, a maximum pressure of 66.36 MPa and an impulse of 12 Ns. The impact velocity in the simulation was $50 m/s$. For comparison a liquid shock wave with the same amount of energy 293.9 J is shown in Fig. 7.14. The impact velocity of the projectile was $\sim 70\ m/s$. The experimental liquid shock wave has a maximum pressure of only 51 MPa and an impulse of 17.3 Ns. This means that the contour of the simulated shock wave is a little bit different in comparison to the experiments'. Despite a higher maximum pressure the modeled shock wave yields a lower pressure energy and impulse which is due to a steeper pressure decrease behind the initial pressure jump.

To simulate the impact of a projectile with a stepped surface the water section has to be calculated by using an Euler processor since large distortions occur for the impact surface. The projectile is still defined in Lagrange. Both processors can be coupled by using a polygon to define the Lagrange surface interacting with the Euler mesh. The clearance gap between the stepped projectile and the shock tube wall is defined as a void Euler mesh to allow this space to be filled with water during the impact since the Euler framework is fixed and no masses can be transported beyond the original defined mesh. Therefore no boundaries have to be specified for the Euler modeled water section. As an example the pressure history of the single stepped piston with an impact velocity of 37.5 m/s is shown in Fig. 7.15. The corresponding pressure history of the experimental test is shown in Fig. 7.6. The comparison shows

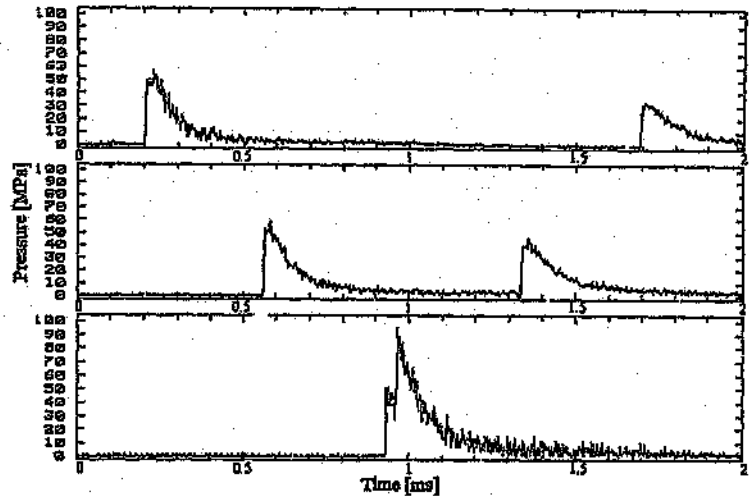

Figure 7.14: Experimental liquid shock wave pressure history for the impact of the 0.2 kg plastic projectile. $V_{imp} \sim 70\, m/s$. Transducer position 1,2,3

that the numerical model is in good agreement with the experimental shock wave. The numerical shock wave reveals the initial pressure peak which is followed by a constant pressure up to the second pressure peak as noted in the experiments. The maximum pressure and the shock wave velocity are higher for the numerical model as already mentioned earlier in this section. The results of the numerical simulations for different impact velocities are shown in Table 7.5, where p_1 is the first and p_2 the second pressure peak in MPa. p_{1av} is the average of the constant pressure between the first and the second pressure peak. Δt is the time difference between the pressure peaks in μs. To allow comparisons of the numerical results with the experimental results (see table 7.1) the impact velocities in the simulation have been chosen to be identical with the experimental impact velocities. The comparison of the two tables shows for all impact velocities that the initial pressure peak and the second pressure peak of the computed shock waves are higher than the peaks of the experimental ones. In contrast to this the constant pressure p_{1av} of the simulation is in good agreement to the experimental constant pressure. Again a possible explanation for this could be partial absorption of the very short pressure peaks due to dissolved gases in the water. This absorption is not as significant as for the short pressure peaks due to its longer time period.

The time differences Δt shown in table 7.5 are smaller than the ones obtained from the experiments. This can be explained by the neglecting of friction between the projectile and the shock tube wall in the numerical model.

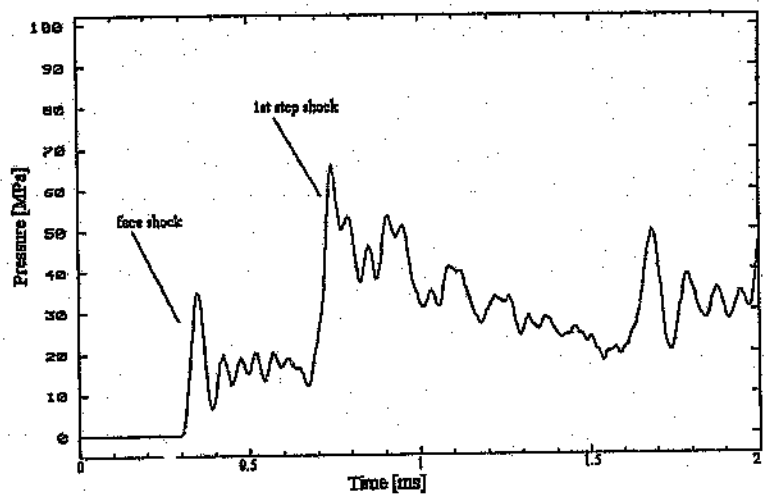

Figure 7.15: AUTODYN 2D-model: Liquid shock wave pressure history for the impact of the single stepped projectile [short]

V_i $[m/s]$	Δt	p_1 $[MPa]$	p_{1av} $[MPa]$	p_2 $[MPa]$
32.5	399.9	30.1	13.16	46.6
37.5	352.5	34.0	15.83	58.8
38.1	340	34.5	17.05	66.9
45.2	332	43.5	22.78	80.1

Table 7.5: AUTODYN 2D results for the single step projectile [short]

8 FORMING OF CIRCULAR METAL DISKS

The deformational behaviour of circular metal disks under the impact of liquid shock waves is discussed in this chapter. Experiments have been performed to determine the stress and strain state of the disks. A theoretical approach is given to predict the maximum midpoint deflection. The deformation process is optically investigated and the strain rates are calculated. A finite element model is presented and the numerical results are compared with the experimental results.

8.1 STRAINS AND STRESSES OF DEFORMED METAL PLATES

The stress and strain state of a deformed metal can be determined by measuring the deformation of the formed part. The free forming of circular disks has been performed with copper and mild steel disks.
To determine the three strains ϵ_r, ϵ_θ, ϵ_T of the metal disks after the deformation process the displacement of a grid is measured. The grid is painted with a template onto the disk before the test. From the measured displacements the natural strains can be calculated by using the following equations:

$$\epsilon_r = ln\frac{r_i}{r_{i0}} \tag{8.1}$$

$$\epsilon_\theta = ln\frac{R_i}{R_{i0}} \tag{8.2}$$

$$\epsilon_T = ln\frac{T_i}{T_{i0}} \tag{8.3}$$

The constancy of volume is given by:

$$\epsilon_r + \epsilon_\theta + \epsilon_T = 0 \tag{8.4}$$

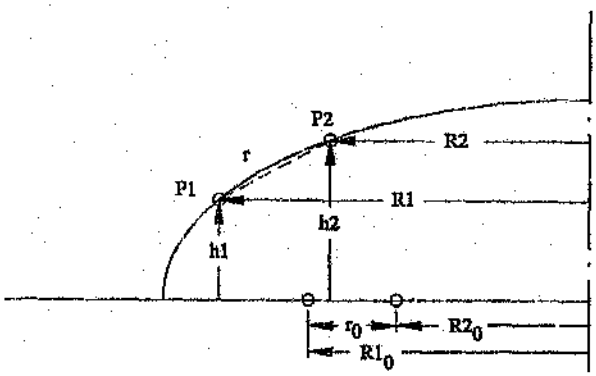

Figure 8.1: Measurements of circumferential and radial strains



Figure 8.2: Pictures of deformed copper disks. Thickness 0.55 *mm*. From left to the right hand side: 10.95, 13.45, 14.4, 16.15 *mm* midpoint deflection



Figure 8.3: Pictures of deformed copper disks. Thickness 0.9 *mm*. From left to the right hand side: 16.03, 17.22, 17.5, 19.0 *mm* midpoint deflection

To determine the circumferential and radial displacements of the grid, a Nikon Profile Projector with a zoom of 10 is used. The adjustment of the profile projector is vertical to the plate and therefore only the radius R_i can be measured. The radial displacement r has to be calculated from the radius R_i and the actual height of the point. The distance between two points is approximated as a straight line (see Fig. 8.1). The height of the points on the deformed disks is measured with a normal clock gauge. The thickness of the disk is measured with an electronic gauge (Heidenhahn MT 60). The accuracy of this measuring device lies within 0.001 *mm*.

In Fig. 8.2 and 8.3 photographs of several copper test plates are shown. The maximum midpoint deformation increases from the left to the right hand side. The following pictures (Fig. 8.4 and Fig. 8.5) show a typical example of the strain measurements of a deformed copper plate. The variation of the height and the thickness over the radius is shown in Fig. 8.4. The picture shows that the disk

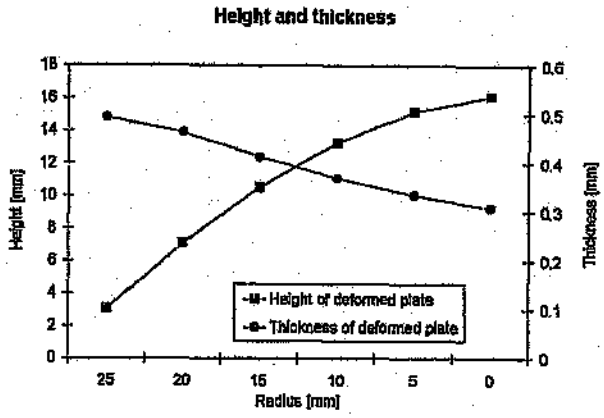

Figure 8.4: Variation of height and thickness for a 0.55 mm copper disk after impact of a shock wave with $p_{max} = 25.56\ MPa$, $E = 116.96\ J$ and $I = 10.97\ Ns$

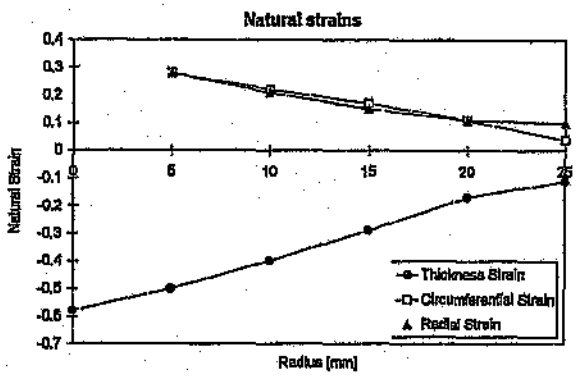

Figure 8.5: Variation of natural strains for a 0.55 mm copper disk after impact of a shock wave with $p_{max} = 25.56\ MPa$, $E = 116.96\ J$ and $I = 10.97\ Ns$

was deformed to a dome profile. The deflection thickness ratio in this case was $D/T = 29.36$. Fig. 8.5 shows the variation of the natural strains over the radius. In literature (e.g. Wilson [12]) the strain conditions for a bulged disk are reported to be balanced biaxial. That means that the stresses in the radial and circumferential directions are equal and therefore $\epsilon_r = \epsilon_\theta = -0.5\ \epsilon_T$. In Fig. 8.5 it can be seen that this is true for the top of the dome up to a radius of approximately 20 mm. At the outer part of the dome the circumferential strain tends towards zero due to the clamping of the disk. The results of the strain measurements also show good agreement with the constancy of volume (equation 8.4).

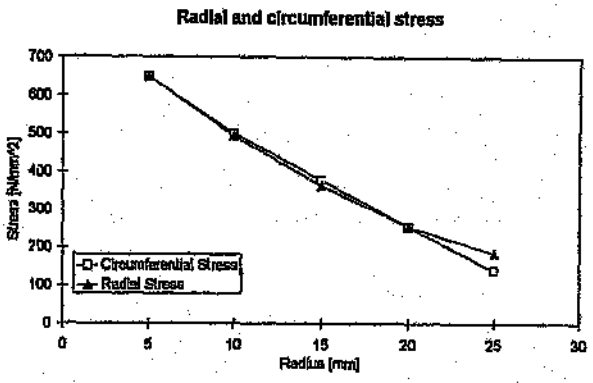

Figure 8.6: Variation of stresses for a $0.55mm$ copper disk after impact of a shock wave with $p_{max} = 25.56MPa$, $E = 116.96J$ and $I = 10.97Ns$

The stress state of the deformed part can be determined by using the Levy - Mises plastic stress strain relationship:

$$d\epsilon_r = \frac{1}{C}\left[d\sigma_r - \nu\left(d\sigma_\theta + d\sigma_T\right)\right] \tag{8.5}$$

$$d\epsilon_\theta = \frac{1}{C}\left[d\sigma_\theta - \nu\left(d\sigma_T + d\sigma_r\right)\right] \tag{8.6}$$

$$d\epsilon_T = \frac{1}{C}\left[d\sigma_T - \nu\left(d\sigma_\theta + d\sigma_r\right)\right] \tag{8.7}$$

Since the plastic behaviour of the metal is non - linear the equations are expressed in incremental form. Due to the constancy of volume (Eq. 8.4) the Poisson's ratio is $\nu = 0.5$. The constant C is the secant modulus of the effective stress strain diagram. The Levy - Mises equations neglect the elastic strains and are therefore only valid for large deformations. Since the assumption of a balanced biaxial loading condition is made, the principal axes of strain have a fixed orientation due to the principal stresses and strains being equal ($\epsilon_r = \epsilon_\theta$; $\sigma_r = \sigma_\theta$) and due to zero shear stress on all planes. Therefore Eqs. 8.5 - 8.7 can be written in terms of total strain. Another assumption is that the sheet metal is very thin and therefore σ_T is equal to zero. In Fig. 8.6 the radial and circumferential stress distribution of the same deformed copper plate can be seen as a typical example. The stress values have been calculated by using Eqs. 8.5 - 8.7 and by using the natural strains which are shown in Fig. 8.5. Near the centre of the dome the radial stress is equal to the circumferential stress due to the balanced biaxial behaviour. Towards the outer parts of the disk the circumferential stress tends towards zero.

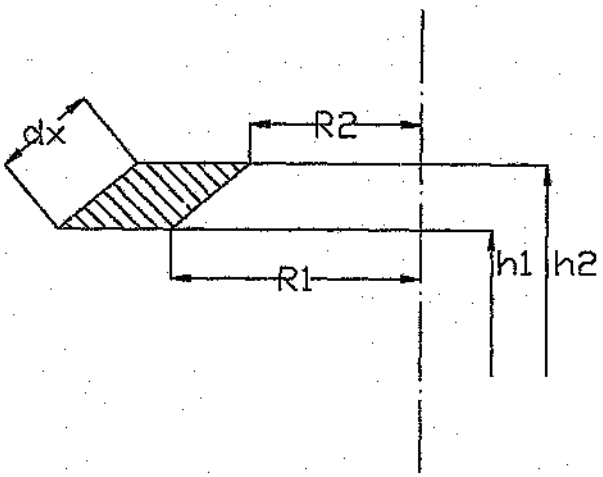

Figure 8.7: Geometry of circular ring element

8.1.1 DEFORMATION ENERGY FOR CIRCULAR PLATES

In section 6.3 the equation for the deformation energy per unit volume has been derived. The total deformation energy of the circular plate can now be calculated by using the radial, height and thickness strains, which have been determined in section 8.1. The calculation of the deformation energy is divided into six parts becauss the measurements mentioned above have been performed six times over the radius of the test specimen.

$$W = \sum_{i=1}^{6} \left(\frac{K}{n+1} \right) (\bar{\varepsilon})_i^{n+1} V_i \tag{8.8}$$

The effective strain is defined as [12]:

$$\bar{\varepsilon} = \sqrt{\frac{2}{9} \left[(\epsilon_\theta - \epsilon_r)^2 + (\epsilon_\theta - \epsilon_T)^2 + (\epsilon_T - \epsilon_r)^2 \right]} \tag{8.9}$$

The effective strain states that ductile failure at any point in a body under any combination of stress begins only when equal to the strain energy of distortion absorbed per unit volume at any point in a simple tension specimen [12]. Equation 8.9 is only valid for an idealised metal where the deformation is isotropic [37].

For the calculation of the effective strain the radial, the circumferential and the thickness strains, which have been determined from the deformed disk, are used. The volume of the test specimen is integrated using a circular element (see Fig. 8.7) of the deformed plate.

$$dV = 2\pi T R\, dx$$

$$V = 2\pi T \int_{R2}^{R1} \sqrt{1 + \left(\frac{h2 - h1}{R1 - R2}\right)^2}\, R\, dR$$

For the circular element the thickness and the strain is assumed constant.

$$V_i = \pi T_i \sqrt{1 + \left(\frac{h_{i+1} - h_i}{R_i - R_{i+1}}\right)^2} \left(R_i^2 - R_{i+1}^2\right)$$

The values for the deformation energy calculated using equation 8.8 can be seen in Table 8.1. For copper the material properties of the static tensile tests have been used since these values stay constant up to strain rates of $10^4\ s^{-1}$ (see section 4.4). The material properties for mild steel change with increasing strain rates and therefore the dynamic properties determined by Bramley and Melor [32] have been used.

The table shows that for test specimens out of copper and mild steel the results of the calculated deformation energy are very similar to the measured energy of the liquid shock wave. That means that the shock wave energy is nearly completely transformed into deformation energy. This is in good agreement with the experimental results since the liquid shock waves always get completely absorbed by the deforming specimen.

For copper, machined specimens and sheet material have been used in the experiments. In general the sheet material reveals a better agreement with the calculation since the machined specimen vary in thickness due to the tolerances given. A typical pressure history for a test with a copper test specimen can be seen in Fig. 8.8. The pressure trace for transducer 3, which is located 25 mm above the metal plate shows the transaction between the deforming metal specimen and the impacting liquid shock wave very well. The incoming shock wave travels with a velocity of 1501.6 m/s and impacts 17.6 μs after passing the third transducer. For a very short period the shock wave gets reflected before the metal starts to deform. This reflection can be seen in the small second peak on the initial shock wave. The information of the deformation of the copper disk reaches the third transducer 39.25 μs after the initial shock wave has passed the transducer, which results in a sudden pressure drop in the pressure history. In addition no further reflection of the shock wave can be seen which leads to the conclusion that the pressure energy gets nearly completely absorbed by the deformation process.

For the mild steel specimen the difference between the deformation energy and the shock wave energy is a little bigger. This difference between the energies is due to a

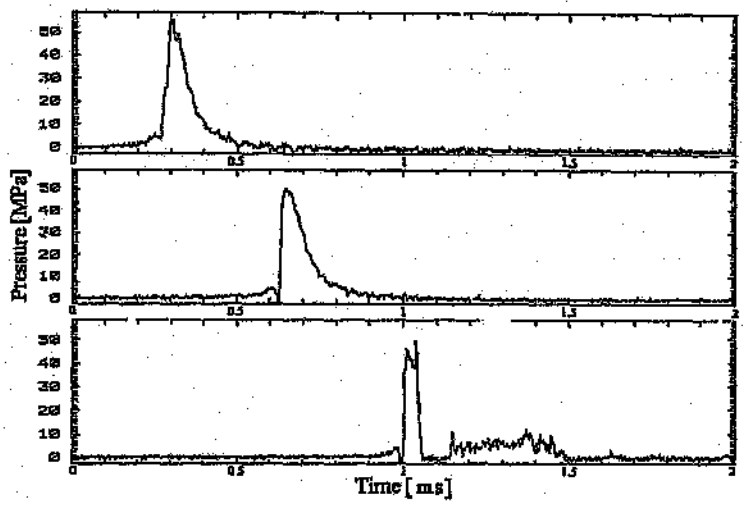

Figure 8.8: Pressure history for a liquid shock wave impacting on a copper specimen

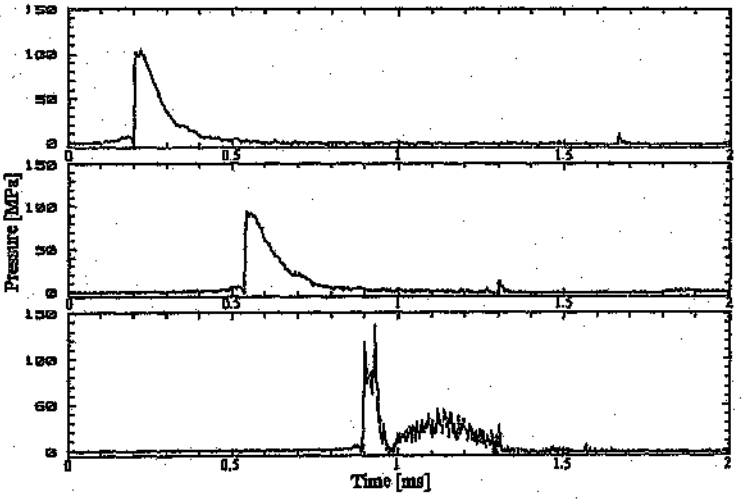

Figure 8.9: Pressure history for a liquid shock wave impacting on a mild steel specimen

Thickness [mm]	Shock Wave Energy [J]	Deformation Energy [J]	Max. Deformation [mm]
Copper sheet:			
0.55	45.88	43.02	10.95
0.55	79.25	73.5	13.45
0.55	90.4	79.26	14.4
0.55	116.96	105.56	16.15
0.9	144.3	135.05	16.03
0.9	183.5	163.96	17.5
0.9	184.9	161.94	17.22
0.9	219.6	178.27	19.00
Copper machined:			
0.55	26.2	33.7	8.96
0.55	32.97	45.29	9.95
0.55	38.14	48.49	9.99
0.55	40.2	44.4	9.77
0.9	26.84	20.38	7.5
0.9	39.1	24.42	8.4
0.9	41.77	34.28	7.72
0.9	68.65	57.2	9.75
0.9	88.43	60.0	11.67
0.9	98.22	74.5	11.15
0.9	162.2	130.3	14.85
0.9	181.0	144.09	14.25
0.9	193.95	171.7	15.0
0.9	198.99	166.99	15.95
1.5	210.9	147.6	12.45
1.5	277.9	197.7	14.50
Mild steel sheet			
1.6	210.0	140	6.37
1.6	569.1	491	12.28
1.6	701.3	649	14.43
1.6	703.2	685	14.90
1.6	1064.1	827	16.77

Table 8.1: Comparison of deformation energy with shock wave energy for machined copper and mild steel specimen and for sheet material

higher resistance and spring back of the mild steel specimen. This can be seen in Fig 8.9. ming shock wave is travelling with a speed of 1568 m/s and impacts on the [illegible] μs after passing the transducer. A first reflection can be seen in the second peak on the initial shock wave. The information of the deformation of the metal disk reaches the transducer 35 μs after the initial shock wave has passed the transducer. 63 μs later the deformation slows down and the pressure starts rising slowly again. A small pressure wave travelling back up the shock tube can be seen.

8.2 PREDICTION OF MIDPOINT DEFLECTION

As shown in the previous section 8.1.1 almost the total amount of the pressure energy of the liquid shock wave is transformed into deformation energy of the metal specimen. This gives the possibility to predict the maximum deflection of the bulged disk and its dependence on the input energy by just using the material properties, the thickness of the metal disk and by assuming a cone as the final deformed shape. First of all it is necessary to determine the volume of the metal being deformed. The radial, circumferential, and thickness strains depend on the stress condition for the high velocity forming. As the experiments show the stress condition for a bulged disc is similar to the balanced biaxial tension and therefore the thickness reduction is given by:

$$\epsilon_r = \epsilon_\theta = -\frac{\epsilon_T}{2} \tag{8.10}$$

$$\epsilon_T = ln\frac{T}{T_0} = -2\epsilon_r$$

$$T = T_0 e^{-2\epsilon_r} \tag{8.11}$$

It is assumed that the final shape of the deformed circular plate is similar to a cone (see Fig. 8.10).

For the cone the differential volume element is:

$$dV = 2\pi RT dx$$

with

$$dx = \sqrt{1 + \left(\frac{y}{R_0}\right)^2}\, dR$$

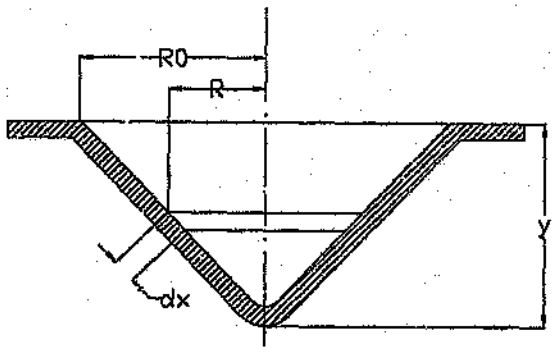

Figure 8.10: Geometry of deformed disk

After integration the volume of the deformed disc can be calculated:

$$V = \pi T_0^2 \sqrt{1 + \left(\frac{y}{R_0}\right)^2} \tag{8.12}$$

To compute the average thickness of the deformed disc the average radial strain ϵ_{av} has to be calculated first:

$$\epsilon_{av} = ln \frac{\sqrt{R_0^2 + y^2}}{R_0}$$

This leads to an average thickness T_{av} of:

$$T_{av} = T_0 e^{-2ln\sqrt{1+(y/R_0)^2}}$$

With the average thickness the average volume V_{av} of the deformed metal can be calculated:

$$V_{av} = \frac{\pi T_0 R_0^2}{\sqrt{1 + (y/R_0)^2}} \tag{8.13}$$

The assumption of an average strain leads to a small contradiction in the assumption of an incompressible material since $V_{av} \neq V_0$. However the error is in general less than 10%. For the largest deformation of 19 mm the error increases to 15%.

Using equation 8.9 and the relationship for balanced biaxial tension (eqn. 8.10) the effective strain can be calculated to be:

$$\bar{\epsilon} = 2\, ln \sqrt{1 + \left(\frac{y}{R_0}\right)^2} \tag{8.14}$$

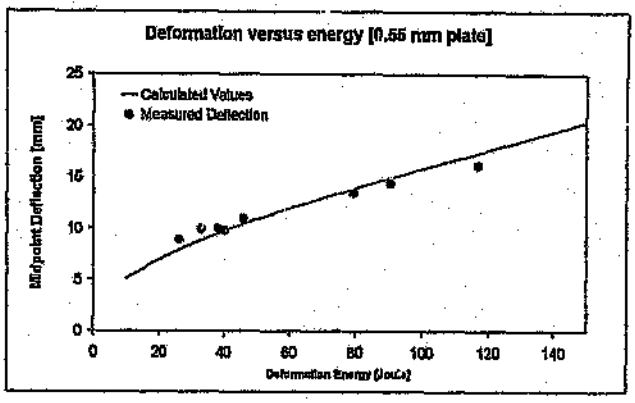

Figure 8.11: Comparison of calculated and experimental midpoint deflection for 0.55 mm copper plates

Combining the equations 6.3, 8.13 and 8.14 leads to an expression for the deformation energy depending on the midpoint deflection and the material constants of the bulged disk.

$$W = \frac{K}{n+1}\left[2ln\sqrt{1+\left(\frac{y}{R_0}\right)^2}\right]^{n+1}\frac{\pi T_0 R_0^2}{\sqrt{1+\left(\frac{y}{R_0}\right)^2}} \tag{8.15}$$

Since the shock wave energy is nearly completely transformed into deformation energy, W can be exchanged with the energy of the liquid shock wave E. Equation 8.15 is now just a function of y ($E = f(y)$) and the midpoint deflection can therefore easily be predicted by using the above equation.

Fig. 8.11 to Fig. 8.14 show the results of the performed calculation in comparison to experimental results. The experiments have been performed with 0.9 mm and 0.55 mm circular copper disks and 1.6 mm, 1.0 mm and 0.5 mm circular mild steel disks. For the calculation the static material properties for copper and the dynamic material properties according to [32] have been used. In Fig. 8.13 the calculated curve for both, static and dynamic material properties are shown and it can be seen that the deformation energy due to the high strain rates increases.
Overall the results show excellent agreement between the calculated curve and the experimental values considering the approximations that have been made. The maximum difference between calculation and experimental results for both materials is smaller than 15 % and the above theoretical approach can be used to estimate the midpoint deflection of circular disks.

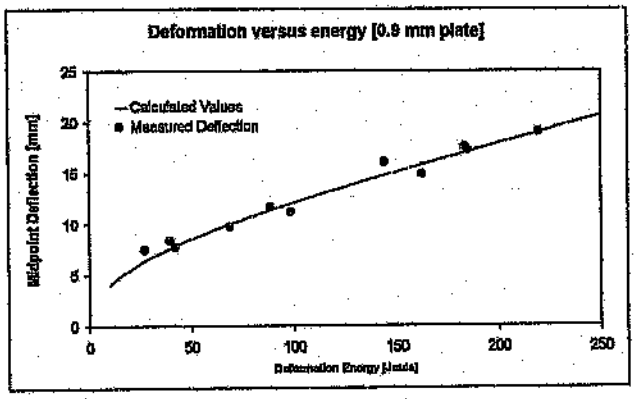

Figure 8.12: Comparison of calculated and experimental midpoint deflection for 0.9 *mm* copper plates

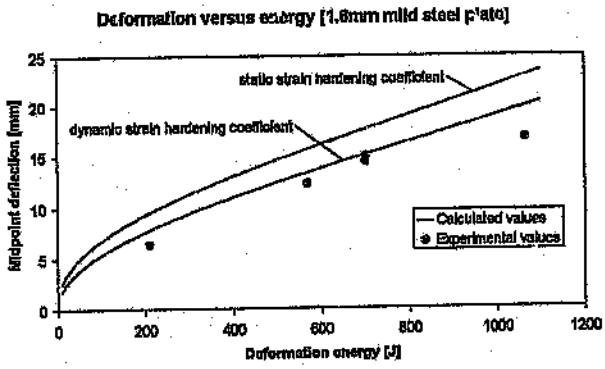

Figure 8.13: Comparison of calculated and experimental midpoint deflection for 1.6 *mm* mild steel plates

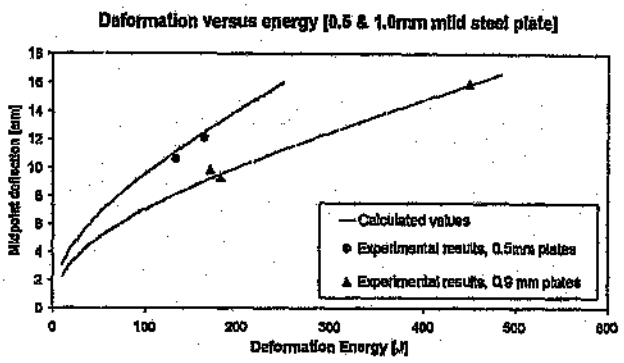

Figure 8.14: Comparison of calculated and experimental midpoint deflection for 1.0 *mm* and 0.5 *mm* mild steel plates

8.3 OPTICAL INVESTIGATIONS OF THE DEFORMATION PROCESS

The experimental set-up described in section 4.3 allows the production of pictures of the metal deformation during the impact of the shock wave. Good results have been obtained for a camera setting of three to four superimposed pictures with an exposure time of 11 μs each. A larger number of pictures reduces contrast due to the superimposing and it has been found difficult to separate them. Tests have been performed with copper and mild steel specimens machined out of thick plates. The design of the specimens and the test section is shown in Fig. 4.7 and 4.9 respectively. The behaviour of the machined specimens has been found to be very similar to the behaviour of fully clamped circular disks. Measurements of the strains show a good accordance of both types of specimen. Due to the machined and therefore rougher surface, the specimens out of solid tend to rupture at an earlier stage.

8.3.1 DEFLECTION TIME HISTORY AND DEFORMATION VELOCITY

In the following figures, pictures of the experiments are shown. For these experiments the 'FlashCam' has been used. The camera, and therefore the picture, is rotated by 90 degrees in order to have a higher resolution in the same direction as the deformation since the camera's resolution is 756 x 290 pixels. Due to the optical set-up only the enlarged centre part of the test specimen is visible. To magnify the

deformation process in the picture an aspect ratio of 2:1 was chosen. This leads to the oval shape of the test section window. The white line in the pictures shows the position of the undisturbed disk before the impact of the shock wave. In Fig. 8.15 the deformation process of a copper test specimen with a thickness of 0.55 mm is shown. The shock wave had a maximum pressure of $p = 28.6\ MPa$. The three superimposed pictures were taken at 80 μs, 151 μs and 222 μs after the impact of the shock wave. It can be seen that the deformation starts in the outer part of the test specimen and that the centre remains nearly flat. The plastic hinge, moving towards the centre, is clearly visible in the second picture. When the plastic hinge reaches the centre, the metal is pushed rapidly forward until the maximum deflection is reached. The existence of the plastic hinge was theoretically predicted in 1951 by Hudson [15] (see section 3). Johnson [11] pointed out that the material in the central region of the disk, bounded by the plastic hinge, is progressively, radially stretched and thinned whilst that in the conical region is rigid and stationary.
The local deformation velocities of the metal specimen at a certain deformation stage have been determined from the pictures and are shown in Fig. 8.15 as well. The velocity was calculated by measuring the difference in the position of the centre of the specimen for each picture. The time duration between each picture was obtained from the camera setting (80 μs for the first and 71 μs for the last two pictures). Thus the term local velocity represents the mean velocity between two successive frames.
From the first to the second picture the velocity drops from 58.4 m/s to 50.9 m/s. This velocity drop is due to the centre part staying behind the deformation of the outer part. From the second to the third picture the centre is rapidly folded forwards which leads to a large rise in the local velocity up to 95.5 m/s. The average velocity of the total deformation process, which is calculated from the three local velocities is 68 m/s.

In Fig. 8.16 two experiments with 0.9 mm copper plates subjected to a similar pressure pulse are shown. Fig. 8.16a shows the deformation of the plate at an early stage and Fig. 8.16b at the final stage. The three pictures of Fig. 8.16a have been taken 47 μs , 108 μs and 169 μs after the impact of the shock wave. The plastic hinge moving radially inwards can be seen very clearly. The behaviour of the local velocities in the centre of the disk is governed by the plastic hinge and changes rapidly at this early stage of deformation. After a fast acceleration of the disk due to the impact of the shock wave the movement of the centre slows down. The deformation is only taking place in the plastic hinge and the centre remains flat and nearly undisturbed. This can be seen in a major velocity drop from 73 m/s down to 50.5 m/s. With the plastic hinge folding the centre forward the velocity rises again

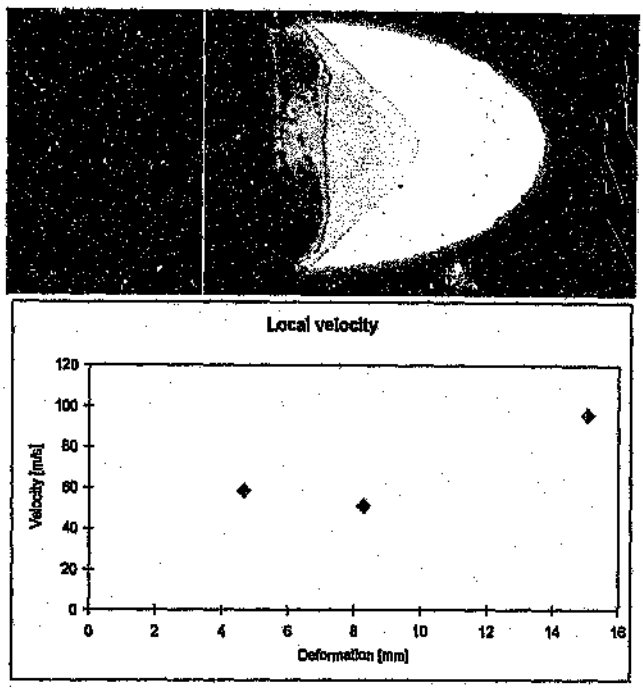

Figure 8.15: Pictures and local deformation velocities on the centre line of a copper specimen with a thickness of 0.55 mm. The maximum pressure of the shock wave is $p = 28.6\ MPa$, the impulse $I = 9.85\ Ns$ and the shock wave energy $E = 107.25\ J$

up to 80 m/s.

In Fig. 8.16b the pictures have been taken 67 μs, 128 μs and 189 μs after the impact of the shock wave. The deformation process is much further developed than in Fig. 8.16a, i.e. it shows the plastic hinge at a later stage. In the third picture the centre is already folded forward and the final shape is reached. A thin water jet ejected out of a small crack can also be seen in the third picture. These small ruptures occurred quite often in the test specimens due to the rougher surface after machining. For larger deformations tearing starts at these points. The local velocities for this test show a similar behaviour. The velocity of the centre at the second picture is slightly higher than in the first picture because the plastic hinge is further developed and has already accelerated the centre. The average velocity for this test is 82.6 m/s.

As an example of the deformation process of circular mild steel plates Fig. 8.17 shows the deformation process of a mild steel plate with an initial thickness of 1.0 mm. For this experiment the ultra high speed camera 'SensiCam' was used (see 4.3).

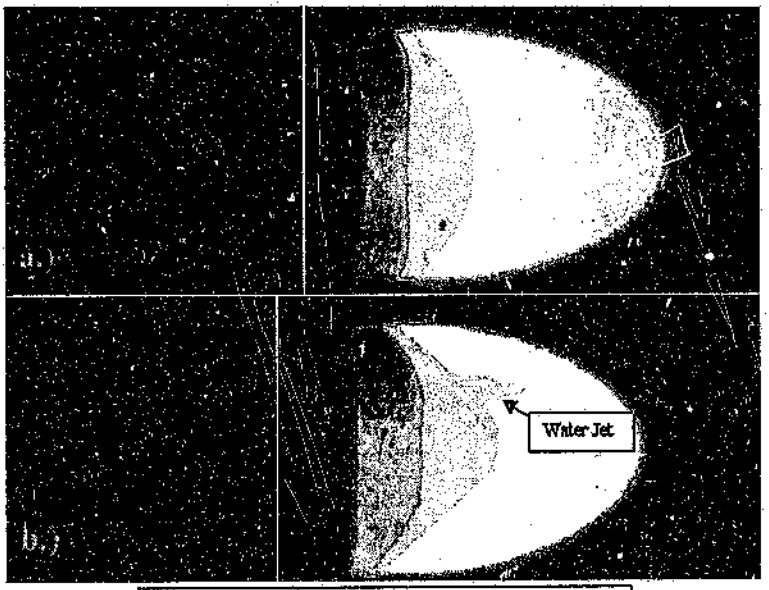

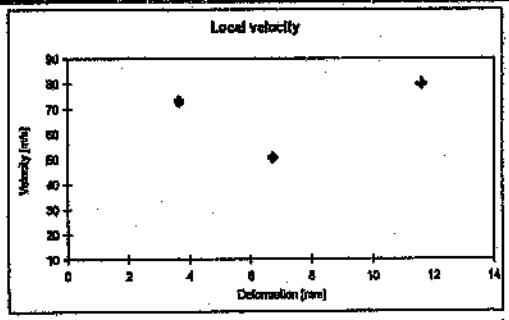

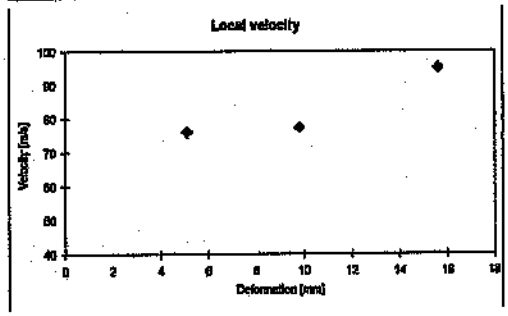

Figure 8.16: Pictures and local velocities on the centre line of two copper specimen with a thickness of 0.9 mm. $p_a = 36.4\ MPa$, $I_a = 11.8\ Ns$, $E_a = 162\ J$; $p_b = 40\ MPa$, $I_b = 11.64\ Ns$, $E_b = 181\ J$

The three superimposed pictures have been taken 57 μs, 118 μs and 232 μs after impact of the shock wave. The deformational behaviour of the mild steel specimen is quite similar to copper. The deformation commences in the outer part of the specimen. The plastic hinge can be seen in the first frame. In the first picture of the first frame the centre part is still undisturbed. In the second picture the plastic hinge has reached the centre. which is rapidly folded forwards. This results in a large increase in the local deformation velocity up to 111.8 m/s. The average deformation velocities of the mild steel specimens are comparable to the velocities of the copper specimens as well. The average deformation velocity in this test was 80.22 m/s.

In the following three figures the behaviour of the average deformation velocities with respect to maximum deformation, shock wave energy and shock wave impulse are presented for 0.55 mm, 0.9 mm and 1.5 mm copper and 1.0 mm mild steel specimens. The average deformation velocities have been calculated by using the peak deflection of the disk shown on the third superimposed picture and the time delay between impact of the shock wave on the disk and the recording of the third picture. In Fig. 8.18 the deformation velocity is plotted versus the peak deformation of the test specimens. The average velocity shows a linear behaviour and seems to be independent of the thickness and the material of the metal plates.

In Fig. 8.19 and 8.20 the average deformation velocity versus the shock wave energy and the impulse is shown. In both cases the curves do not reveal a linear behaviour. Therefore the values in these two figures are plotted in a log-log diagram to get an almost linear dependence for each curve.
In both figures the thinner plates in comparison to the thicker ones reach higher deformation velocities for a constant input energy. The specimens of mild steel, which need in general a higher deformation energy and which can sustain a larger impulse, reveal a dependence with the lowest slope.

Since the values in the energy and impulse diagram (Fig. 8.19 and Fig. 8.20) are drawn in logarithmic scale the curves reveal a quite linear behaviour. Therefore it can be estimated that the values behave according to a power law:

The dependence of the average deformation velocity on the energy:

$$v_{av} = cE^z + b$$

and the dependence on the impulse:

$$v_{av} = cI^z + b$$

The coefficients c, b, z can be obtained from the diagrams.

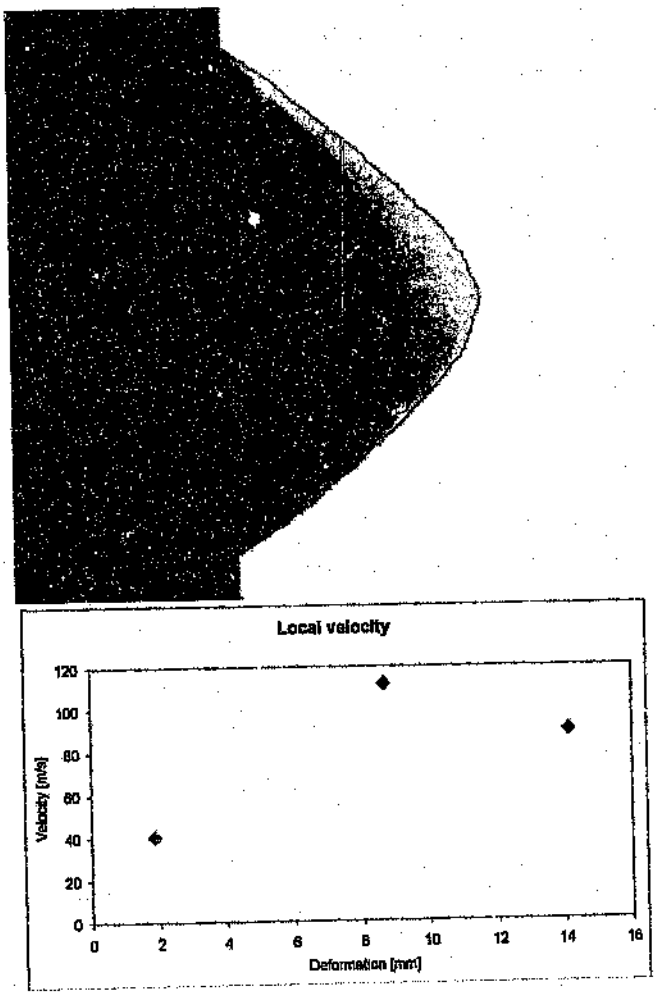

Figure 8.17: Pictures and local deformation velocities on the centre line of a mild steel specimen with a thickness of 1.0 mm. The maximum pressure of the shock wave is $p = 65.0\ MPa$, the impulse $I = 17.74\ Ns$ and the shock wave energy $E = 449.3\ J$

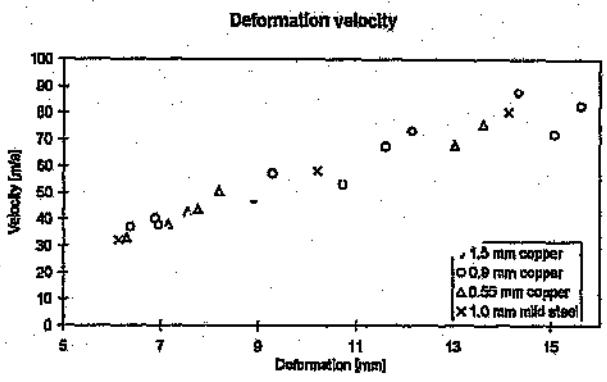

Figure 8.18: Average deformation velocity versus maximum deformation

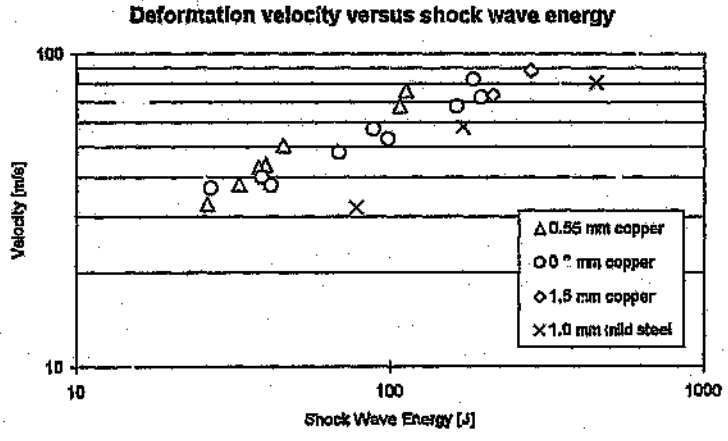

Figure 8.19: Average deformation velocity versus shock wave energy

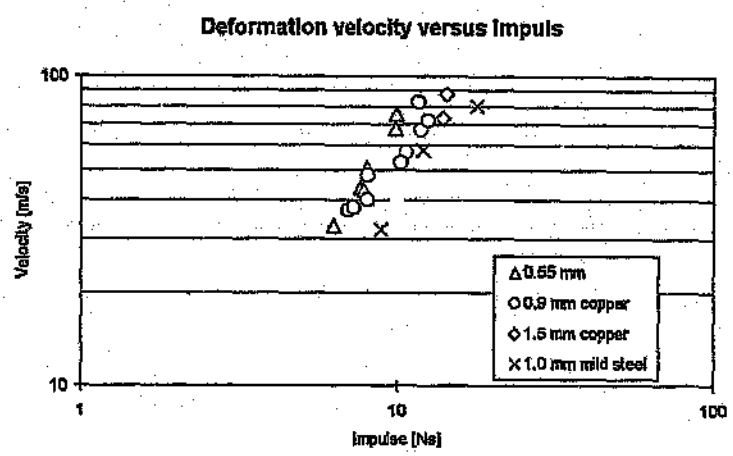

Figure 8.20: Average deformation velocity versus shock wave impulse

8.3.2 STRAIN RATES

From the time the metal needs to respond to the impulsive loading, the strain rates can be determined. For the natural strain the strain rate is defined as follows:

$$\dot{\epsilon} = \frac{d\epsilon}{dt} \tag{8.16}$$

The strain rate has an effect on the behaviour of the metal during the deformation process. In [12] the following table is given to classify the strain rates and to show their effects and the thermodynamic conditions.

Effect or condition	$0 - 10^{-3}\frac{1}{s}$	$10^{-3} - 10^{2}\frac{1}{s}$	$> 10^{2}\frac{1}{s}$
Isothermal	X		
Steady strain rate $\epsilon \neq f(x,t)$	X	X	
Increased resistance to flow		X	X
Adiabatic (thermodynamic)		X	X
Elastic & plastic wave propagation effects			X
Unsteady strain rate $\epsilon = f(x,t)$			X

Table 8.2: Basic strain rate effects and thermodynamic conditions [12]

From the table it can be seen that, in the static range, heat is dissipated fast enough to maintain isothermal conditions. As velocity increases, adiabatic conditions are

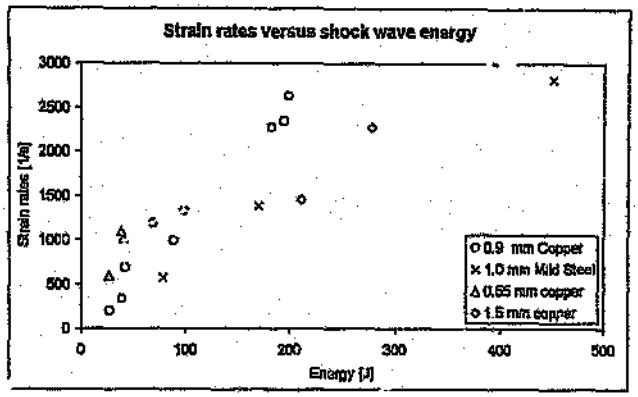

Figure 8.21: Strain rates versus liquid shock wave energy, circular disks

approached in which the heat does not dissipate from the specimen during the deformation process. Up to $10^2\ s^{-1}$ wave effects are negligible and a steady strain rate exists. That means that the strain is not a function of both position and time. For higher strain rates the resistance to flow increases, which leads in the dynamic stress strain diagrams to an elevation of the curve above the static one. The ductility of the metal under high strain rates depends on the material. It might increase, decrease or remain constant as for low strain rates.

The strain rates in this section are determined by using the effective strains calculated with eqn. 8.9 and the deformation times obtained from the experiments performed with the high speed video cameras. The average deformation speed has to be considered because the pictures do not automatically show the maximum deformation of the test specimen. The time difference between the largest deformation on the picture and the maximum deformation measured after the test is calculated using the average deformation speed. In Fig. 8.21 the strain rates versus the shock wave energy are shown. The results show in this range of strain rates a nearly linear behaviour.

8.3.3 STRAIN RATE MEASUREMENTS DURING THE DEFORMATION PROCESS

The optical set-up shown in Fig. 4.9 gives the possibility to study the behaviour of the metal specimen during the impact simultaneously from two directions. The set-up of the mirror system enables the camera to record the side view and the bottom view of the test specimen in one picture. The side view reveals the shape



Figure 8.22: Side and bottom view of deforming copper specimen showing two superimposed pictures at 122 μs and 244 μs

of the deformed specimen during the deformation as already described in section 8.3.1. The bottom view shows the movement of the grid, which was painted onto the specimen before the test and allows the strains during the deformation to be determined. By using the strains and the time at which the picture has been recorded the strain rates for that particular deformation stage can be calculated.

As an example Fig. 8.22 shows a picture of a 0.9 mm copper plate. The left side of the picture shows the side view and the right side shows the bottom view. The quality of the picture is not as good as the quality of the pictures in section 8.3.1 since the specimen had to be illuminated from the bottom and the side, which results in some reflections on the image. The photograph shows two superimposed pictures taken 122 μs and 244 μs after the impact of the shock wave. The first picture taken at 122 μs shows the deformation process at an intermediate stage. The side view reveals clearly the plastic hinge. The maximum midpoint deflection at this stage is 8.57 mm. The second superimposed picture shows the deformation at a later stage which is close to the final deformed shape of the specimen. Paint particles lifting of the specimen can be seen in the second picture as well. The

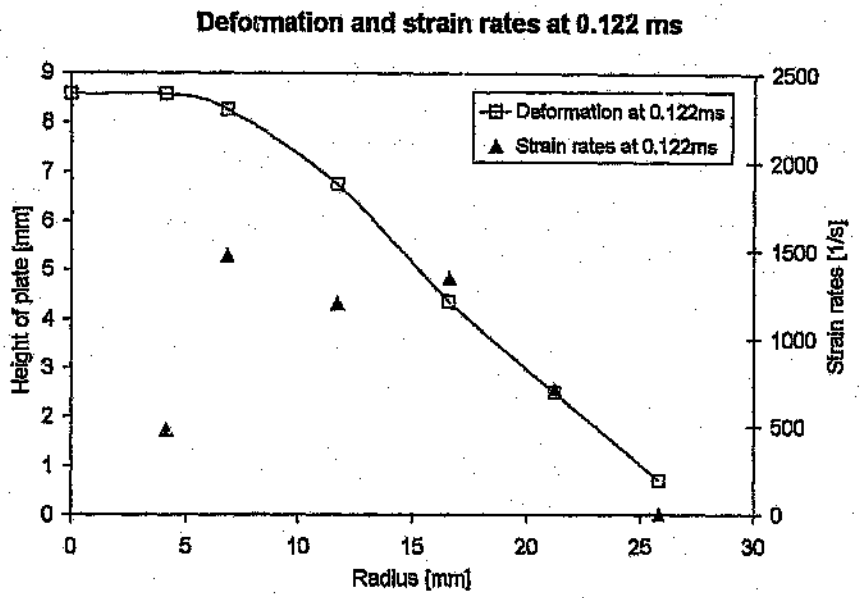

Figure 8.23: Deformation and local strain rates of the copper plate at 122 μs

maximum midpoint deflection in this picture is 12.3 mm. The final deformation of the specimen measured after the test is 12.5 mm. The bottom view (right side) of the photograph shows clearly the movement of the grid. The photograph shows white lines with a brighter middle part. These white lines are the grid lines, which have been drawn onto the specimen with an initial thickness of 2 mm. Since two superimposed pictures have been taken the photograph shows the white grid lines at different positions. The bright middle part is due to an overlapping of the grid lines from the first and the second picture. From the dislocation of the grid the circumferential strain ϵ_θ can be calculated directly by using equation 8.2. The radial displacement is calculated by using the circular displacement and the actual height of the point measured in the side view photograph. The distance between two measured points has been approximated as a straight line. The radial strain can then be calculated by using equation 8.1. The thickness strain cannot be measured and has therefore to be derived from equation 8.4. In order to calculate the strain rates the effective strain is calculated first by using equation 8.9. The results of the strain rates measurements at two different deformation stages are shown in Fig 8.23 and 8.24. The figures show the strain rates and the shape of the specimen at the specific times of 122 μs and 244 μs.

In Fig. 8.23 measurements have been made in the undisturbed centre part, in the

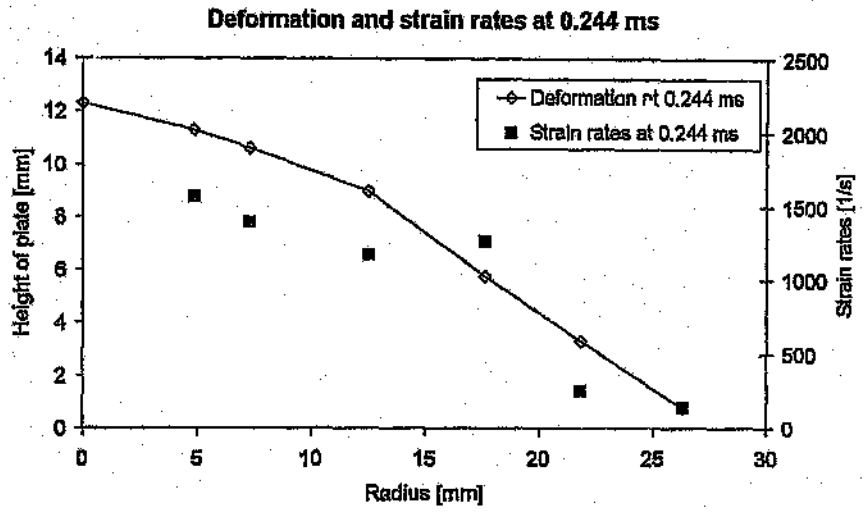

Figure 8.24: Deformation and local strain rates of the copper plate at 244 μs

plastic hinge and outside the plastic hinge. The results show a very low strain rate in the centre part and the maximum strain rate in the plastic hinge. This means that the centre is nearly undisturbed as already assumed in literature (e.g. [11] and [15]) and that the deformation process is driven by the plastic hinge. In Fig. 8.24 the plastic hinge has already reached the centre and folded it forward. The values for the strain rates are rising towards the centre. At the outer part of the t .t specimen the strain rates tend towards zero due to the clamping of the disk.

8.3.4 FINITE ELEMENT MODELING OF THE DEFORMATION PROCESS

The deformation process of flat copper disks has been numerically investigated by using the commercial finite element package AUTODYN 2.66. This program is described in section 7.3. In the finite element model a planar two dimensional liquid shock tube with a length of 0.5 m and an inner height of 56 mm (according to the real shock tube) is considered. The liquid shock wave in the model is generated by simulating the impact of a Delrin piston on the water surface. For the delrin piston and the water section a Lagrange processor has been used.

At the end of the 0.5 m long shock tube the copper specimen is introduced. AUTODYN offers for the modeling of thin structures a special 'shell' processor which has been employed in this case. The equation of state used, describes a rigid, strain

hardening material by defining the yield stress at certain strains. The start point of the plasticity curve is defined by the yield stress at zero strain. The material properties for the copper specimen have been taken from the static tensile tests.

As an example of the results from these numerical calculations the deformation process of a 0.9 mm copper plate is shown in Fig. 8.25 to 8.32. The maximum midpoint deflection of this example is 13.5 mm, which allows comparisons with the experimentally determined deformation process of the 0.9 mm copper plate shown in Fig. 8.16b. To reach this maximum midpoint deflection of 13.5 mm in the numerical model a much stronger liquid shock wave had to be used ($\Delta E \approx$ 50%). This difference between model and reality is most probably due to the model being plane two-dimensional. It was not possible to simulate the problem in an axisymmetric model since cell degeneration occurred on the axis of symmetry. In addition to the model being purely two-dimensional a difference occurs in the contour of the numerical liquid shock wave as already described in section 7.3. The pressure history of the simulated liquid shock wave can be seen in Fig. 8.33.

The comparison between the numerical results and experimental results shows a good qualitative agreement. The first six figures (Fig. 8.25 - 8.30) show velocity plots of the lower part of the water section and the metal specimen. Fig. 8.25 is taken 23 μs after impact of the liquid shock wave. The deformation has already started and the metal is pushed forwards. Since the movement of the metal is restricted at the outer part due to the boundary condition a plastic hinge is formed. This results in the water particles being pushed inwards. The plastic hinge movement towards the centre of the disk can be seen in the following two pictures. The water particles are pushed inwards even more which results in higher water velocities behind the plastic hinge. The centre part of the metal specimen stays a little bit behind the plastic hinge which can be seen in the Fig. 8.26 and 8.27. Fig. 8.27 shows the specimen 123 μs after the impact of the liquid shock wave and can therefore be compared to the second picture in Fig. 8.16b which has been taken 123 μs after impact. The development of the plastic hinge is quite similar. The length of the flat centre part is about 25 mm. in both pictures. The numerical simulation reveals velocity vectors pointing inwards for the outer parts of the metal specimen, which have already been deformed by the plastic hinge. In the following pictures (Fig. 8.28 and 8.29) the plastic hinge reaches the centre. The water particles are still pushed inwards which leads to a maximum velocity in the centre. This results in the centre part being rapidly pushed forwards. The final deformed shape of the specimen can be seen in Fig. 8.30. The metal and the water velocity has dropped to zero.
The deformation velocities of the metal specimen in the centre part are shown in

Fig. 8.34. In the figure it can be seen that the maximum deformation velocity occurs right at the beginning of the deformation. With increasing deformation the velocity drops down. This is in good agreement with the experimental results shown in Fig. 8.16 a and b. These figures show a large velocity drop from the early stage of the deformation and then again a large increase of the velocity when the centre folds forward.

With the liquid shock wave impacting on the metal specimen the deformation commences and the shock wave does not get reflected. Instead an expansion wave is generated which travels up the shock tube. The generation of the expansion wave, which is possible in the numerical model since pure water is assumed, is due to the fact that the deformation velocity of the metal is higher than the velocity of the water particles induced by the piston. The local flow has to accelerate to remain attached to the plate since the deformation velocity for the copper specimen at the beginning of the deformation process is higher than 90 m/s (see Fig. 8.34). The velocities of the water particles behind the shock wave, which are equal to the impact velocity of the projectile, are 60 m/s. In Fig. 8.31 and 8.32 two contour plots are shown 23 μs and 73 μs after the impact of the shock wave. The plots show the generation of the expansion wave. The expansion wave can also be seen in the simulated pressure history in Fig. 8.33. The time duration of the expansion wave is similar to the deformation time of the metal specimen. The pressure history shows the reflection of the expansion wave at the top end of the liquid shock tube, where the Delrin piston is still lying on the water surface. The reflected expansion wave is characterised by the second negative pressure peak and the following pressure increase.

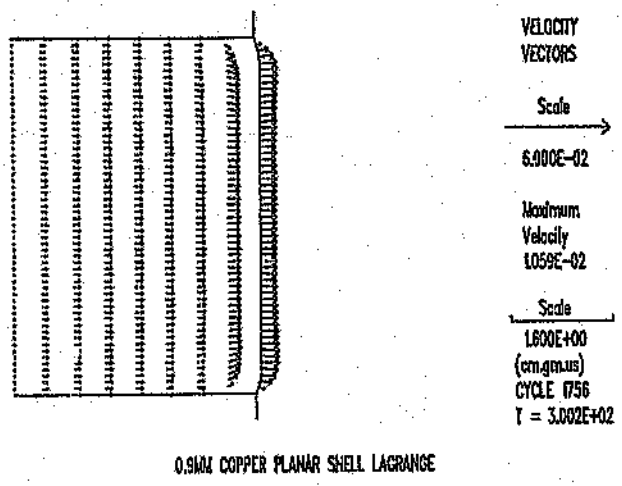

Figure 8.25: AUTODYN 2D-model: Deformation of a 0.9 mm copper plate at 23 μs after impact of liquid shock wave (velocity scale units in $[cm/\mu s]$ and dimension scale units in $[cm]$)

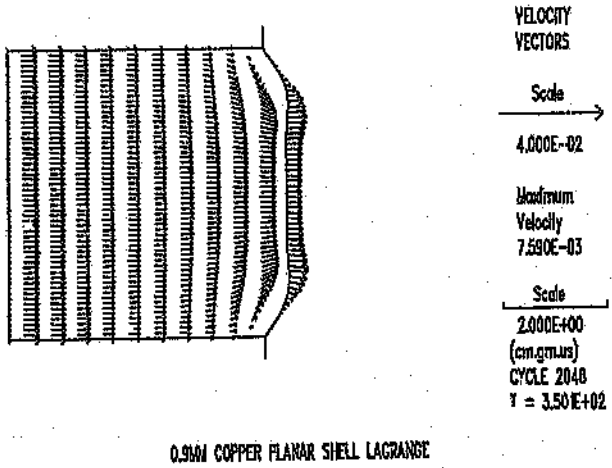

Figure 8.26: AUTODYN 2D-model: Deformation of a 0.9 mm copper plate at 73 μs after impact of liquid shock wave (velocity scale units in $[cm/\mu s]$ and dimension scale units in $[cm]$)

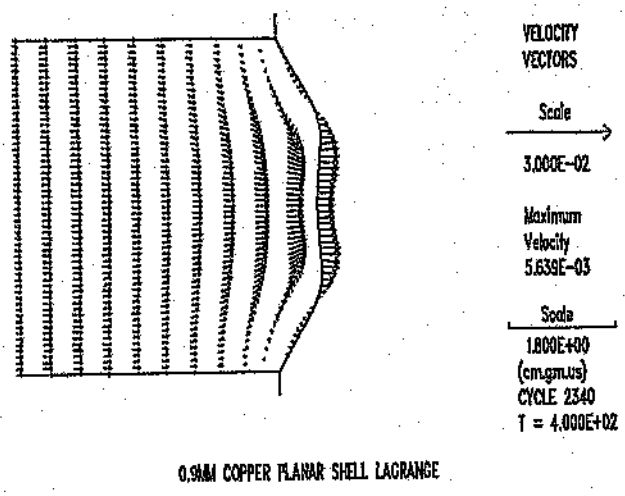

Figure 8.27: AUTODYN 2D-model: Deformation of a 0.9 mm copper plate at 123 μs after impact of liquid shock wave (velocity scale units in $[cm/\mu s]$ and dimension scale units in $[cm]$)

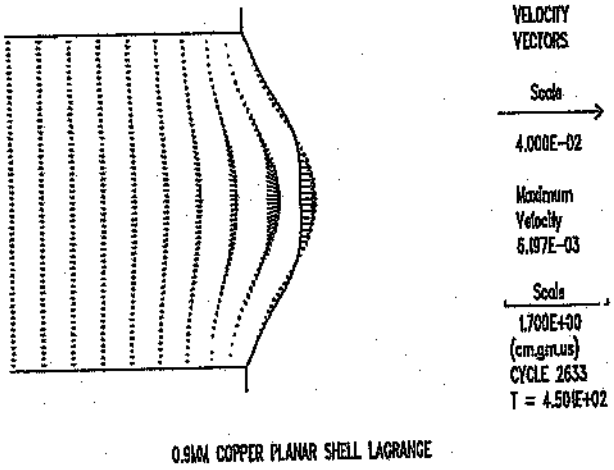

Figure 8.28: AUTODYN 2D-model: Deformation of a 0.9 mm copper plate at 173 μs after impact of liquid shock wave (velocity scale units in $[cm/\mu s]$ and dimension scale units in $[cm]$)

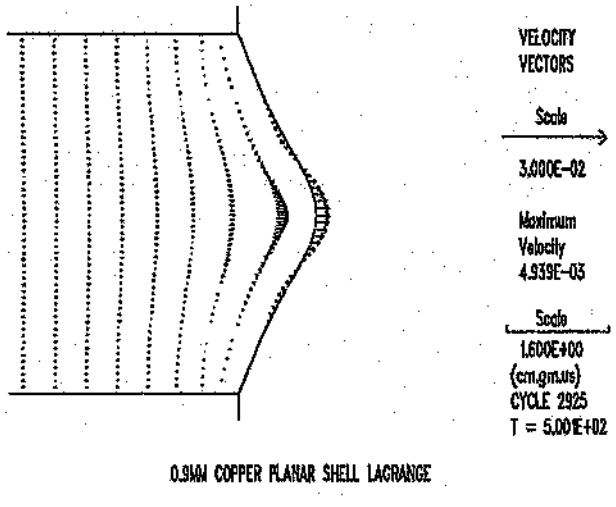

Figure 8.29: AUTODYN 2D-model: Deformation of a 0.9 mm copper plate at 223 μs after impact of liquid shock wave (velocity scale units in $[cm/\mu s]$ and dimension scale units in $[cm]$)

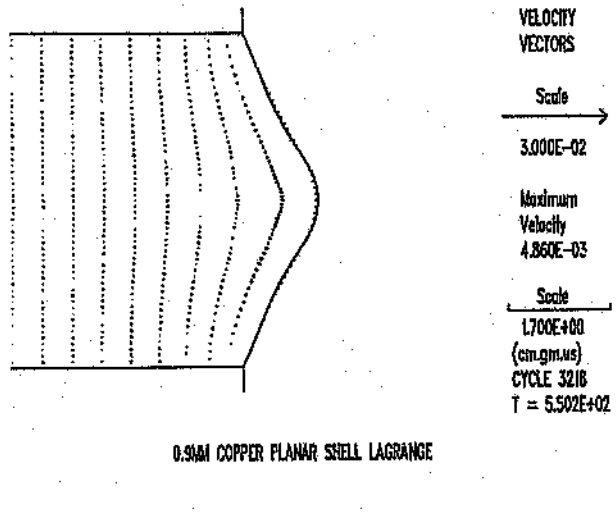

Figure 8.30: AUTODYN2D-model: Deformation of a 0.9 mm copper plate at 273 μs after impact of liquid shock wave (velocity scale units in $[cm/\mu s]$ and dimension scale units in $[cm]$)

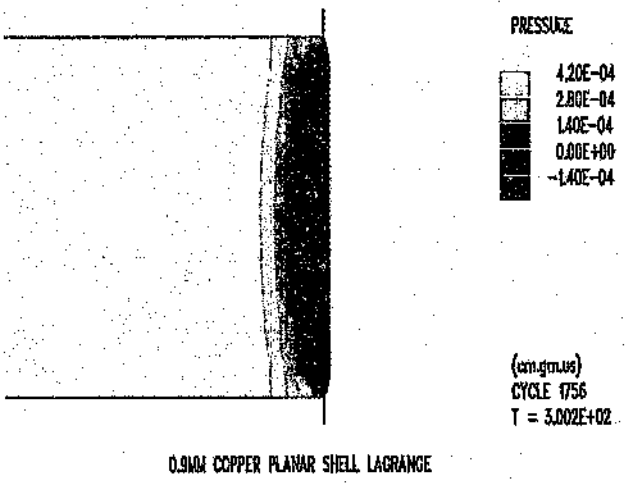

Figure 8.31: AUTODYN 2D-model: Contour plot at 23 μs after impact of liquid shock wave on the specimen (pressure in $[gm/(cm\,\mu s^2)]$)

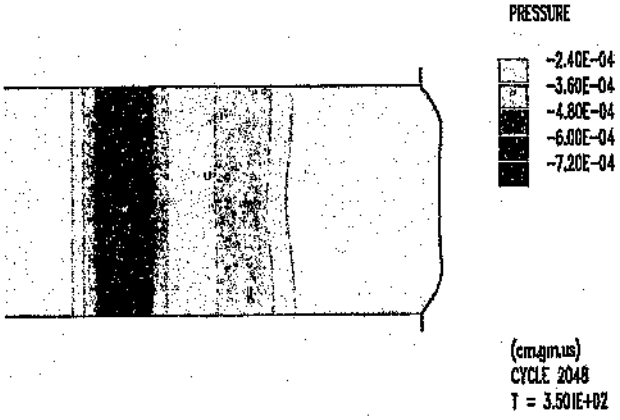

Figure 8.32: AUTODYN 2D-model: Contour plot at 73 μs after impact of liquid shock wave on the specimen (pressure in $[gm/(cm\,\mu s^2)]$)

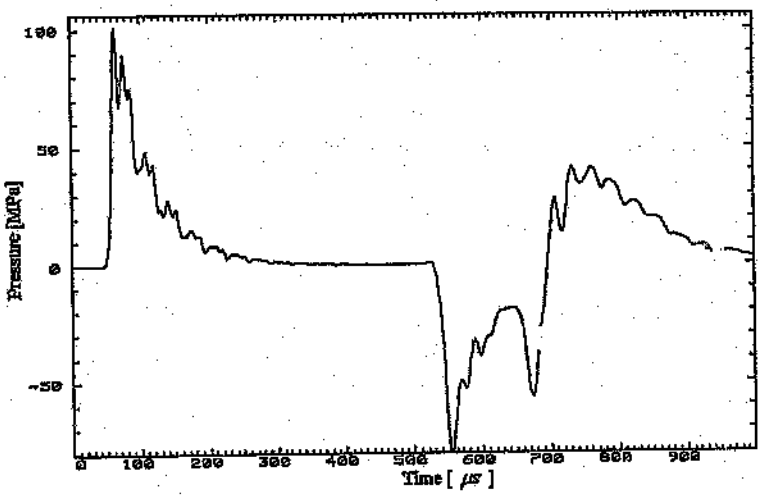

Figure 8.33: AUTODYN 2D-model: Liquid shock wave pressure history

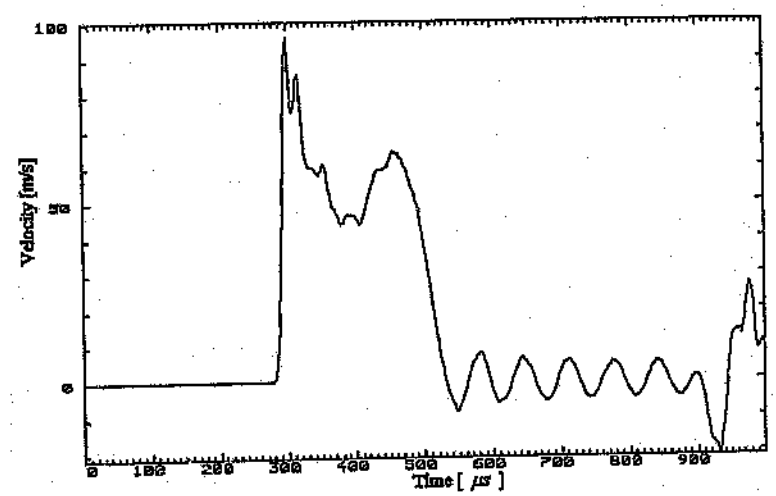

Figure 8.34: AUTODYN 2D-model: Deformation velocity measured in the centre of the 0.9 mm copper plate

9 FORMING OF CYLINDRICAL METAL TUBES

Circular metal tubes out of mild steel and copper are investigated with respect to their deformational behaviour. The stress and strain state of the deformed tube is determined experimentally and the deformation energy is calculated. The deformation process during the impact of the liquid shock wave is optically investigated and the strain rates are calculated. The forming of cylindrical tubes into cylindrical, hexagonal and octagonal dies is examined and the results are presented.

9.1 FOCUSING OF THE LIQUID SHOCK WAVE INTO THE CYLINDRICAL TEST TUBE BY MEANS OF A NOZZLE

For the forming of cylindrical metal tubes the liquid shock wave has to be focused into the inside of the tube by means of a nozzle. The set-up of the test section and the arrangement of the nozzle and the test specimen can be seen in Fig. 4.5. The behaviour of the liquid shock wave passing through the nozzle has been numerically investigated by using a finite element solver implemented by Felthun [38]. This finite element solver uses the Euler equations. The use of the Euler equations, which ignore the effects of viscosity, is acceptable since the length of time over which the shock wave acts is much shorter than the time period over which viscous effects will develop [39]. The finite element solver uses a Taylor-Galerkin algorithm ([40]) which is used in conjunction with a Flux-Corrected-Transport algorithm [41] to maintain high resolution of discontinuities. For refining the mesh appropriately an adaptive refinement algorithm was used [42].

The results of this numerical simulation are shown in Figs. 9.1 - 9.4. The initial shock wave has a maximum pressure of 47 MPa. The elapsed time is taken from

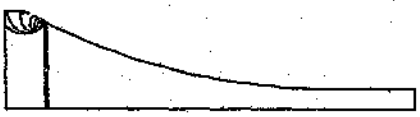

Figure 9.1: Euler model at $t = 4\ \mu s$

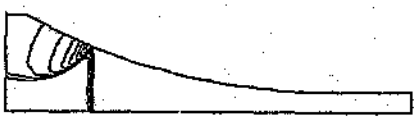

Figure 9.2: Euler model at $t = 12\ \mu s$

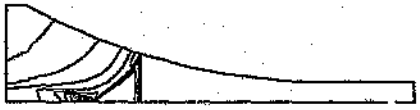

Figure 9.3: Euler model at $t = 20\ \mu s$



Figure 9.4: Euler model at $t = 28\ \mu s$

the first contact of the shock wave with the nozzle. In all cases the shock wave is travelling from the left to the right hand side. Each figure displays the isopycnics (contour lines of equal density). In the figures the liquid shock wave passing through the nozzle is shown. With the impact of the shock wave on the side walls of the nozzle a reflected shock wave is generated (see Fig. 9.1), which has a curvature pointing inwards and is travelling in the same direction as the initial shock wave. Finally the reflected shock wave catches up with the initial shock wave due to the higher speed of sound in the compressed medium (Fig. 9.2 to 9.5). This leads to a magnification of the pressure of the initial shock wave.

A typical experimental pressure diagram for the set-up with nozzle can be seen in Fig. 9.5. A fourth pressure transducer has been introduced immediately under the nozzle. The initial shock wave yields a maximum pressure of 47 MPa and an energy of 607 J. The pressure behind the nozzle has been magnified to 171 MPa. In the CFD calculation the focused shock wave yields a maximum pressure of 215 MPa.

9.2 STRAINS AND STRESSES OF DEFORMED METAL TUBES

Similar to the case of forming of circular plates a grid is painted onto the cylindrical tubes before each test. After the test the deformations are measured by using the Heidenhahn MT 60 electronic gauge for the thickness reduction, a vernier gauge for the radial expansion and the Nikon Profile Projector for measuring the longitudinal deformation. Since the adjustment of the profile projector is vertical to the tube only the vertical displacement can be measured. The actual longitudinal displacement has to be calculated from the vertical displacement and the actual radius of the point. The distance between two points is approximated as a straight line.

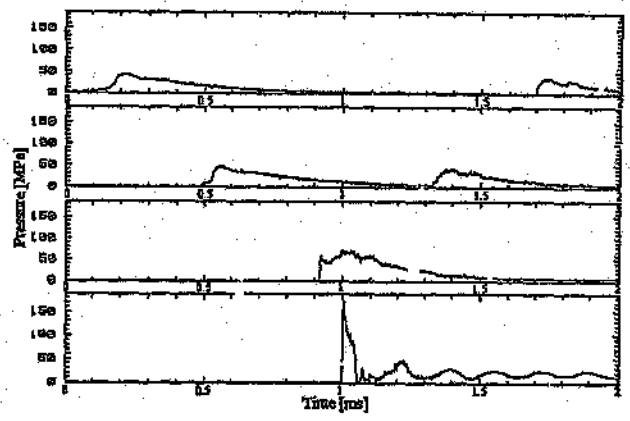

Figure 9.5: Pressure history for an aluminium projectile (0.87 *kg*) with focusing nozzle at the bottom end of the shock tube, Transducer 1, 2, 3 and 4

Due to the greater energy requirement for the deformation of tubes the aluminium piston with a mass of 0.87 *kg* and the steel piston with a mass of 3.665 *kg* were used for the test with the copper tubes and for the tests with the mild steel tubes respectively.

The results of free forming of cylindrical mild steel and copper tubes tubes can be seen in Figs. 9.6 and 9.7 respectively. The figures show that, after an initial deformation over the whole length of the tube (see e.g. Fig. 9.7, first tube), the deformation at the top part lags behind the deformation of the bottom part. This leads to a final shape of the tubes which is more bulged towards the bottom. With increasing deformation the maximum diameter starts to move towards the centre. This can also be seen in Fig. 9.8 and 9.9. The diagrams display the change of diameter of the deformed tubes and show the energy and maximum pressure of the shock wave. The phenomenon of the maximum deformation, being closer towards the bottom, can be explained with the shock wave travelling from the top of the tube to the bottom. At the end wall the shock wave gets reflected, which results in double the pressure at the bottom of the test specimen. Since the tube is restrained at the top and the bottom by means of the free forming die, the tube cannot expand freely. This results in the maximum diameter moving with increasing pressure energy from the bottom of the tube towards the centre.

The three natural strains, the hoop, the longitudinal and the thickness strain, can be calculated by using the measured deformations and the following three equations.



Figure 9.6: Pictures of deformed mild steel tubes. Maximum diameter increases from left to right hand side [mm]:24.1, 26.0, *torn*



Figure 9.7: Pictures of deformed copper tubes. Maximum diameter increases from left to right hand side [mm]:21.4, 24.7, 25.2, 25.4, 26.35, 26.6, *torn*

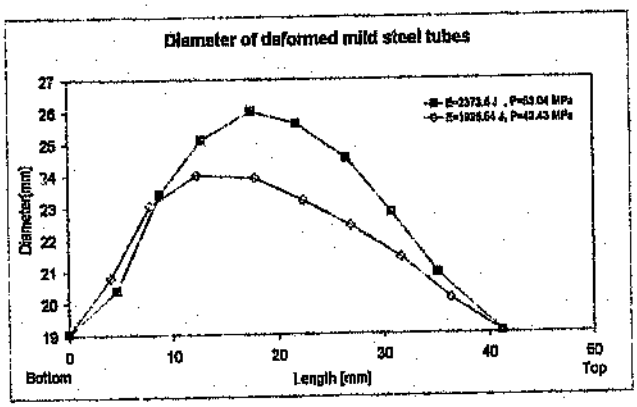

Figure 9.8: Change of diameter versus length of deformed mild steel tubes

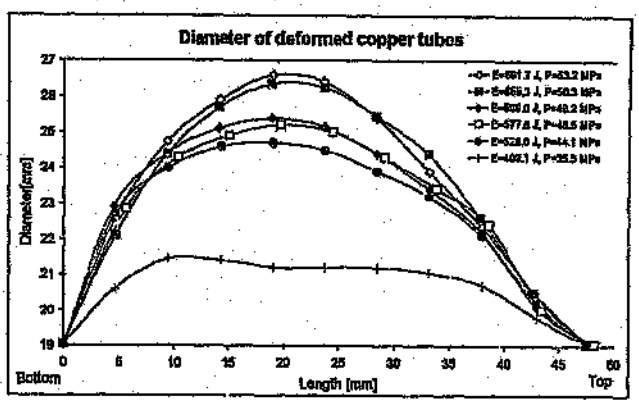

Figure 9.9: Change of diameter versus length of deformed copper tubes

Hoop strain:

$$\epsilon_h = ln\frac{R}{R_0} \tag{9.1}$$

Longitudinal strain:

$$\epsilon_L = ln\frac{L}{L_0} \tag{9.2}$$

Thickness strain:

$$\epsilon_t = ln\frac{T}{T_0} \tag{9.3}$$

The strain conditions for the deformed test specimen are found to be close to plane strain (Plane strain: $\epsilon_L = 0$ and $\epsilon_h = \epsilon_t$) since the longitudinal deformations are very small. Wilson [12] reported the natural strains to have a combined stress condition between plane strain and simple tension but more closer to plane strain with an exponent factor approximating -0.9. The thickness reduction is then given by:

$$t = t_0 e^{-0.9\epsilon_h} \tag{9.4}$$

In Fig. 9.10 the natural strains versus the length of a copper tube are shown as a typical example. It can be seen that the behaviour of the natural strains is close to plane strain. The longitudinal strains have approximately -0.1 to -0.2 times the value of the hoop strains, which is in good agreement with equation 9.4. The natural strain variation is also in accordance with the constancy of volume law (see equation 8.4).

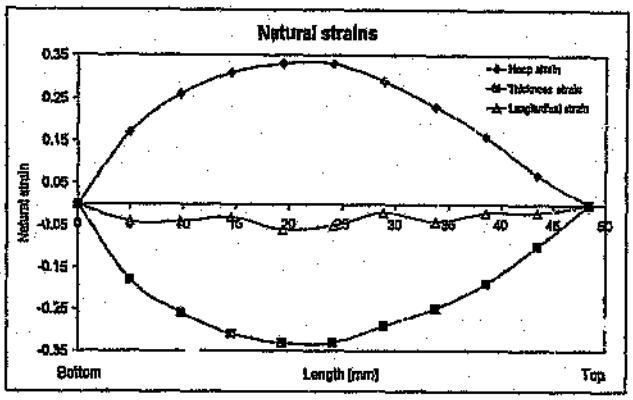

Figure 9.10: Variation of natural strains for a copper tube with a wall thickness of 1.4 mm after impact of the liquid shock wave with $p_{max} = 53.2\ MPa$, $E = 691.7\ J$, $I = 37.6\ Ns$

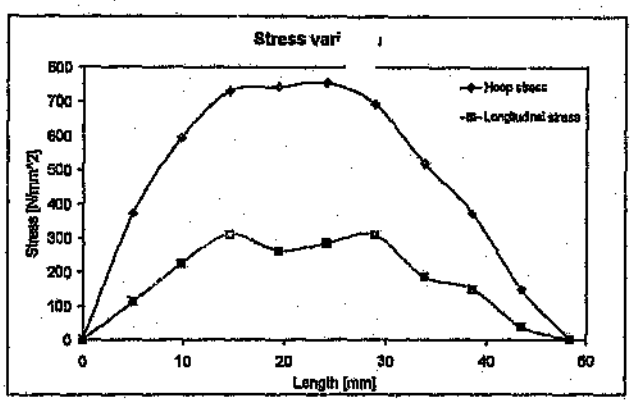

Figure 9.11: Variation of stresses for a copper tube with a wall thickness of $1.4mm$ after impact of a liquid shock wave with $p_{max} = 53.2MPa$, $E = 691.7J$, $I = 37.6Ns$

For the calculation of the stress state in a deformed cylindrical tube the Levy - Mises plastic stress strain relationship is used (see equations 8.5). The tube specimen can be regarded as thin walled and therefore the thickness stress can be neglected. In Fig. 9.11 the stress state of the same deformed copper tube can be seen as a typical example. The diagram shows that the longitudinal stress is a little bit smaller than half the hoop stress. For a plane strain condition the longitudinal stress would be exactly half the hoop stress ($\sigma_L = 0.5\ \sigma_h$) but since the stress condition is between simple tension and plane strain, σ_L is smaller.

9.2.1 DEFORMATION ENERGY FOR CYLINDRICAL TUBES

The equation for the deformation energy has been derived in section 6.3. By using the strain distribution of the deformed cylindrical tubes, which has been determined in section 9.2, the total deformation energy of the tubes can be calculated. The grid, which has been painted onto the specimen before the test, divides the free formed section into nine equal parts along the longitudinal axis. The calculation is therefore split into nine parts as well.

$$W = \sum_{i=1}^{9} \left(\frac{K}{n+1} \right) (\bar{\varepsilon})_i^{n+1} V_i \tag{9.5}$$

For the calculation of the effective strain equation 8.9 has been used. The volume of the nine sections of the test specimen are integrated by assuming a circular ring element with constant thickness and constant strain.

$$dV = 2\pi T \frac{D}{2} dx$$

$$V = \pi T \int_{D1}^{D2} \sqrt{\frac{1}{4} + \left(\frac{L2 - L1}{D2 - D1} \right)^2} D \, dD$$

$$V_i = \frac{1}{2} \pi T_i \sqrt{\frac{1}{4} + \left(\frac{L_{i+1} - L_i}{D_{i+1} - D_i} \right)^2} \left(\mid D_{i+1}^2 - D_i^2 \mid \right)$$

The results of the deformation energy calculation for 1.4 mm copper tubes and 1.6 mm mild steel tubes can be seen in Table 9.1. The table shows the maximum deformation of the tubes, the calculated deformation energy and the energy of the initial shock wave. The difference between the energy of the initial shock wave and the deformation energy is quite large which is due to the shock wave focused through the nozzle into the tube. A major part of the shock wave gets reflected at the nozzle and is not passing through it(see the reflected shock wave in Fig. 9.5). Therefore only a small portion of the total amount of energy can be utilised in the deformation process.

9.3 OPTICAL INVESTIGATION OF THE DEFORMATION PROCESS

The shadow photography system described in section 4.3 has been used for the optical investigations. In comparison to the optical investigations of circular disks

Maximum Deformation [mm]	Deformation Energy [J]	Shock Wave Energy [J]
Copper tubes:		
21.2	105.42	409.1
24.7	237.23	526.0
25.2	278.05	577.6
25.4	280.14	589.0
25.8	295.73	607.0
26.35	298.95	655.3
26.6	298.03	691.7
Mild steel tubes:		
23.95	306.52	1995.54
26.0	422.3	2373.62

Table 9.1: Deformation energy for cylindrical copper and mild steel tubes

(see section 8.3) no special test specimen were needed since the cylindrical tubes are restrained only at the top and bottom by the free forming die. The deforming part of the tube is therefore not covered (see Fig. 4.6). Good results have been obtained for a camera setting of three superimposed pictures with an exposure time of 11 μs. For the optical tests copper tubes with a wall thickness of 1.4 mm have been used. No optical test have been performed with mild steel tubes since very high pressures have to be used for the deformation of the steel tubes. In case of tearing of the tubes this high pressure would discharge into the test section and could result in breaking of the test windows.

9.3.1 DEFLECTION TIME HISTORY

Two typical results of the optical investigations of cylindrical tubes can be seen in Fig. 9.12 a) and b). To magnify the deformation process in the picture an aspect ratio of 2:1 was chosen which leads to the oval shape of the test section window. The white line indicates the undisturbed specimen. The first photograph (Fig. 9.12a) shows an early stage of the deformation process. The three superimposed pictures have been taken 35 μs, 126 μs and 217 μs after the shock wave has arrived at the centre part of the tube. The pictures show that the deformation starts at the top of the tube and that the bottom first remains undisturbed. For the second photograph a larger delay has been chosen to visualise the final deformation process. The three superimposed pictures have been taken 271 μs, 512 μs and 753 μs after the arrival

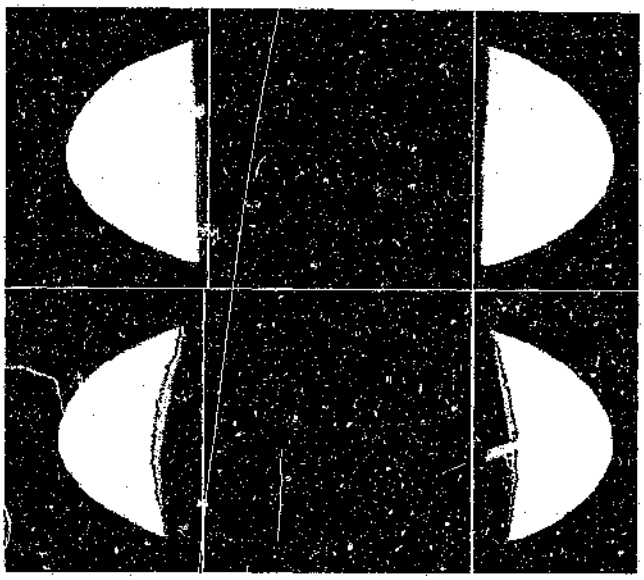

Figure 9.12: Pictures of the deformation process of copper tubes a.) $p = 58.3\ MPa$, $I = 35.6\ Ns$, $E = 683.4\ J$ b.) $p = 42.8\ MPa$, $I = 31.6\ Ns$, $E = 509.5\ J$

of the shock wave. In the first superimposed picture the deformation at the bottom part is already nearly equal to the deformation of the top part. In the second picture it can be seen that the deformation at the top has slowed down. The deformation of the centre part of the tube stays behind the deformation of the bottom and only in the third picture it can be seen that the point of maximum deformation is moving towards the centre of the tube. In this test the whole deformation process stopped before the maximum deflection reached the centre of the tube. Therefore the final shape of the tube shows a larger deformation towards the bottom part.

This unsymmetrical behaviour of the test specimen can also be seen in the deformation velocities, which were calculated for three different deformation stages and at three different points of the tube. Similar to the calculation of the deformation velocities for circular disks in section 8.3.1 the velocities for the tubes have been calculated by measuring the difference in the position of the specimen for each picture. The time duration between each picture was obtained from the camera setting (271 μs for the first and 241 μs for the last two pictures). The deformation velocities have been determined at the top (15 mm above centre), at the centre and at the bottom part (15 mm below centre) of the tube. The results are shown in Fig. 9.13 and it can be seen that the deformation velocities for the top part are lower than for the bottom part which leads to the unsymmetrical deformation of the tube.

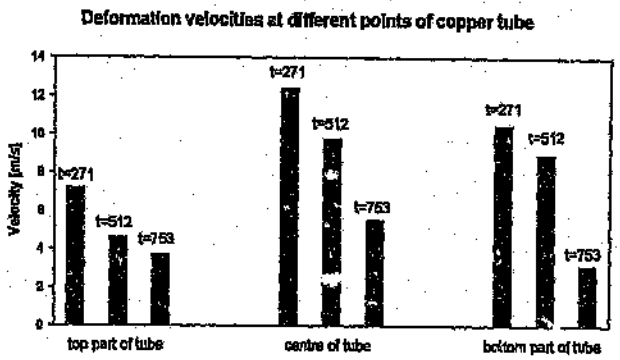

Figure 9.13: Deformation velocity at different points of the tube

The deformation velocity at the bottom decreases drastically towards the end of the deformation process (see Fig. 9.13 at 753 μs) since the movement of the metal is restricted due to the free forming die.

The average deformation velocity measured at the centre of the tube is much slower in comparison to the deformation velocity of circular plates. For the test in Fig. 9.12b the mean velocity of the moving metal in the centre of the specimen was 9.34 m/s.

9.3.2 STRAIN RATES

The strain rates in this section are determined by using the effective strains calculated with Eqs. 8.9 and 8.16. The deformation times are obtained from the experiments performed with the high speed video camera. Therefore only strain rates for the copper tubes have been obtained since no optical tests for the mild steel tubes have been performed. The deformation of the tubes was measured at the centre of the tube. As already mentioned in section 8.3.2 the average deformation speed has to be considered because the pictures do not automatically show the maximum deformation of the test specimen. The time difference between the largest deformation on the picture and the maximum deformation measured after the test is calculated using the average deformation velocity. In Fig. 9.14 the strain rates versus the shock wave energy are shown. The points show a nearly linear behaviour in this range of strain rates. In comparison to the strain rates for the forming of flat plates the strain rates of the cylindrical tubes are lower, which is due to the lower deformation velocity. The strain rates for the tubes lie in a range

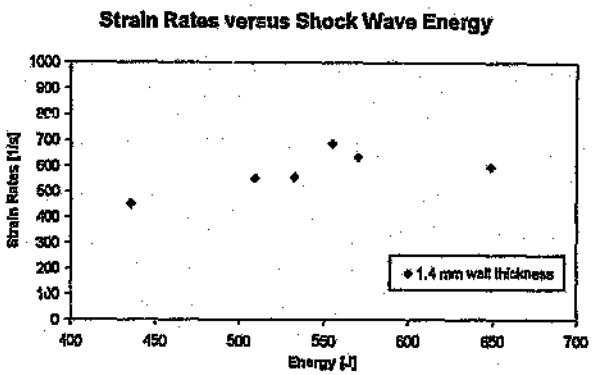

Figure 9.14: Strain rater versus liquid shock wave energy, cylindrical tubes

from $0.4 \cdot 10^3 - 0.7 \cdot 10^3\ s^{-1}$ whilst the strain rates for the disks lie in a range from $0.2 \cdot 10^3 - 3 \cdot 10^3\ s^{-1}$.

9.4 FORMING OF CYLINDRICAL TUBES INTO DIES

Mild steel tubes with a wall thickness of 1.6 *mm* and 1.24 *mm* have been deformed into cylindrical dies. Five dies with a diameter of 22 *mm*, 23 *mm*, 24 *mm*, 25 *mm* and 27 *mm* were available and have been tested. A schematic drawing of a $\emptyset$ 22 *mm* die can be seen in Fig 9.15. The maximum elongation $\Delta D/D_0$ for a tube which has been fully deformed into the die covers a range of 15.48% for the $\emptyset$ 22 *mm* die up to 41.73% for the $\emptyset$ 27 *mm* die. The heavy steel projectile (3.665 *kg*) has been used for the experiments. The results are shown in the Tables 9.2 and 9.3 for the 1.6 *mm* and 1.24 *mm* tubes respectively. The tables show the maximum pressure, the energy and the impulse of the initial liquid shock wave and the filling grade of the die. The filling grade distinguishes between five different deformation stages of the tube which are:

1. tube not touching the wall of the die
2. tube touches wall of the die over a certain length (max. 30 *mm* see Fig. 9.15)
3. die filled except corners
4. die completely filled
5. torn

	Shock wave pressure $[MPa]$	Shock wave energy $[J]$	Shock wave impulse $[Ns]$	Filling grade
$22mm$ die	65.65	3202.62	122.5	4
	45.25	1824.8	98.97	3
$23mm$ die	60.4	3496.6	136.52	4
$24mm$ die	66.4	3113.23	122.2	4
	60.2	2762.2	114.3	4
$25mm$ die	57.04	2483.6	107.6	2 ($15.0mm$)
	58.6	2482.5	110.0	2 ($20.4mm$)
	69.04	2728.4	114.3	4
	57.3	2649.3	114.5	3
$27mm$ die	43.4	1996.0	102.0	1
	53.1	2374.0	114.0	1
	50.46	2586.3	123.8	5

Table 9.2: Filling grade and energy requirements for forming of mild steel tubes ($1.6\ mm$) into cylindrical dies

	Shock wave pressure $[MPa]$	Shock wave energy $[J]$	Shock wave impulse $[Ns]$	Filling grade
$22mm$ die	58.2	2516.9	111.93	4
$23mm$ die	52.2	2434.43	114.9	4
$24mm$ die	61.78	3300.8	128.3	4
$25mm$ die	58.08	2620.4	111.8	5
	45.1	1428.2	85.7	4
$27mm$ die	52.88	2374.2	110.98	5
	34.5	1241.85	83.53	5

Table 9.3: Filling grade and energy requirements for forming of mild steel tubes ($1.24\ mm$) into cylindrical dies

The results show that in comparison to free forming much more energy is needed to fill the dies completely (see Figs. 9.8 and 9.9). Despite this high pressure energy the tubes do not tear since the movement of the metal is restricted due to the die walls.

The $\emptyset$ 27 mm die could not be filled since the diameter of this die exceeds the maximum possible elongation of the mild steel tubes. In this case significantly less energy is needed to tear the tubes. A photograph of a tube deformed into the $\emptyset$ 24 mm die can be seen in Fig. 9.16.

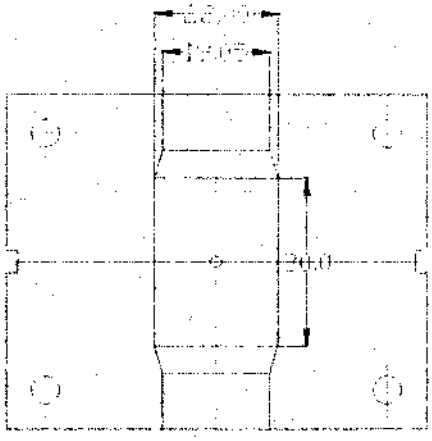

Figure 9.15: Schematic drawing of cylindrical die for tube forming

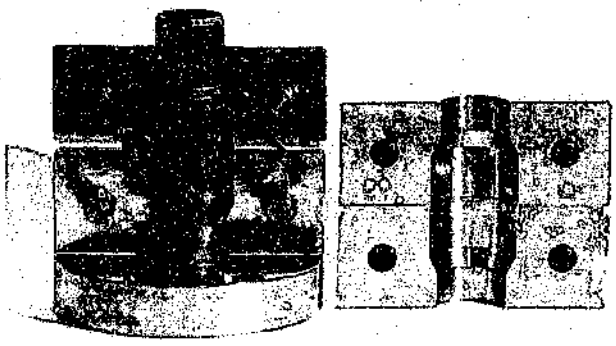

Figure 9.16: $\emptyset\, 24mm$ cylindrical die with a deformed mild steel tube, 1.6 mm wall thickness after impact of a shock wave with $P_{max} = 66.4\ MPa$, $I = 122.2\ Ns$, $E = 3113.23\ J$

Experiments have been performed to transform a cylindrical tube into a hexagonal or octagonal tube by deforming it into a die of this shape. The hexagonal die has a diagonal length of 22.5 mm and the octagonal die 22.8 mm. A schematic drawing of the octagonal die can be seen in Fig. 9.17. The experiments have been carried out with copper tubes of 1.2 mm wall thickness. A photograph of a cylindrical copper tube, which was deformed into a hexagonal die, is shown in Fig. 9.18. The picture shows the deformed copper tube next to the die and it can be seen that the transformation of a cylindrical into a hexagonal tube was possible. The small round imprint on the tube results from the vacuum line hole in the die.

The results of the experiments performed with these two dies can be seen in the Tables 9.4 and 9.5. The tables show the maximum pressure, the energy and the impulse of the initial liquid shock wave. The filling grade of the die was determined by measuring the diagonal length of the deformed tube. For the experiments the aluminium (0.87 kg) and the steel (3.665 kg) projectile have been used. The results in the tables show an interesting phenomenon. The maximum diagonal length of the deformed tubes was produced with the lighter aluminium projectile despite the highest amount of pressure energy was generated in the experiment with the steel projectile. A reason for this is most probably the time duration in which the pressure energy is delivered to the test specimen. The duration of the liquid shock wave generated by the aluminium projectile is much shorter than for the steel projectile. Therefore the power of the liquid shock wave generated by the aluminium projectile is higher than for the steel projectile.

Projectile	Shock wave pressure $[MPa]$	Shock wave energy $[J]$	Shock wave impulse $[Ns]$	Diagonal length $[mm]$
Al [0.87kg]	53.8	699.7	36.1	21.86
Al [0.87kg]	49.0	688.0	34.9	22.15
Al [0.87kg]	62.12	902.4	40.4	22.25
Al [0.87kg]	74.1	1505.92	55.79	22.32
Steel [3.665kg]	44.3	1769.9	92.15	21.8

Table 9.4: Filling grade and energy requirements for forming of copper tubes (1.2 mm) into the hexagonal die

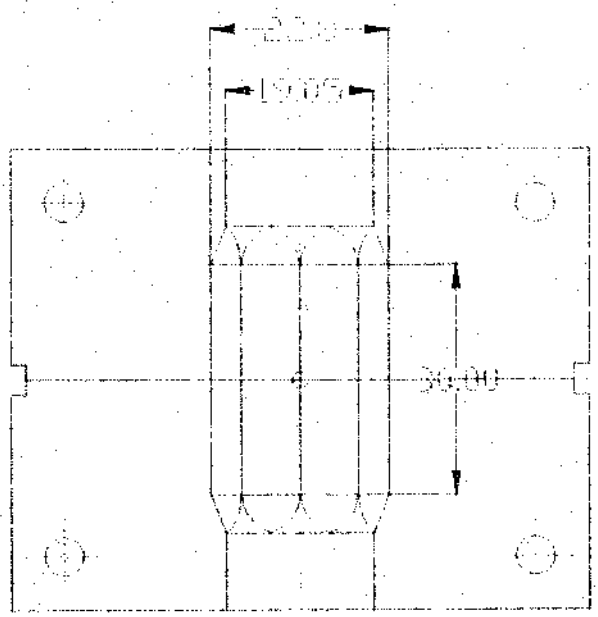

Figure 9.17: Schematic drawing of the octagonal die for tube forming

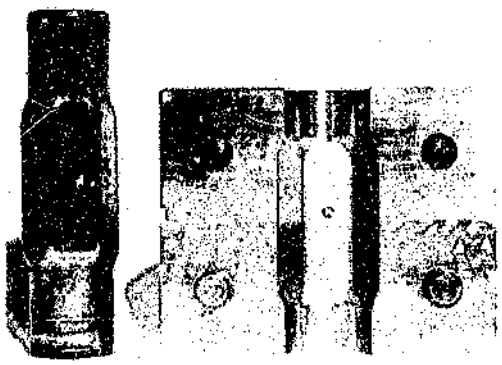

Figure 9.18: Hexagonal die with a deformed copper tube. 1.2 mm wall thickness after impact of a liquid shock wave with $P_{max} = 62.12\ MPa$, $I = 40.3\ Ns$, $E = 902.4\ J$

Projectile	Shock wave pressure $[MPa]$	Shock wave energy $[J]$	Shock wave impulse $[Ns]$	Diagonal length $[mm]$
Al $[0.87kg]$	59.2	828.0	39.1	22.5
Al $[0.87kg]$	57.36	963.03	40.1	22.7
Steel $[3.665kg]$	47.0	1971.8	98.56	22.5

Table 9.5: Filling grade and energy requirements for forming of copper tubes (1.2 mm) into the octagonal die

10 CONVERSION OF THE SHOCK TUBE TO DIAPHRAGMLESS OPERATION

To operate the liquid shock tube two diaphragms have to be fitted before each test. The first diaphragm separates the high pressure driver from the driven section and the second diaphragm covers the water section (see section 4.1.3). The changing of the diaphragms is very time consuming and fragments of the ruptured diaphragms get into the driven and water section and have to be removed. To reduce the time between two tests, to get greater repeatability and to make the liquid shock tube suitable for industrial manufacturing purposes the design of the existing liquid shock tube has been changed.

10.1 THE DIAPHRAGMLESS WATER SECTION

The evacuated driven section and the water section are separated by means of a plastic diaphragm. The purpose of this diaphragm is to keep the water surface smooth and to prevent the water from boiling.

Tests in the projectile mode have been performed with a vacuum close to the evaporating pressure of water and without a diaphragm to cover the water section. These tests reveal that micro bubbles have been generated in the water due to the evaporation. These bubbles absorb parts of the liquid pressure energy. That means that the pressure and the energy of the liquid shock wave decrease rapidly with increasing travel distance of the shock wave. Therefore the vacuum containing driven section had to be changed in order to make the diaphragm unnecessary.
An interim piece has been designed, which contains two longitudinal slots opposite to each other. The interim piece is situated between the driven and the water section. The water in the water section is filled up to the bottom of the slots. The driven section is no longer evacuated since the downwards moving projectile is able to push the air through the slots out of the tube. This additional work results in

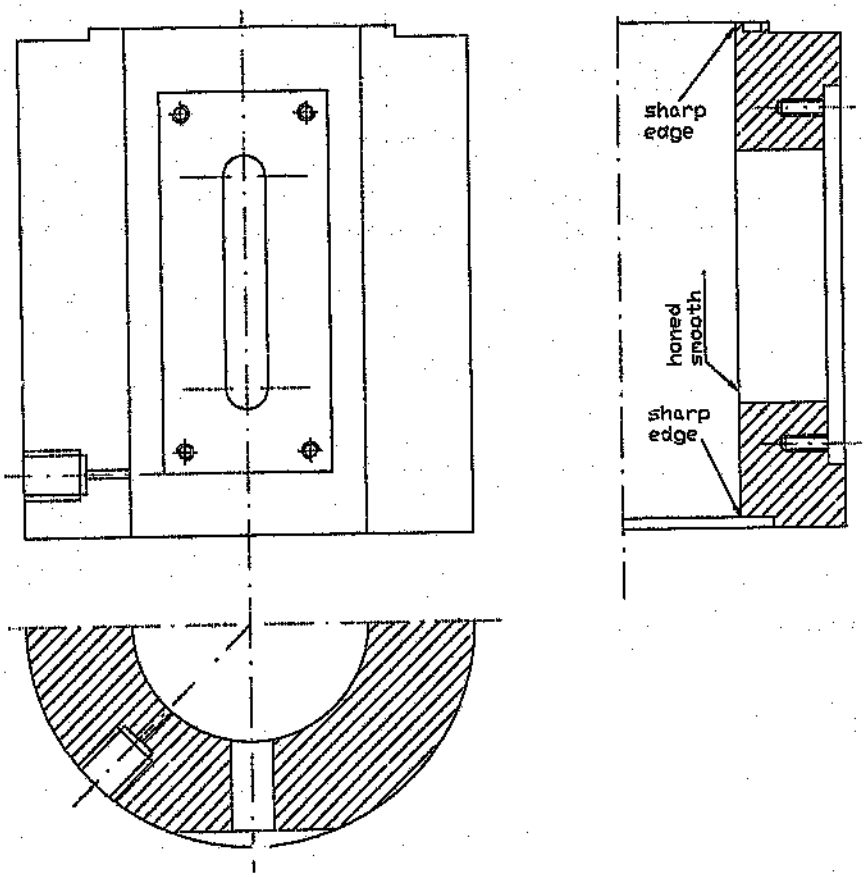

Figure 10.1: Schematic drawing of slotted interim section

energy loss of the projectile. This disadvantage is not significant since more than enough pressure energy is available (see section 4.1).

After the test the two slots are closed by means of two plates. The projectile can now be pushed back into the initial position by introducing high pressure into the interim section. The design of the interim section can be seen in Fig. 10.1.

10.2 THE DIAPHRAGMLESS DRIVER

To improve the performance of the liquid shock tube the diaphragm which separates the high pressure vessel from the driven section had to be replaced. This was done by means of a diaphragmless driver. It was the objective to design a new concept

for a diaphragmless driver that is able to work on gas shock tubes as well as on the liquid shock tube. For the projectile mode of the liquid shock tube the opening time of the new driver is not too important since the projectile velocity is much slower than the speed of sound. To generate shock waves in gases the opening time is very important. The optimum would be an instantaneous opening of the driver (which cannot be fulfilled) to minimize the establishment time of the shock wave. With increasing opening time the shock needs longer time to establish. If the opening of the driver is too slow the shock cannot establish at all and only a compression wave is generated. To specify the performance of a driver the distance is measured that the shock has to travel to fully establish. This is done in the literature, by quoting the non-dimensional shock formation length L/D. To determine if the shock is fully established the Mach Number and/or the rise time of the shock has to be recorded. An established shock is defined by a constant Mach Number and by a short rise time.

To determine the performance of the new driver the tests have been performed with a shock tube set-up for gas shock waves (see section 4.1.1)

10.2.1 PREVIOUS WORK

In conventional shock tubes the high-pressure gas is separated from the low pressure gas by a metal or plastic diaphragm. The advantages of using a diaphragm are the simplicity of design of such systems and the fact that a diaphragm ruptures very rapidly to produce a shock wave in short distances. The disadvantages are numerous: The ruptured fragments of the diaphragm can contaminate and even damage the shock tube. The presence of diaphragm fragments during a test and the varying nature of each diaphragm rupture cause a lack of experimental reproducibility in Mach number. The replacement of diaphragms can be costly, time consuming and can lead to test gases diffusing into the laboratory.

Over the last 30 years numerous researchers have used different piston and rubber valve systems to replace the diaphragm. Garen et al. [43] replaced the diaphragm with a rubber disk, to generate weak shock waves. This disk was pressurised and thus bulged to seal the low-pressure part of the tube from the high-pressure driver. When the pressure behind the disk was vented the shock wave was initiated. The shock tubes used were 97 and 133 pipe diameters long. Oguchi et al. [47] used a snap-action valve consisting of two pistons. The main piston sealed the high-pressure driver gas from the low pressure driven gas. A smaller auxiliary piston actuated the main piston via a system of pressure venting. Pressure readings at 80 pipe diameters

indicated that the Mach 4.1 shock wave was established. Onoder [44] improved on the design of Oguchi et al. [47] by combining the auxiliary and main piston into a more complex single composite piston. The large front end of this piston sealed the driver from the driven section of the shock tube, and was connected to the much smaller back end of the piston by a stem. The volume behind the rear of the piston was extremely small so that the high-pressure gas, preventing the motion of the piston, could be rapidly dumped by a solenoid valve in order to initiate a test. The volume surrounding the piston stem was evacuated to provide less resistance to the piston acceleration. Although this composite piston arrangement resulted in a complex sealing arrangement a. 1 a heavy (1 kg) piston, the acceleration of the piston to the desired stroke length was achieved quickly, due to the small volume behind the piston. The non-dimensional shock formation length L/D (formation length/shock tube diameter) was 65 for a Mach 1.2 shock wave. Yang et al. [45] used the rubber sheet method to obtain low shock formation lengths in the Mach 1.02 to 1.55 range. This is achieved as the rubber has very low mass and its elasticity aids the rapid opening of the driven section. In order to eliminate the expansion wave emanating from the rapid movement of the rubber sheet into its smaller un-deformed area, a system of support blocks and grids were utilised to limit the displacement of the rubber sheet. Smooth post shock pressure traces were obtained with a non-dimensional shock formation length of 40 for Mach 1.2 shock waves. The design was limited to a maximum Mach 1.55 shock wave as the pressure difference across the rubber sheet had to be maintained below one atmosphere, due to limitations in the material properties of the rubber used. Itabashi et al. [46] designed one of the most sophisticated single piston valve systems to date for reproducible operation in the Mach 1.2 to 5 range. In most diaphragmless shock tube designs the driver efficiency is lower than that predicted by simple shock tube theory that assumes an instantaneous diaphragm rupture. The ratio of driver to driven section pressures (p_4/p_1) has to be higher for a given shock strength since the driver gas has to negotiate 90 or 180 degree bends. Itabashi et al. [46] numerically optimised the channel within which the high pressure gas flows to the driven section, thus resulting in a more efficient driver than that of most previous designs. The single piston was accelerated by venting the chamber behind it by rupturing an auxiliary diaphragm. This motion was assisted with a spring mechanism. In order to prevent piston spring back and to increase piston survivability a spring and gas dynamic damper was utilised. The shock formation length for a Mach 1.2 shock wave was about 50 tube diameters.

In order to obtain strong shock waves or to drive a shock into a shock tube at ambient conditions a piston system must be used. In all previous piston actuated drivers, the piston resists the driver pressure and is held in place by a high pressure

behind it. To accelerate conventional piston systems sufficiently rapidly to achieve short shock formation lengths two objectives have to be realised: Firstly the gas pressure behind the piston had to be reduced rapidly to expose the piston to a large differential pressure driving force. Secondly the gas has to be displaced from the auxiliary chamber behind the piston to allow the piston to move the required stroke distance to fully open the valve and prevent choking of the shock tube. Normally to prevent the overly complex design of the dual piston system, a diaphragm is used to vent the auxiliary chamber rapidly. Although shock strength reproducibility and prevention of shock tube contamination (with diaphragm fragments) are achieved using this method, the inconvenience of diaphragm replacement after every test is still present.

In the design presented below there is no auxiliary pressure chamber behind the single piston. Instead the chamber behind the piston is evacuated to provide no resistance at all to piston acceleration. Thus the piston is always exposed to the full driver pressure and the problems of auxiliary chamber gas displacement are not present. Instead the piston is held in place by the friction force exerted on the side of the piston by a steel brake pad mechanism. In order to provide sufficient force to the side of the piston the brake pad is held in place by a small pressurised hydraulic reservoir. When a valve in the hydraulic reservoir is opened the pressure drops almost instantly (since the hydraulic fluid is practically incompressible). Only a very small volume of fluid has to be vented as the brake pad needs only to move fractionally for the friction force to drop to zero. Thus the piston is accelerated rapidly against zero resistance. Due to the simplicity of the design the manufacturing cost of the driver is low and the piston design can easily be optimised to reduce the mass and the shock wave formation length further.

10.2.2 DESIGN

The high-pressure driver gas reservoir is an annular cylinder wrapped around the driven section. The driven section of the shock tube has a diameter of 56 mm and the ratio of driver section to driven section cross-sectional areas is 1.65.

The diaphragmless shock tube driver is an independent unit placed on the top of the shock tube. It consists of a piston chamber, a vacuum chamber, a piston and a hydraulic cylinder. The piston seals the high-pressure vessel from the driven section of the shock tube. The driver is connected to the high pressure vessel and to the shock tube by means of an adapter system. Two o-rings are incorporated into the adapter system to prevent leakage from the pressure vessel into the shock tube or

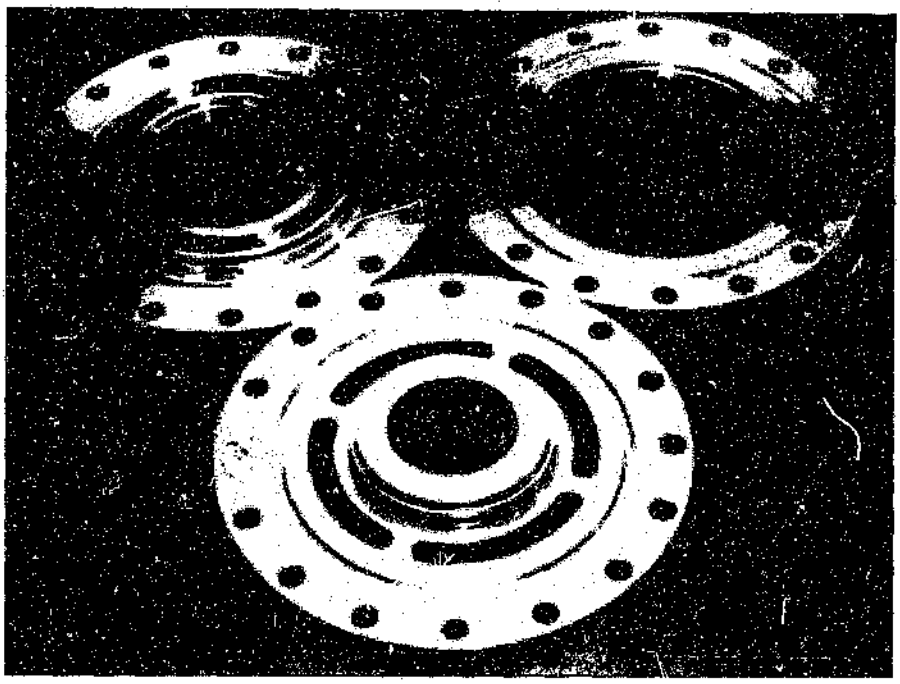

Figure 10.2: Three adapter rings

into the piston chamber. The two o-rings have to be captured since they would get pulled out of the o-ring grooves by the rapidly upwards moving piston. The captured o-ring grooves, which are difficult to machine are the reason for the complex design of the adapter system. A photograph of the three adapter rings can be seen in Fig. 10.2.

A quarter circumference stainless steel ring - element is incorporated in the piston chamber and used as a brake pad to hold the piston in position. The ring-element is actuated by the hydraulic cylinder. A photograph of the partly assembled piston chamber can be seen in Fig. 10.3. In the picture the brake pad ring element can be seen. The brake pad is connected to a shaft, which passes through the wall of the piston chamber. The large spring, which is used to pull back the brake pad is already connected to the shaft system and can be seen on the left of the piston chamber. One of the pistons (the hollow aluminium piston) is shown on the right side of the piston chamber. The complete design of the system can be seen in Fig.10.4.

To operate the diaphragmless driver, high pressure gas ($\sim 10\ bar$) is admitted to the vacuum section first. This forces the piston into the initial position and presses it against the captured o-rings. By applying the appropriate pressure with the manual



Figure 10.3: Arrangement of piston chamber with brake pad and hollow aluminium piston

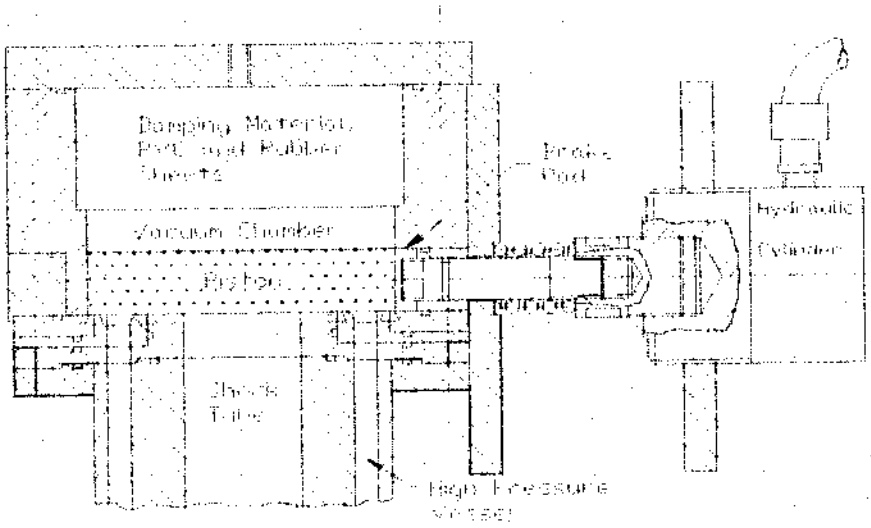

Figure 10.4: Schematic arrangement of the diaphragmless shock tube driver

hydraulic cylinder the ring element presses the piston against the wall of the piston chamber and holds it in place by means of frictional force. A vacuum of about 40 *mbar* can then be introduced to the vacuum section and the driver can be filled with the high-pressure driver gas until the required pressure is reached. To avoid slipping of the piston the frictional force between the piston and the chamber wall has to be higher than the force on the piston caused by the difference between the high pressure in the driver section and the vacuum in the vacuum section.

To initiate a test a manual valve (it was not necessary to use a solenoid valve.) is opened in the hydraulic chamber. This results in an immediate drop of the frictional force. In addition to that the ring element is pulled back by a strong spring. The piston then accelerates rapidly upwards into the vacuum section due to the lifting force of the high pressure and the vacuum (the total stroke of the piston is 21 *mm* plus deformation of the damping pad). After the initial movement of the piston the high pressure acts over the whole area of the piston, which increases the force on the piston. As a result of the movement of the piston the driver gas can now discharge into the low pressure channel and form a shock wave front. The driver is reset by re-pressurising the vacuum section, to push the piston back into the initial position.

10.2.3 EXPERIMENTAL RESULTS

A series of tests were performed to characterise the operation of the new shock tube driver. Three different pistons were used, all having the same diameter and height of 146 *mm* and 30 *mm* respectively. The pistons were made from solid brass (4.4 *kg*), solid PVC (0.71 *kg*) and hollow aluminium (0.38 *kg*). Four pressure transducers were used to record the pressure history. These pressure transducers were located at 22, 32, 43 and 53 pipe diameters downstream of the piston. In all tests the driven section of the tube was at atmospheric pressure (0.83 *bar*). The three pistons were tested with the driver gauge pressure ranging from 2 to 50 *bar*, giving p_4/p_1 values between 3 and 60. The maximum driver pressure was only limited by the maximum capability of the pressure vessel and not by the piston/friction mechanism. Fig.10.5 illustrates the efficiency of the driver. It can be seen that the maximum deviation between the experimental and theoretical (ideal shock tube theory) was 9%. Thus the loss in shock wave strength due to the driver gas flowing around a 180° corner is not large. The maximum errors occurred for the very heavy brass piston because the shock wave was not quite fully established at 53 pipe diameters.

In order to establish the shock formation distance the average Mach number between each pressure transducer station was calculated and the rise time of the shock wave

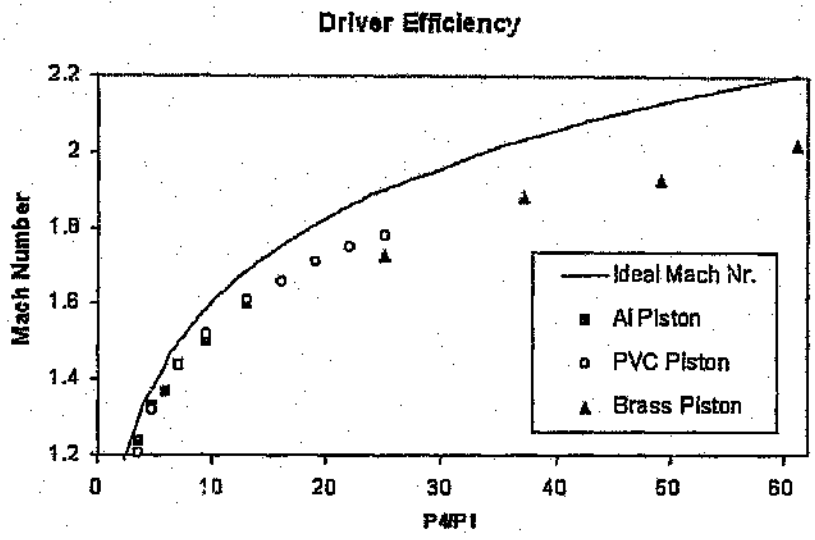

Figure 10.5: Efficiency of the diaphragmless driver

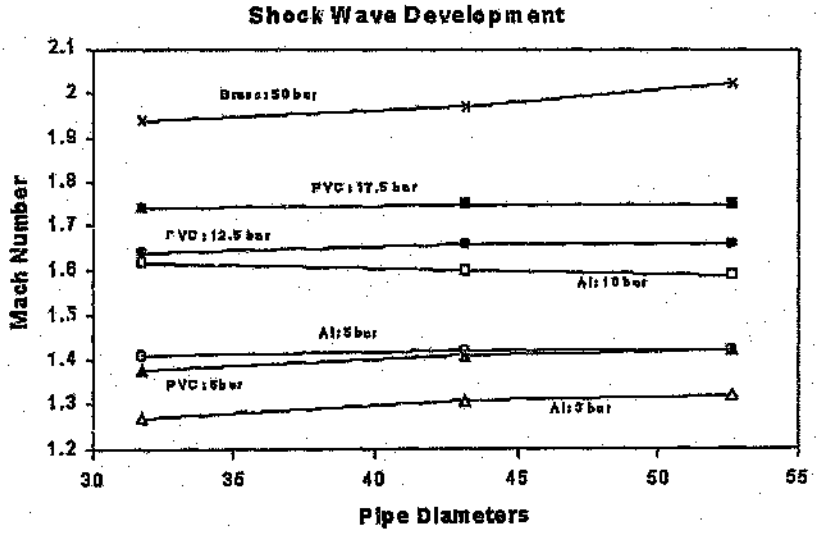

Figure 10.6: Shock wave development

across each pressure transducer was recorded. Figure 10.6 shows the Mach number versus non-dimensional pipe length L/D, for several driver pressures, using all three pistons. For the hollow aluminium piston a Mach 1.33 shock wave was established at between 32 and 43 pipe diameters downstream. A Mach 1.44 wave was established between 22 and 32 pipe diameters. The aluminium piston was not tested at higher pressures, as deformation was observed on the rear face of the piston. This was due to the fact that the skin thickness of the piston was only 5mm. A more elegant design, such as a honeycomb filled core, could easily overcome this problem. The 4.4 *kg* brass piston was tested at driver pressures ranging between 20 and 50 bar. At 20 bar the Mach number at the fourth transducer was 1.73, while the fully established Mach number using the lighter PVC piston at the same driver pressure was 1.78. Using 50 *bar* pressure in the driver the Mach number was 2.02 at the fourth transducer (53 pipe diameters downstream). The ideal Mach number with no losses is 2.2 at this pressure. In addition the rise time of the shock wave across the fourth transducer indicated that the flow was practically established at this point. The PVC piston was tested at driver pressures ranging from 3 to 20 *bar*, but it can also be used at higher pressures. Using the PVC piston the non-dimensional shock establishment length was between 32 and 43 at Mach 1.44 and between 22 and 32 at Mach 1.6. Fig.10.7 shows the pressure history at the four transducer locations for a Mach 1.44 test using the PVC piston. The smooth post shock pressure trace is observed in the last two pressure traces.

The results show that the new friction operated single piston shock tube driver is very effective over a broad range of driver pressures and shock wave strengths. The turn - around time between tests is extremely rapid since no auxiliary diaphragms are used. As with all diaphragmless shock tube designs the experimental reproducibility is greatly improved. The use of a well designed hollow piston is recommended for shock strengths ranging between Mach 1.1 and 1.4, with non-dimensional formation lengths of between 20 and 40. For Mach numbers between 1.4 and 5 the use of a solid piston manufactured from a light material such as PVC also results in shock formation lengths between 20 and 40. The shock tube was tested up to a Mach number of 2, this was due to the fact that the test section was not evacuated and only air was used as the test gas. The brake pad mechanism results in an extremely simple design with rapid piston acceleration. If desirable the use of numerically optimised flow paths to reduce pressure loss around the bends in the vicinity of the driver, as well the implementation of spring gas dynamic damper mechanisms behind the piston (to allow for the use of lighter pistons), as used by [47], could easily be incorporated in the friction operated piston driver concept.

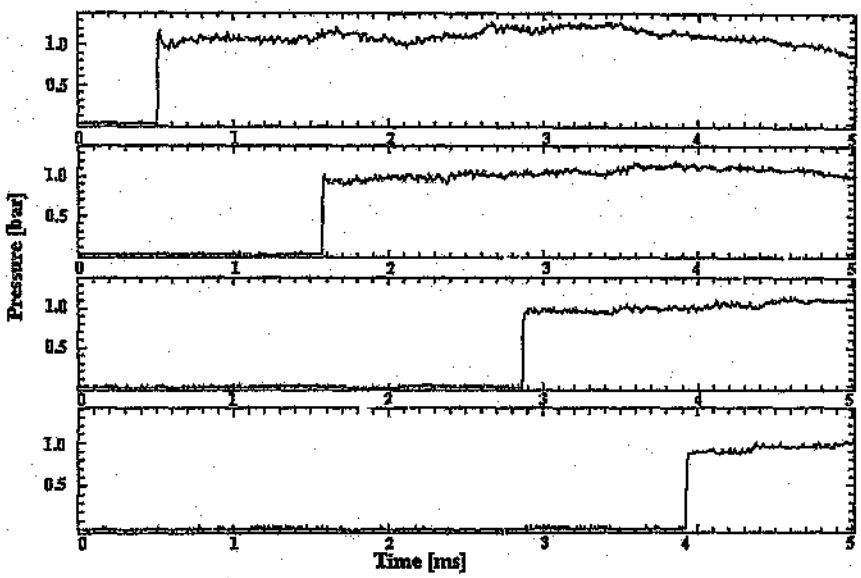

Figure 10.7: Pressure History, Mach 1.44

10.3 PERFORMANCE OF THE DIAPHRAGMLESS SHOCK TUBE IN PROJECTILE MODE

Tests have been performed to test the repeatability and the performance of the modified liquid shock tube. For the tests plastic projectile (0.2 kg) and the steel projectile (3.665 kg) were used. The results are shown in Table 10.1 and 10.2. The table shows the pressure in the driver, the impact velocity of the projectile, the energy, the pressure and the impulse of the liquid shock wave.

The tests have been performed with one set of projectile rings. A change of the projectile rings changes the behaviour of the projectile itself due to the machining tolerance of these rings. The results show that the repeatability of the tests is very high. With the new driver and ambient conditions in the driven section the desired impact velocity of the projectile can be accurately reached. The energy of the liquid shock wave is not as repeatable as the impact velocity since impurities and micro bubbles still absorb parts of the energy.

By using the new diaphragmless driver the shock tube does not have to be opened before each test. On the one hand this is a big advantage since the test turn - around times are now much shorter. On the other hand due to the shock tube

Driver Pressure	Impact Velocity	Shock Wave Energy	Shock Wave Pressure	Shock Wave Impulse
$[bar]$	$[m/s]$	$[J]$	$[MPa]$	$[Ns]$
3	51.6	172.9	37.6	11.34
3	51.7	179.0	39.5	11.13
3.5	57.2	216.0	49.3	12.4
3.5	61.6	181.8	43.05	13.87
4.5	69.7	312.8	52.45	15.01
5.5	79.8	347.1	62.32	15.84
5.5	79.9	449.3	65.0	17.5
6	84.1	468.5	68.2	18.02
6	88.9	482.2	68.5	17.7
15	94.3	501.04	69.0	20.72

Table 10.1: Plastic projectile: Results for tests with diaphragmless liquid shock tube

Driver Pressure	Impact Velocity	Shock Wave Energy	Shock Wave Pressure	Shock Wave Impulse
$[bar]$	$[m/s]$	$[J]$	$[MPa]$	$[Ns]$
15	36.3	1759.4	45.0	91.83
15	36.3	1983.4	47.3	47.3

Table 10.2: Steel projectile: Results for tests with diaphragmless liquid shock tube

staying closed the projectile is not checked for damage to the piston rings before each test. A broken piston ring can block the movement of the piston and therefore spoil the test. This happens on average in one out of ten tests.

11 CONCLUSION

This thesis discusses the high speed metal forming in a liquid shock tube. The high speed metal forming can be carried out by operating the shock tube in two different modes, the air mode and the projectile mode.
The tests performed with the liquid shock tube in the air mode show that this process is not precisely controllable. The process depends strongly on the bursting pressure of the diaphragms and their opening times. The liquid shock wave generated in the air mode has a very long duration and gets superimposed by the remaining static pressure in the shock tube. This static pressure can be high because of the much higher initial pressure required in this mode. This makes it very difficult to determine if the whole deformation of the test specimen is caused by the initial liquid shock wave or if a part of the deformation is due to the static pressure. Also the energy and the impulse of the liquid shock wave are difficult to determine. Another aspect is the total amount of energy, which is needed in the air mode. The driving section requires a much higher pressure to generate a liquid shock wave which is sufficiently strong for metal forming.

The controllability of the shock tube in the projectile mode is much better as shown in section 6. Different projectile masses and materials allow the exact amount of energy required for the metal forming to be produced. The pressure history of the liquid shock wave generated in the projectile mode is similar to that of a blast wave and therefore the energy and the impulse of the liquid shock wave can be precisely determined. The total amount of energy required in the driving section is much lower than for the air mode.
The results of the energy transformation calculations show good accordance with the experimental results. It is possible to predict the impact velocity of the projectile and with that, the kinetic energy available. By using the method of characteristics the liquid shock wave is calculated from the impact velocity of the projectile. This numerical approach makes it possible to predict the maximum pressure, the energy and the impulse of the liquid shock wave. The deformation energy absorbed by the test specimen is calculated by using the flow stress power law.

The effect of different projectile masses, materials and geometries are discussed in section 7. Experimental results are presented, which show how the contour of the liquid shock wave can be tailored to exactly deliver the amount of energy required for the forming of the metal. It is shown that double and triple pressure pulses can be generated by using stepped projectile impact surfaces which gives the possibility to split the deformation process into multiple stage deformations. A finite element program has been employed to model the impact process of the projectile and the generation and propagation of the liquid shock wave. The results of this computation show good quantitative agreement. The contour, the propagation and the reflection at the end wall of the liquid shock waves for different impacting projectiles could successfully be modeled. The maximum pressure and the shock wave energies are higher in the numerical model due to the neglect of micro bubbles and impurities in the water.

The deformations of the copper and mild steel disks have been measured and the true stresses and strains have been determined. The stress strain behaviour of the deformed disks, which is reported in literature to be balanced biaxial, shows good agreement with the theory. Using the strains obtained from the measurements it was possible to calculate the energy absorbed by the deformation of the copper disks. This calculation shows that nearly the total pressure energy of the liquid shock wave is transformed into deformation energy.

A theoretical approach is given to predict the maximum midpoint deflection by assuming a conical shape of the deformed disk. This approach uses an energy method for plastic material behaviour and since the shock wave energy is equal to the deformation energy the strain energy of the disk could be calculated by using the initial shock wave energy imparted to the copper disk. Thinning of the disk during deformation was also taken into consideration and the results of the calculations show a good agreement with experimental values.

Valuable information has been obtained with the optical investigation of test specimens during the impact of the liquid shock wave. Local velocities and the average deformation velocity have been determined. It was also possible to observe the plastic hinge, which has been predicted in the literature.

By using the results obtained from the strain measurements and from the optical investigation it was possible to calculate the strain rates for the deformation processes.

Strain rates at different stages of the deformation process could be obtained by using a mirror system which allows the recording of the side and bottom view simultaneously.

An attempt has been made to model the deformation process of flat disks by employing a finite element package. In the two-dimensional calculation a liquid shock wave generated by the impact of a projectile is used to deform the flat plate. The results of this numerical model show a good qualitative agreement in comparison to experimental results.

The forming of cylindrical mild steel and copper tubes is investigated in section 9. The unsymmetrical deformational behaviour of the tubes for free forming is explained and the stresses and strains are determined. The results of the strain calculations are used to obtain the deformation energy of the tubes.
The optical investigations performed with the high speed video camera reveal the deformational behaviour of the tubes quite clearly. The deformation velocities at different locations of the tube could be obtained and the strain rates calculated. The results show that the strain rates are much lower for the forming of tubes in comparison to the forming of flat disks.
Good results have been obtained with the forming of tubes into cylindrical, hexagonal and octagonal dies. The results show that it was possible to deform the tubes nearly completely into the dies which shows that detailed figuring is possible.

In section 10 the conversion of the tube into a diaphragmless tube is described, which is done by introducing a slotted section and a new diaphragmless driver to the existing tube.
The new diaphragmless driver has been tested extensively by using the shock tube as a normal gas shock tube and by comparing the performance of this new type of driver to already existing diaphragmless drivers. The new driver works very effectively over a broad range of driver pressures and shock wave strength. Non-dimensional shock formation length of between 20 and 40 could be achieved.
For the liquid shock wave work the conversion into a diaphragmless shock tube results in much shorter test turn - around times and in increased repeatability.

This work shows that high speed metal forming in a liquid shock tube is possible. This new forming method has potential for development as a manufacturing process due to its safety and repeatability. It is especially useful for the expansion of tubes, which is difficult to do by using conventional methods and for fine detailed metal forming. In addition the liquid shock tube also serves, due to its good controllability, as a very useful tool in research to further investigate the phenomenon of high speed metal forming.

Since high speed metal forming in a liquid shock tube is a new field of study, this work cannot be regarded as being complete. To further explore this promising

technique several interesting questions which have not been answered yet, should be addressed.

The effect of double and triple shock waves generated by a stepped projectile impact surface on the metal specimen should be investigated since a multiple stage deformation could increase the quality of the forming process. In addition different projectile geometries should be tested to generate various types of liquid shock waves.

Free forming tests with cylindrical tubes should be performed by using a shock tube set-up where the liquid shock wave does not get reflected. This could be achieved by e.g. replacing the solid end wall by a thin diaphragm which tears when the shock wave arrives. This could lead to uniform deformation of the tubes.

The use of the finite element package AutoDyn could be extended e.g. to model the deformation of cylindrical tubes.

The forming of metal specimen into dies has to be further investigated. Interesting to investigate would be the heat development of the metal whilst moving with high speed over the die wall.

REFERENCES

[1] Johnson, W., *A Survey of some High-Rate Forming Methods*, Recent Progress in Metal Working: Lectures Delivered at the Institution of Metallurgists Refresher Course, October 1963, Institution of Metallurgists Great Britain, London Iliffe 1964

[2] Glass, I.L., Sislian, J. P., *Nonstationary Flows and Shock Waves*, Oxford Science Publications, The Oxford Engineering Science Series, Clarendon Press, Oxford, 1994, pp. 20-37, p. 58,

[3] John, J. E. A., *Gas Dynamics*, Second Edition, Allyn and Bacon, Inc., Boston, London, Sydney, Toronto, 1984

[4] Shock Tube Simulation Program *KASIMIR*, Stoßwellenlabor RWTH Aachen, Germany, Copyright @1993

[5] Cole, R. H., *Underwater Explosions*, Dover Publications, Inc., New York, 1965

[6] Müller, M., *Stoßwellenfokusierung in Wasser*, Dissertation, RWTH Aachen, Germany, 1987

[7] Kirkwood, J. G., Bethe, H., Montroll, E., Richardson, J.M. *The Pressure Wave Produced by an Underwater Explosion*, Office of Scientific Research and Development, OSRD Reports I (No. 588), II (No. 676), III (No. 813), 1942

[8] Richardson, J. M., Arons, A.B., Halverson, R.R., *Hydrodynamic Properties of Sea Water at the Front of a Shock Wave*, J. Chem. Phys., 15, 785, 1947

[9] Holl, R., *Wellenfokussierung in Wasser*, Dissertation, RWTH Aachen, 1983

[10] Davies, R., Austin, E. R., *Developments in High Speed Metal Forming*, The Machinery Publishing Co. LTD, Brighton, 1970

[11] Johnson, W., *Impact Strength of Materials*, Edward Arnold, London, 1972

[12] Wilson, F. W., *High-Velocity Forming of Metals*, American Society of Tool and Manufacturing Engineers, Prentice-Hall INC., London, 1964

[13] Jones, N., *Structural Impact*, Cambridge University Press, Cambridge, New York, Port Chester, Melbourne, Sydney, 1989

[14] Rinehart, J. S., Pearson, J., *Explosive Working of Metals*, Pergamon Press, Oxford, London, New York, Paris, 1963

[15] Hudson, G. E., *A Theory of the Dynamic Plastic Deformation of a Thin Diaphragm*, J. Appl. Phys, 22, 1951

[16] Kiyota, M., Fujita, M., *Diverging Plastic Wave Generated at the Centre of a Plate by an Impulsive Load*, Proc. 13th Jap. Natn. Congr. for Appl. Mech., 90 (1963)

[17] Jones, N., *A Literature Review of the dynamic plastic response of structures*, Shock Vib. Dig. 13 (10), 3-16, ,1975

[18] Johnson, W., Kormi, K., Travis, F. W., *An Investigation into the Explosive Deep Drawing of Circular Blanks Using the Plug-Cushion Technique*, Int. J. Mech. Sci., Pergamon Press Ltd., Vol. 6, 1964

[19] Nurick, G. N., *A New Technique to Measure the Deflection-Time History of a Structure subjected to High Strain Rates*, Int. J. Impact Engng. Vol.3, No.1, 1985

[20] Nurick, G. N., *An Empirical Solution for Predicting Maximum Central Deflections of Impulsively Loaded Plates*, Inst. Phys. Conf. Ser. No 102, IOP Publishing Ltd., 1989

[21] Johnson, W., *Experiments and Efficiency Considerations in High Rate Forming*, The Journal of the Australian Institute of Metals, 1966, presented at the Twentieth Annual Conference 1967

[22] Duffey, T. A., *The Large Deflection Dynamic Response of Clamped Circular Plates Subjected to Explosive Loading*, Sandia Laboratories Research Report, SC-RR-67-532, 1967

[23] Nurick, G. N., Martin, J. B., *Deformation of Thin Plates Subjected to Impulsive Loading - A Review*, Int. J. Impact Engng Vol. 8, No. 2, 1989

[24] Travis, F. W., Johnson, W., *Experiments in the Dynamic Deformation of Clamped Circular Sheets of Various Metal Subjects to an Underwater Explosive Charge*, Sheet Metal Industries, 1962

[25] Ida, N. N., Ezra, A. A., *Die-Less, Explosive Forming of One-Piece Thin Shells of Revolution*, Proc. of the 3rd International MTDR Conference, University of Birmingham, 1962

[26] Wedda, H. W., Gallup, R., Cosner, L., N., *The Photography of Explosively Loaded Cylinders*, unpublished paper, for results see [10]

[27] Johnson, W., Doege, E., Travis, F. W., *The Explosive Expansion of Unrestrained Tubes*, Proc. Instn Mech. Engrs, Vol. 179, Pt1, No.7, 1964-65

[28] Pynton, W. A., Travis, F., W., Johnson, W., *The Free Radial Expansion of Thin Cylindrical Brass Tubes Using Explosive Gas Mixtures*, Int. J. Mech. Sci, Pergamon Press, Vol.10, Great Britan, 1968

[29] Chandler, H. D., *On the Increased Strain Rate Sensitivity of the Flow Stress of Copper at High Strain Rates*, Proceeding of The Johannes Weertman Symposium, The Minerals, Metals & Materials Society, 1996

[30] Follansbee, P. S., Kocks, U. F., *A Constitutive Description of the Deformation of Copper Based on the Use of the Mechanical Threshold Stress as an Internal State Variable*, Acta metall. Vol. 36, No. 1, 1988

[31] Lindholm, U. S., in Kawata, K., Shiori, J. (Eds), *High Velocity Deformation of Solids*, Springer Verlag, Berlin, 1978

[32] Bramley, A. N., Mellor, P. B., *The Effect of Strain Rate on the Plastic Flow Characteristics of Steel and Aluminium Sheet*, Journal of Strain Analysis, Vol. 1, No. 5, 1966

[33] Heiser, R., *Die Druckluftkanone - Berechnung und Versuche*, Bericht 14/69, Ernst Mach - Institut, Freiburg, 1969

[34] Larson, V. H., *A Kinetic Hydraulic System for High Energy Rate Metal Forming*, Journal of Engineering for Industry, Transactions of the ASME, 1970

[35] Grönig, H., *Stoßwellen I-III*, Course Notes, RWTH Aachen, 1983

[36] Birnbaum, N. K., *Numerical Simulations of Impact Phenomena in an Interactive Computing Environment*, Century Dynamics Inc., Oakland, California, U.S.A, in AUTODYN, Compendium of Papers, 1991

[37] Johnson, W., Mellor, P. B., *Plasticity for Mechanical Engineers*, D. Van Nostrand Company LTD, London , Toronto, New York, Princeton / New Jersey , 1961

[38] Falthun, L. T., *Finite Element Analysis of Compressible Flows*, Thesis, School of Mechanical Engineering, University of the Witwatersrand, 1995

[39] Mortimer, B. J. P., *Liquid Wave Focusing and the Production of Pulsed Jets*, Thesis, School of Mechanical Engineering, University of the Witwatersrand, 1997

[40] Lohner, R., Morgan, K., Zienkiewicz, O., *An Adaptive Finite Element Procedure for Compressible High Speed Flows*, Comput. Meths. Appl. Mech. Engrg 51, 1985

[41] Lohner, R., Morgan, K., Peraire, J., Vahdati, M., *Finite Element Flux - Corrected Transport (FEM-FCT) for the Euler and Navier - Stokes Equations*, Int. J. Numer. Meths. Fluids 7, 1987

[42] Lohner, R., *An Adaptive Finite Element Scheme for the Transient Problems in CFD*, Comput. Meths. Appl. Mech. Engrg 61, 1987

[43] Garen W., Synofzik R., Frohn A *Shock Tube for Generating Weak Shock Waves*, AIAA J. Vol. 12, No. 8, pp. 1132-1134, 1974

[44] Oguchi H., Funabiki K., Sato S., *An Experiment on Interaction of Shock Wave with Multiple-Orifice Plate by means of a Snap-Action Shock Tube*, Proc. 10th Int. Shock Tube Symposium. Kyoto, 1975, pp. 386-391, 1975

[45] Onodera H., *Double Piston Shock Wave Valve*, AIAA J., Vol. 30, No. 10, pp. 2569-2571, 1992

[46] Yang J., Onodera O., Takayama K., *Characteristics of a Rapidly Opening Shock Tube Using a Rubber Sheet for Weak Shock Wave Generation*, Japanese Machinery Conference Proceedings, (Edition B), doc. no. 93-0773, 1994

[47] Itabashi S., Meguro T., Onodera O., Ojima H., Ogawa T., Takayama K., *Characteristics of a 100 mm X 180 mm Diaphragmless Shock Tube Using a Piston Quick Opening Valve*, Proc. Symposium on Shock Waves, Japan '95. Tokyo, March 14-16 1996, pp. 211-214, 1996

Author: Kosing, Oliver E.

Name of thesis: An investigation of high speed metal forming with liquid shock waves.

PUBLISHER:

University of the Witwatersrand, Johannesburg
©2015

LEGALNOTICES:

Copyright Notice: All materials on the University of the Witwatersrand, Johannesburg Library website are protected by South African copyright law and may not be distributed, transmitted, displayed or otherwise published in any format, without the prior written permission of the copyright owner.

Disclaimer and Terms of Use: Provided that you maintain all copyright and other notices contained therein, you may download material (one machine readable copy and one print copy per page)for your personal and/or educational non-commercial use only.

The University of the Witwatersrand, Johannesburg, is not responsible for any errors or omissions and excludes any and all liability for any errors in or omissions from the information on the Library website.